UNIVERSITÀ DEGLI STUDI DI MILANO

FACOLTÀ DI SCIENZE E TECNOLOGIE

Dipartimento di Fisica
Corso di Laurea Magistrale in Fisica

Realization of spin-dependent optical potentials for quantum transport in ultracold Fermi gases

Relatore interno:
Prof. Davide Emilio Galli

Relatore esterno:
Dott. Giacomo Roati

Correlatore:
Prof. Francesco Scazza

Candidato:
Alessandro Thomas Muzi Falconi

Matricola: 955163

Anno accademico 2020-2021

Contents

Introduction

Understanding the behavior of many interacting particles poses some major challenges both theoretically and experimentally. In particular, due to fermionic statistics, the study of interacting fermions has proven to be one of the greatest challenges of modern physics. As both nucleons inside atomic nuclei and electrons in solid state materials are fermionic particles, the understanding of highly correlated Fermi systems is crucial for the description of many phenomena across all fields of physics. However, the theoretical description of such systems is rather complicated as even the most powerful computers struggle when dealing with simulations of even a few tens of fermions due to the so-called fermion sign problem, the requirement of inverting the sign of a fermionic wavefunction as two particles are swapped.
In this context, much effort has been directed towards the quantum simulation of strongly correlated fermionic systems. Originally proposed by Feynman in 1982 [1], the idea of quantum simulation is based on the realization that some quantum phenomena are too complicated to be simulated with classical computers. Feynman's proposal was then to use a controllable quantum system, whose Hamiltonian could be engineered experimentally, to reproduce another much more complex quantum system of interest. Thanks to their unparalleled degree of controllability, ultracold quantum gases have emerged as a prominent quantum simulator to investigate many-body phenomena that are challenging to approach in solid state as well as in high-energy physics [2]. With advanced technical tools it is possible to manipulate atomic samples with high of precision and control, allowing the on-demand preparation of quantum systems with programmable Hamiltonians. By cooling different atomic species and isotopes it is possible to simulate both bosonic and fermionic systems and laser light allows to trap atoms in many different geometries, including defectless, completely tunable optical lattices to simulate the motion of electrons in periodic potentials. Ultracold atoms have also much longer coherence times than those typical of electrons in solid state, thus making the time and length scales of quantum phenomena much more accessible. Another appealing property of quantum gases is that they are a powerful benchmark for theories. In fact, while in solid state systems most of theoretical assumptions may not be completely valid, it is in principle possible to arbitrarily engineer the Hamiltonians describing ensembles of ultracold atoms. In quantum gases it is therefore possible to artificially introduce theoretical assumptions, eventually providing minimalistic systems where fundamental theories can be tested and verified.
The unique possibility of tuning interatomic interactions offered by Feshbach resonances [3] has allowed to explore both weakly and strongly interacting fermionic systems, providing the breakthrough tool for the description of fermionic superfluidity and of the celebrated BEC-BCS crossover [4–6]. However, the development of new tools for the manipulation of ultracold atomic samples with high resolution and control is paving the way for a new generation of ultracold

atoms experiments. In particular, it is now possible to shape laser light to confine ultracold matter in almost arbitrary geometries and to locally manipulate it with high spatial resolution. These technical advances allow to generate atomic currents with a new level of control and have led to the emergence of the field of *atomtronics* [7]. Most experiments have focused on investigating mass transport in atomic currents, that is the equivalent of charge transport in electronic currents, and only more recently spin transport has been addressed.

In recent years, the investigation of spin transport in fermionic systems has drawn considerable attention due to both fundamental and technological reasons. In fact, electron spin plays a central role in defining the transport properties of many solid state systems. Spin correlations give rise to the wide range of magnetic phenomena and strong magnetic correlations can influence the transport properties of electrons in presence of even a single spin impurity [8]. Even fermionic superfluidity in conventional superconductors is described by Cooper pairs of electrons in opposite spin states [9] and similar singlet pairs are also expected to characterize high T_c cuprate superconductors [10]. As many of the properties of correlated Fermi systems arise from correlations between particles in different spin states, spin transport is also powerful tool to probe such correlations at a fundamental level.

From a technological perspective, the coupled transport of spin and charge currents holds the promise of new spin-based electronic devices. In fact, after decades of constant advance, the development of electronic devices with ever-increasing performances seems to be slowing down as we assist to the breakdown of Moore's law due to excessive miniaturization of electronic components. Extending the manipulation of currents to the spin degree of freedom of electrons may lead to the development of new devices with increased data processing speed and decreased electric power consumption.

This interest towards the coupled transport of spin and charge in solid state systems has led to the emergence of the field of *spintronics*, whose main focus is the manipulation of electronic spins for the ultimate goal of developing spin-based devices [11, 12]. First experimental demonstration of coupled spin and charge manipulation was provided in 1988 by the discovery of giant magnetoresistance [13, 14] and its subsequent application to magnetoresisitve memories showed that the realization of spin-based devices was indeed possible. In the wake of this results, many spintronics devices, such as the paradigmatic Datta-Das *spin field-effect transistor* [15], have been proposed but their real life implementation is forestalled by the complexity of spin manipulation and detection in solid state systems. In fact, these are intrinsically complex environments where the electron spin is not easily accessible and the inevitable presence of external elements, such as phonons, leads to short coherence times and fast spin-relaxation rates.

On the other hand, ultracold Fermi gases allow to investigate spin transport phenomena in a clean and controlled environment where interactions, geometry and dissipative effects can be tuned almost arbitrarily. Further, the spin degree of freedom of ultracold atoms is encoded in their internal states, allowing for much more direct spin manipulation and detection. As transitions between spin states can be driven by radiofrequency pulses, high resolution tailored optical potentials give access to the local manipulation of ultracold gases. This allows to produce both globally and locally spin imbalanced systems and to use opportunely shaped spin-selective or spin-dependent optical potentials to imprint atomic spin currents. The versatile and tunable environment provided by ultracold Fermi gases can therefore be exploited to investigate spin correlations at a fundamental level and to address the many open questions concerning spin transport in highly-correlated Fermi systems.

Within this framework, in this thesis work we develop an experimental setup that allows to realize both spin-dependent tailored optical potentials for investigating quantum transport in a degenerate gas of ^{6}Li atoms. In particular, we demonstrate that by finely tuning the frequency and polarization of a laser beam it is possible to differentially address ultracold lithium atoms in different Zeeman states, which are defined by their spin quantum number. By computing the multi-level polarizabilities of such states we show that we can realize optical potentials that have a differential effect on the atomic spin states, or that affect only one of them, namely spin-selective optical potentials. We therefore develop an experimental setup based on an offset-phase-lock that allows us to set and stabilize the frequency of a laser source to the values necessary for realizing such potentials. After stabilizing the frequency of our laser source, we design and implement on the main experimental apparatus an optical set up for tailoring the intensity profile of our laser beam using a Digital Micromirror Device. With this setup we shine tailored spin-selective perturbations on a degenerate non-interacting Fermi gas composed by a mixture of atoms in two different spin states. We show that we can selectively address each spin state with resonant light, thus introducing local spin-selective losses. Finally, we demonstrate that we can produce both spin-dependent and selective optical potentials by performing an optical Stern-Gerlach experiment. With our experimental setup we can therefore investigate the dynamical response of a fermionic system in presence of spin-dependent external perturbations and explore the role of spin correlations in different geometries and interaction regimes. Our findings will help shed light on fermionic spin correlations and on the fundamental mechanisms underlying the spin transport properties of correlated Fermi systems.
This thesis is organized as follows:

- In Chapter 1 we give an overview of the tools enabling the production and manipulation of a ^{6}Li degenerate gas in our laboratory. We describe the fundamental properties ot atoms-light interaction, with particular focus on the scattering and dipole optical forces which are the two crucial tools for cooling and manipulating an atomic sample. We then discuss the specific properties of ^{6}Li atoms that are necessary to understand the techniques we employ for manipulating them. In the third part of the chapter we give a brief overview of the basic properties of trapped degenerate Fermi gases at zero temperature and of how we can tune interactions between atoms using Feshbach resonances. In the fourth part of this chapter we describe the main experimental apparatus and the techniques we use for cooling and manipulating our fermionic sample as well as for extracting information from it. In the last part of the chapter we focus on the experimental protocol that we employ for producing a degenerate non-interacting Fermi gas and on how we measure its temperature.

- In Chapter 2 we provide a framework regarding the investigation and the relevance of spin transport in different contexts. In the first part of the chapter we give a brief overview of the fundamental aspects of spin transport in solid-state materials, with particular focus on applications in spintronics and spin caloritronics. In the second part of this chapter we report on the experimental investigation of spin transport in ultracold Fermi gases, focusing on the case of ^{6}Li. Finally we introduce the idea of generating spin currents with spin-dependent optical potentials and we highlight the novelty and the advantages that this technique may offer compared to others.

- In Chapter 3 we report on the the realization of spin-selective and spin-dependent tailored

optical potentials. We start by describing how such potentials arise from the properties of light interacting with multi-level atoms, how we compute the multi-level atomic polarizability and how this polarizability allows to realize both spin-dependent and spin-selective optical potentials. In the second part of the chapter we describe the offset-lock setup we developed for locking the frequency of our laser source to the values necessary for realizing such potentials. We then show how we can manipulate the intensity profile of a laser beam with a Digital Micromirror Device and how this allows us to tailor the spatial profile of an optical potential. Finally we describe the optical setup we designed and built for shaping our laser beam and for shining spin-selective tailored optical potentials on the atomic sample taking advantage of a pre-existent horizontal imaging setup.

- In Chapter 4 we report on the experiments we performed for testing the spin-dependent and spin-selective perturbations on a non-interacting Fermi gas. In the first part of this chapter we focus on dissipative perturbations and we show that we can selectively address spin states with resonant light in order to introduce local spin-selective losses or heating in our sample. In the second part of this chapter we describe how we produce arbitrarily shaped optical potentials by manipulating the intensity profile of a laser beam using a Digital Micromirror Device. We then report on an optical Stern-Gerlach experiment that allows us to demonstrate the capability of realizing both spin-selective and spin-dependent optical potentials. Finally we offer a brief outlook on the possibility of using our setup for imprinting spin currents in the atomic sample to investigate spin transport in our system.

Chapter 1

Production and manipulation of a ^{6}Li degenerate Fermi gas

The atomic physics' toolbox allows to manipulate atomic ensembles with an outstanding level of control and can be used to produce ultracold degenerate atomic gases. In this chapter we will describe how we are able to produce a sample composed by ultracold ^{6}Li atoms in different interaction regimes. The first part of this chapter will be dedicated to the description of the atom-light interaction. In the second part we will briefly describe the electronic structure of ^{6}Li and then introduce the main properties of ultracold Fermi gases, with particular focus on fermionic lithium. In the fourth part we will give an overview of our experimental setup and routine for trapping and cooling an atomic gas to degeneracy. In the last part of this chapter we will describe the experimental procedure for obtaining a non-interacting ^{6}Li Fermi gas.

1.1 Atom-light interaction

The investigation of atoms-light interaction has been the spark that ignited the quantum revolution in the early years of the 20th century. Since then, the exploration of the response of atomic mediums to electromagnetic radiation has been one of the most active areas of research in physics. In the last decades, the use of laser light for atomic manipulation has been the breakthrough tool to achieve trapping and cooling of atomic samples. Absorption and emission of resonant light provided the first tool to slow atomic beams and nowadays the interaction between atoms and resonant light still plays a fundamental role in all ultracold atoms experiments. However, this interaction can be considered a dissipative process and the cooling techniques based only on resonant light present some crucial limits. When a moving atom absorbs a counterpropagating photon it loses kinetic energy due to momentum conservation, however when the atom re-emits the photon it does so in a random mode and recoils in a random direction. For this reason, the use of resonant light is not sufficient to cool atoms below a certain threshold and to coherently manipulate them.
Since the first demonstration of the *otpical tweezers* technique by Nobel prize laureate Arthur Ashkin, great effort has been directed towards the manipulation of atomic samples with non-resonant light. As interactions between atoms and non-resonant light do not rely on absorption of photons, non-resonant light allows to induce non-dissipative forces on atomic samples. As

optical forces provide an unrivalled tool for the manipulation of biological matter, such as cells of bacteria, non-resonant light offers a mean to cool atoms to degeneracy and coherently manipulate them.
Adopting a semiclassical approach, we can treat an atom as a quantum object with quantized internal states $|i\rangle$ and consider a classical monochromatic electromagnetic field:

$$\mathbf{E}(\mathbf{r},t) = E_0(\mathbf{r})e^{i(\phi(\mathbf{r})-\omega t)}\hat{\epsilon} + c.c. \tag{1.1}$$

The Hamiltonian of the atom in the external field is:

$$H = H_A + H_I \tag{1.2}$$

where H_A is the unperturbed atomic Hamiltonian, whose eigenvectors are just the atomic energy levels, and H_I is the atom-light interaction Hamiltonian. Considering a two-level atom in the *dipole approximation*, the interaction Hamiltionian is [16, 17]:

$$H_I = -\mathbf{d}\cdot\mathbf{E}(\mathbf{r}) \tag{1.3}$$

where $\mathbf{r}$ is the atom's center of mass position and $\mathbf{d}$ is the atomic dipole operator, which is related to the field amplitude via the complex polarizability α ($d(\omega) = \alpha(\omega)E(\omega)$).
In the Heisenberg picture, the force acting on the atom is:

$$\mathbf{F} = \frac{d\mathbf{p}}{dt} = \frac{i}{\hbar}[H,\mathbf{p}] = -\nabla H_I. \tag{1.4}$$

Since we can consider the induced dipole moment to be independent on the atomic position, we can safely take it out of the derivative and write $\mathbf{F} \propto \nabla E(\mathbf{r})$. The electric field depends on position both in its amplitude and in its phase, therefore computing the derivative of the electric field results in two terms, related to the gradient of the phase and of the amplitude respectively. The total force acting on the atom is therefore the sum of two terms:

$$\mathbf{F} = \mathbf{F}_{scatt} + \mathbf{F}_{dip} \tag{1.5}$$

where $\mathbf{F}_{scatt} \propto \nabla\phi(\mathbf{r})$ is the *scattering force*, which arises from the absorption and re-emission of photons, and $\mathbf{F}_{dip} \propto \nabla E(\mathbf{r})$ is the *dipole force*, which is a non-dissipative force related to dispersion.

1.1.1 Photon absorption and re-emission

Every time an atom interacts with light momentum must be conserved. Therefore, when an atom absorbs or emits a photon it recoils so that its momentum change compensates that of the emitted or absorbed photon. This light-induced change of momentum can indeed be considered a force that light exerts on the atom.
This scattering force therefore is:

$$\mathbf{F}_{scatt} = \hbar\mathbf{k}\,\Gamma_{sc} \tag{1.6}$$

where $\mathbf{k}$ is the absorbed photon momentum and Γ_{sc} is the *scattering rate*, which describes the rate at which photons are absorbed and spontaneously re-emitted. Neglecting any stimulated emission process, we can write $\Gamma_{sc} = \Gamma\,\rho_{22}$ where Γ is the linewidth of the considered atomic

transition and ρ_{22} is the probability of finding the atom in the excited state. Considering light with a frequency detuning $\delta = \omega - \omega_0$ from the atomic transition, the steady-state solution of the optical Bloch equations yields [16, 17]:

$$\Gamma_{sc}(\mathbf{r}) = \frac{\Omega^2(\mathbf{r})/\Gamma}{1 + 2\Omega(\mathbf{r})^2/\Gamma^2 + 4\delta^2/\Gamma^2} \tag{1.7}$$

where Γ is the transition linewidth and Ω is the *Rabi frequency* that describes the coupling between the atomic transition and the field:

$$\Omega(\mathbf{r}) = \frac{\langle g|\hat{\epsilon}\cdot\mathbf{d}|e\rangle\, E_0(\mathbf{r})}{\hbar}. \tag{1.8}$$

It is worth noting that the scattering rate has an inverse quadratic dependence on the detuning, resulting in a fast decrease of the probability of photon absorption as the detuning increases. Introducing the *saturation intensity* I_s defined as $I/I_s = 2\frac{\Omega^2}{\Gamma^2}$ we can write Eq. 1.7 as a function of the light intensity $I(\mathbf{r}) = 2\epsilon_0 c\,|E_0(\mathbf{r})|^2$:

$$\Gamma_{sc}(\mathbf{r}) = \frac{\Gamma}{2}\,\frac{I(\mathbf{r})/I_s}{1 + I(\mathbf{r})/I_s + 4\delta^2/\Gamma^2}. \tag{1.9}$$

This expression explicitly shows that the photon absorption probability is linear in the light intensity as long as such intensity remains much smaller the the saturation intensity. The scattering force that light can exert on an atom is bounded from above by the maximum value $\mathbf{F}_{scatt,max} = \hbar\mathbf{k}\frac{\Gamma}{2}$ which is obtained for $I \gg I_s$.
From Eq. 1.6 we see that if an atom moves towards a counterpropagating laser beam, the average effect of the scattered photons is to induce a force along the propagation direction of the beam, i.e. opposite to the velocity of the moving atom, which is thus slowed down. This effective viscous force has been extensively exploited for slowing, cooling and trapping atomic ensembles with Zeeman slowers, optical molasses and magneto optical traps (MOTs) [17, 18].
However, this techniques based solely on the scattering force are often non sufficient to cool atomic samples down to the degenerate regime. This is because each time an atom emits a photon it recoils in a random direction with recoil energy $\frac{(\hbar k)^2}{2m} = k_B T_{rec}$, which for the D_2 line (see next section) of ^{6}Li is around 3.5 μK [19]. Further, the lowest temperature achievable exploiting only absorption and re-emission processes, namely the *Doppler temperature*, is $k_B T_D = \frac{\hbar\Gamma}{2}$, which is higher than the recoil temperature due to fluctuations in the number of absorbed and re-emitted photons. This fluctuations lead to a reduction in cooling efficiency [17], thus preventing the cooling of atomic samples below the Doppler temperature, which is orders of magnitudes higher ($T_D = 140\,\mu$K for ^{6}Li [20]) than the degeneracy temperature.
As the scattering force relies on incoherent spontaneous emission, it is a non-conservative force. This makes techniques based on the scattering force valuable tools for the first steps of the cooling procedure, but rarely suitable for further cooling and for the coherent manipulation of ultracold samples.

1.1.2 Optical potentials

To cool atomic gases to degeneracy and manipulate them in a non-dissipative and coherent way, it is customary to use non-resonant light. For far detuned light, photon absorption is highly

unlikely and the dipole force can be exploited to exert a conservative optical force on atomic samples. While the scattering force is related to the in quadrature phase component of the induced dipole moment [17], or, equivalently, to the imaginary part of the polarizability α [21], the dipole force is related to the in phase component of the dipole moment and to the real part of the polarizability. Computing these quantities leads to a dipole force that is proportional to the gradient of the squared Rabi frequency:

$$\mathbf{F}_{dip}(\mathbf{r}) = -\frac{\hbar\delta}{1 + 2\Omega^2(\mathbf{r})/\Gamma^2 + 4\delta^2/\Gamma^2}\nabla\Omega^2(\mathbf{r}). \tag{1.10}$$

It is possible to rearrange this expression to highlight that the dipole force is a conservative force arising from a potential [16]:

$$\begin{aligned} \mathbf{F}_{dip}(\mathbf{r}) &= -\nabla V_{dip}(\mathbf{r}) \\ V_{dip}(\mathbf{r}) &= \frac{\hbar\delta}{2}\log\left[1 + \frac{|\Omega(\mathbf{r})|^2}{2\left((\Gamma/2)^2 + \delta^2\right)}\right]. \end{aligned} \tag{1.11}$$

The potential V_{dip} is the *optical potential* and it is the main element enabling laser light manipulation of atoms. If light is sufficiently far-detuned, so that $|\delta| \gg \Gamma, \Omega$, we can simplify the expression of the dipole potential as:

$$V_{dip}(\mathbf{r}) \simeq \frac{\hbar|\Omega(\mathbf{r})|^2}{4\delta}. \tag{1.12}$$

This expression can, again, be expressed as a function of the intensity saturation parameter $s = I/I_s$ as:

$$V_{dip}(\mathbf{r}) \simeq \frac{3\hbar\Gamma^2}{8\delta}\frac{I(\mathbf{r})}{I_s} \tag{1.13}$$

where the factor 3 account for the possible states of light polarization.
When atoms are exposed to non-resonant light they feel an optical potential proportional to the intensity of the light and inversely proportional to the detuning from the considered atomic transition. Therefore, by using either red ($\omega < \omega_0$) or blue ($\omega > \omega_0$) detuned light, it is possible to engineer attractive or repulsive potentials respectively. Notably, the optical potential has a linear dependence on the inverse detuning $1/\delta$, while that of the scattering rate is quadratic. Therefore, for large detunings, the scattering probability falls much faster than the amplitude of the optical potential. Also, while the absorption probability saturates for high intensities, the dipole potential can be arbitrarily large as intensity increases, even though only logarithmically for the higher intensities. Because of these dependencies on $1/\delta$ and I, it is preferable to manipulate atoms using high intensity far-detuned laser light, so that the dipole potential is large while the unwanted effects related to photon absorption are largely suppressed.
The many available tools for controlling the spatial intensity profile of laser light allow to use both attractive and repulsive optical potential for the arbitrary manipulation of atomic samples. In particular, it is possible to use attractive red-detuned Gaussian beams as optical dipole traps (ODTs) [21] so that atoms remain trapped in the high-intensity regions, in the same way as biological matter is manipulated with optical tweezers. Further, it is possible to use repulsive, blue-detuned, light to confine the atoms in arbitrary geometries and to introduce obstacles inside an atomic sample [22–24].

We stress that expression 1.13, despite capturing the general behavior of atoms exposed to non-resonant light, should be used with caution, since it relies on three assumptions which may not be valid. The first one is the *rotating wave approximation*, i.e. we assume that $\omega - \omega_0 \ll \omega + \omega_0$ so that we can neglect terms proportional to $\frac{1}{\omega+\omega_0}$. In the range of optical atomic transitions this is generally true. The second assumption is that the detuning from the atomic transition is much larger than the transition linewidth. Again, this is usually the case when we want to use optical potentials for manipulating atoms with non-resonant light, since having a detuning comparable with the frequency linewidth results in high photon-absorption probability. The last assumption is considering the atom a two-level system, which, in general, is not true. Atoms in one particular state always have many accessible higher-energy excited states and the decision about which transitions can be neglected is quite an important one. Usually, there is one main transition which has the smallest detuning from the light frequency and it is the one that we would consider in a two-level approximation. We can then neglect the contribution of transitions for which the detuning is much bigger than that of this main transition or that have an energy difference so small that they are not resolved, therefore contributing with one transition only (with the appropriate degeneracy).
An alternative way of describing optical potentials is that of the *light shifts* or *dressed states* picture [21]. This approach is equivalent to our previous treatment but it is particularly appealing for the description of state-dependent optical potentials. In this picture, the interaction between the light's electromagnetic field and the internal atomic levels leads to an energy shift of the involved levels, which become *dressed* by the interaction. For the transition's ground state, these light shifts or *AC Stark shifts* are negative(positive) for red(blue)-detuned light, thus resulting in an effective attraction(repulsion) towards(from) the region of high light intensity. If we consider an ensemble of atoms in different ground states (e.g. in different hyperfine levels of an energy manifold) each state will feel a different light shift and, therefore, a different optical potential. The light shifts picture can also be used to intuitively describe the atom-light interaction beyond the two-level approximation. In Chapter 3 will see how multi-level light shifts give rise to state-selective optical potentials.

1.2 ^{6}Li fundamentals

All the fundamental tools for the production and manipulation of ultracold ^{6}Li gases rely on the properties of its level structure, which we will briefly describe in this section.
Lithium-6 is the fermionic isotope of lithium which is an alkali atom with two core electrons and a single unpaired valence electron. Therefore, its ground state electronic configuration is $1s^2 2s^1$ while the first excited state is $1s^2 2p^1$, which is connected to the ground state by an optical transition called D-line. This transition has a wavelength of almost 671 nm, corresponding to visible red light.
However, as for all alkalis, the D-line of ^{6}Li is split in two narrower lines, namely the D_1 and D_2 lines by the *spin-orbit coupling*. This coupling arises from the mutual interaction between the orbital and spin electronic magnetic moments and results in the *fine structure* of the atomic energy levels. Inserting the spin-orbit interaction as a perturbation in the atomic Hamiltonian allows to compute the energy of the D_1 and D_2 transitions. To do so, it is usual to work in the total electronic angular momentum $\hat{\mathbf{J}} = \hat{\mathbf{L}} + \hat{\mathbf{S}}$ basis. In this basis, each state is finely splitted into levels with different J for $|L - S| \leq J \leq L + S$. The ^{6}Li ground state has $S = 1/2$ and

$L = 0$, therefore the only allowed value for the total angular momentum is $J = 1/2$ and the ground state is not split by the spin-orbit coupling.
The excited state, instead, has $L = 1$, and is thus split in two levels with $J = 1/2$ and $J = 3/2$ respectively. The transition to the lowest energy state ($J = 1/2$) results in the D_1 line (670.992 nm), the transition to the highest energy state ($J = 3/2$) in the D_2 line (670.977 nm). Computing the energy difference between the two lines we get the size of the fine structure splitting $\Delta E_{FS} \simeq 10$ GHz [19].

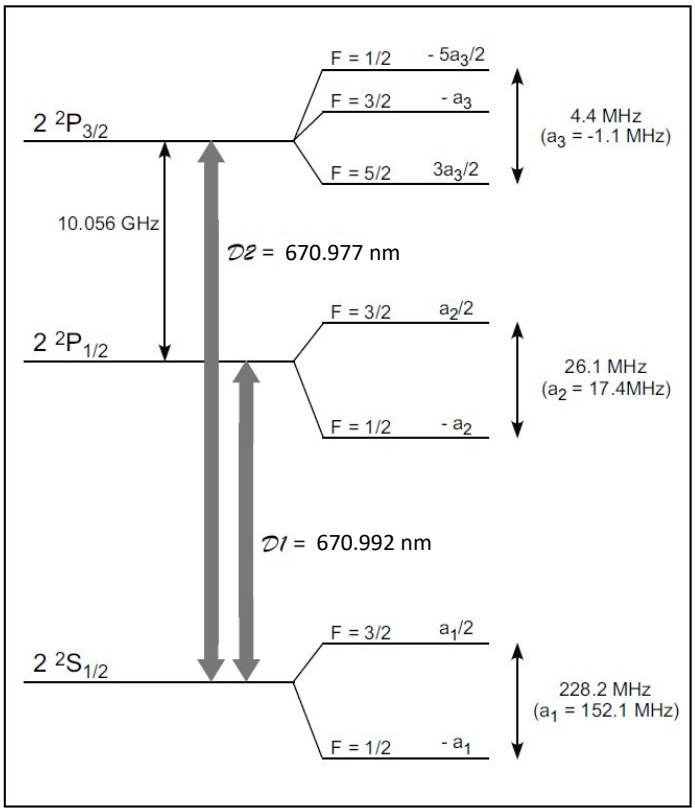

Figure 1.1: Structure of the ground and ^{2}P excited states of ^{6}Li. The spin-orbit coupling splits the excited state in two states, which are connected to the ground state by the D_1 and D_2 lines respectively. The interaction with the nuclear magnetic moment results in a further splitting of the fine sublevels. Energy splittings are not to scale. Image taken from Ref. [19].

For the cooling of alkali atoms it is also necessary to consider the further splitting of the fine levels due to the coupling between the electronic magnetic moment and the nuclear spin magnetic moment $\hat{\mathbf{I}}$, which is 1 for fermionic lithium. This *hyperfine structure* is crucial for the manipulation of lithium atoms in presence of magnetic fields and for the generation of spin-dependent optical potentials. As for the spin-orbit coupling, when computing the eigenvalues of the hyperfine Hamiltonian it is useful to define a new operator and a new quantum number related to it. We therefore define the total angular momentum of the atom $\hat{\mathbf{F}} = \hat{\mathbf{I}} + \hat{\mathbf{J}}$, which can take values in the range $|J - I| \leq F \leq J + I$. The introduction of the hyperfine interaction results in a separation of the ground state in two sublevels separated by an energy difference

of 228.2 MHz [19]. The two excited states corresponding to the D_1 and D_2 lines split into two and four sublevels respectively with even smaller energy separations. We report the zero field structure of ^{6}Li in Fig. 1.1.

1.2.1 ^{6}Li in magnetic fields

So far we have considered the structure of ^{6}Li in absence of external perturbations. However, the cooling, trapping and manipulation of ultracold atoms heavily rely on magnetic fields. Therefore, the energy levels that we need to consider in our experiments are not the unperturbed hyperfine states but are states that are heavily affected by the presence of external magnetic fields. In particular, we have to consider the *Zeeman effect* arising from the interaction between the atomic magnetic moment and a static magnetic field.
Since this interaction energy is proportional to the amplitude of the external field B, for sufficiently low fields, the Zeeman effect can be treated as a perturbation to the hyperfine structure of the atomic levels. As long as B remains small, F is still a good quantum number and the perturbation can be easily computed as $\Delta E_Z = \frac{\mu_B}{\hbar} g_F m_F B$, where $\mu_B \simeq 1.4$ MHz/G is Bohr's magneton, g_F is the Landè g factor and m_F is the projection of $\hat{\mathbf{F}}$ along the quantization axis, which is usually defined by the direction of the magnetic field. As B increases, the interaction

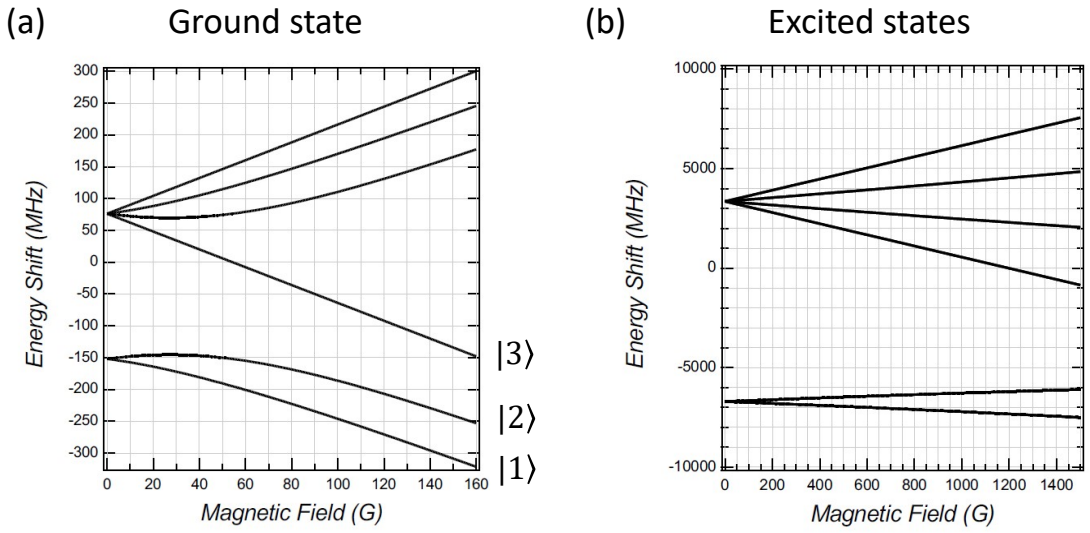

Figure 1.2: Zeeman sublevels of ^{6}Li. (a) Zeeman shift of the hyperfine ground state manifold. From the experimental point of view we are interested in the three lowest sublevels, which we label $|1\rangle$, $|2\rangle$ and $|3\rangle$. (b) Zeeman shift of the $^2P_{1/2}$ and $^2P_{3/2}$ manifolds. Due to its small size, the hyperfine splitting of the excited states can be neglected for all experimentally-relevant magnetic fields. Image adapted from Ref. [19].

energy becomes significant compared to the hyperfine splitting. When this happens F ceases to be a good quantum number and we must look for eigenstates of the full Hamiltonian of the system. For ^{6}Li both the ground and excited states have very small hyperfine splittings, therefore the perturbation regime fails at very low values of B. In the strong-field regime, called *Paschen-Back regime*, we can diagonalize the full Hamiltonian in the $|J, m_J; I, m_I\rangle$ basis and

treat the hyperfine interaction as a small perturbation to the atom-field Hamiltonian. For intermediate fields the energy shifts are more difficult to compute and the full Hamiltonian must be diagonalized numerically.
We report the magnetic field dependence of the ^{6}Li Zeeman subleveles in Fig. 1.2. The two hyperfine levels of the ground state manifold split in two and four Zeeman sublevels respectively. However, as the magnetic field increases, the lowest energy state of the $F = 3/2$ hyperfine level bends towards the $F = 1/2$ states, resulting in the formation of two triplets of Zeeman states. From the experimental point of view we are interested in the three lowest sublevels which we label $|1\rangle$, $|2\rangle$ and $|3\rangle$. These state differ mainly by their nuclear spin projection along the quantization axis m_I and are the states that are populated by the atoms in all our ultracold samples. Since the ^{6}Li excited states have a very small hyperfine splitting, for such states the Paschen-Back regime is reached at magnetic fields lower than those experimentally significant. Therefore, we can neglect the hyperfine structure of the exicted states manifold and write $\Delta E_Z \simeq \frac{\mu_B}{\hbar} g_J m_J B$. This leads to a splitting of the $^2P_{1/2}$ and $^2P_{3/2}$ fine levels into two and four Zeeman states respectively.

1.3 Degenerate Fermi gases

Even though a single particle displays many interesting properties, some of the most fascinating quantum effects arise when many quantum objects become correlated and the behavior of the whole system is governed by the underlying quantum nature of its constituents. These correlations lead to the emergence of quantum collective phenomena, which often result in spectacular effects such as Bose-Einstein Condensation or superconductivity. However, it is usually not trivial to observe these quantum collective phenomena, since they are often suppressed by other effects, such as interactions with external sources or thermal motion. One way of searching for how and when do these quantum collective phenomena occur is considering the de Broglie wavelength of particles:

$$\lambda_{dB} = \sqrt{\frac{2\pi\hbar^2}{mk_BT}}. \tag{1.14}$$

This quantity represents the extent of the wavepacket associated to a particle. When this wavelength becomes comparable to the distance between two particles, their wavefunctions begin to overlap and the quantum nature of their interaction is unveiled. Identical particles with a de Broglie wavelength comparable to their inter-particle spacing become intrinsically indistinguishable and a system composed by such indistinguishable particles is said to be *degenerate*. Such degeneracy is the condition for the emergence of quantum collective behaviors.

1.3.1 Quantum statistics

In quantum mechanics, identical particles are intrinsically indistinguishable and are described by collective wavefunctions. Depending on the nature of the particles, these collective wavefunctions must have different parity with regard to particle exchange. The wavefunction of an ensemble of identical bosons must be symmetric under particle exchange, while that of fermions must be antisymmetric.
The main consequence of the different parity between between fermionic and bosonic ensembles

is their different tendency towards occupying the same quantum state with more than one particle. While two or more identical bosons can freely populate the same quantum state, the antisymmetric nature of fermions prevents them from doing so. This is the well-known *Pauli exclusion principle*, which states that two identical fermions can never occupy the same quantum state. Since bosons can populate the same quantum state, while fermions cannot, systems of non-interacting bosons or fermions have very different ground state properties. All the particles composing an ensemble of non-interacting bosons in the ground state occupy the single particle lowest energy level. In contrast, the ground state of a fermionic system is composed by particles filling all available energy levels up to the *Fermi energy*, so that there are never two particles in the same state.
By computing the partition function of non-interacting, identical quantum particles it is possible to obtain the distribution function of both bosons and fermions, corresponding to the mean occupation number of a state with energy ε:

$$f_\epsilon = \frac{1}{e^{\beta(\varepsilon-\mu)} \pm 1} \tag{1.15}$$

where $\beta = 1/k_B T$ and μ is the chemical potential. In this expression, the $-$ sign is referred to bosons (*Bose-Einstein distribution*) and the $+$ to fermions (*Fermi-Dirac distribution*). This different sign leads to the striking differences between the properties of fermionic or bosonic ensembles.
Atoms are not elementary particles, as they are composed by a number of fermions (electrons, protons and neutrons) which depends on the atomic species and on the considered isotope. Therefore, the number of fermions composing an atom defines its quantum nature. If this number is even, the atom has integer spin and is a boson, conversely atoms composed by an odd number of fermions are fermions themselves. ^{6}Li atoms are composed by six nucleons and an unpaired electron, thus being fermions.
When the temperature is sufficiently high ($\beta \gg \mu$), both the Fermi-Dirac and Bose-Einstein distributions reduce to the classical Boltzmann exponential distribution and the quantum properties of the atomic ensemble are hidden by the particles' thermal motion. Since for atomic samples μ/k_B is usually below 1 μK, to produce a degenerate atomic ensemble it is necessary to drastically lower the temperature of the system. However, lowering the temperature while keeping the density fixed results in a transition to the solid state, in which atoms are fixed inside a lattice. Fixing the atoms' positions effectively makes them distinguishable, thus suppressing quantum degeneracy. It is therefore necessary to prevent any classical phase transition in the process of cooling an atomic sample. To do so, it is possible to produce a system in a metastable gaseous dilute regime with very low number density ($n < 10^{13}\, cm^{-3}$). Such low density results in a strong suppression of three body collisions, which are necessary for the formation of the atomic bonds that lead to classical phase transitions, and provides the way for producing degenerate atomic gases.
The way to achieve a degenerate quantum gas is therefore to produce an ultracold and dilute atomic sample. As an example, we can consider a ^{6}Li gas ($m = 9.98\,10^{-27}$ kg) with $n \simeq 10^{13}\, cm^{-3}$. For such a sample, the degeneracy condition $\lambda_{dB} \simeq n^{-1/3}$ is reached for $T < 1\,\mu K$.

1.3.2 Zero temperature Fermi gases in harmonic traps

As we will see in the following sections, ultracold atoms experiments are often performed in optical dipole traps. These traps are usually obtained by crossing two red-detuned laser beams with Gaussian profiles. Using red-detuned beams generates an attractive optical potential towards the high-intensity region, so that atoms are trapped in the region where the beams cross. This trapping potential is necessary for confining the atoms and can be well approximated by an harmonic trap.
For harmonically trapped atoms, the energy ε of Eq. 1.15 can be written as the sum of the kinetic and the harmonic potential energy, so that the Fermi-Dirac becomes:

$$\begin{aligned} f(\mathbf{r},\mathbf{p}) &= \frac{1}{e^{(\frac{p^2}{2m}+V(\mathbf{r})-\mu)/k_BT}+1} \\ V(\mathbf{r}) &= \frac{1}{2}m(\omega_x^2x^2+\omega_y^2y^2+\omega_z^2z^2) \end{aligned} \tag{1.16}$$

where $\omega_{x,y,z}$ are the trap frequencies along the three spatial directions.
For $T\to 0$, this distribution is 1(0) if the total energy is below(above) the chemical potential:

$$f(\mathbf{r},\mathbf{p}) \xrightarrow[T\to 0]{} \begin{cases} 1 & \frac{p^2}{2m}+V(\mathbf{r})<\mu \\ 0 & \frac{p^2}{2m}+V(\mathbf{r})>\mu. \end{cases} \tag{1.17}$$

This means that, in a zero-temperature non-interacting Fermi gas, particles fill all the energy levels up to the chemical potential, while leaving empty the states with higher energy. Therefore, at zero temperature, μ is the energy of the highest occupied state, i. e. the Fermi energy E_F, and sets the most important energy scale of the system. The spatial density profile of a zero-temperature non-interacting Fermi gas is given by [4]:

$$\begin{aligned} n_F(\mathbf{r}) = \int \frac{d^3\mathbf{p}}{(2\pi\hbar)^3} f(\mathbf{r},\mathbf{p}) &\xrightarrow[T\to 0]{} \int_{|\mathbf{p}<\sqrt{2m(\mu-V(\mathbf{r}))|}} \frac{d^3\mathbf{p}}{(2\pi\hbar)^3} = \\ &= \frac{1}{6\pi^2}\left(\frac{2m}{\hbar^2}\right)^{3/2}(\mu-V(\mathbf{r}))^{3/2}. \end{aligned} \tag{1.18}$$

The Fermi energy can be found by fixing the total number of particles $N=\int d^3\mathbf{r}\; n_F(\mathbf{r})$. Integrating the previous expression for the particle density yields:

$$E_F = \hbar\bar{\omega}(6N)^{1/3} \tag{1.19}$$

where $\bar{\omega}=(\omega_x\omega_y\omega_z)^{1/3}$ is the geometric mean of the trapping frequencies.
This is the global Fermi energy of the system and the globally largest momentum is the Fermi momentum $p_F=\hbar k_F=\sqrt{2mE_F}$. However, an harmonically trapped system is not homogeneous and we should introduce a local Fermi energy and momentum $p_F(\mathbf{r})=\hbar k_F(\mathbf{r})=\sqrt{2m\epsilon_F(\mathbf{r})}=\hbar(6\pi^2 n_F(\mathbf{r}))^{1/3}$. The global Fermi energy equals the local Fermi energy in the trap center, therefore:

$$E_F = \frac{\hbar^2k_F^2}{2m} = \frac{\hbar^2}{2m}(6\pi^2 n_F(0))^{2/3}. \tag{1.20}$$

The spatial profile of the atomic density in Eq. 1.18 can be explicitly written as:

$$n_F(\mathbf{r}) = \frac{8}{\pi^2}\frac{N}{R_{Fx}R_{Fy}R_{Fz}}\left[\max\left(1-\sum_i \frac{x_i^2}{R_{Fi}^2}, 0\right)\right]^{3/2} \tag{1.21}$$

where $R_{Fx,y,z} = \sqrt{\frac{2E_F}{m\omega_{x,y,z}^2}}$ are the *Thomas-Fermi radii* that define the size of the system at zero temperature since the density profile vanishes for $r > R_F$. While the size of a Bose gas does not depend on the number of bosons in the system, for a Fermi gas this quantity is proportional to the total number of particles, due the additional pressure introduced by the Pauli exclusion principle. This pressure is the reason why, usually, a fermionic cloud is much more extended than a bosonic one.

1.3.3 Controlling the interactions: Feshbach resonances

So far we have described the static properties of a non-interacting Fermi gas. However, the most interesting properties of a physical system emerge in presence of interactions. One of the most appealing properties of ultracold atomic gases is the possibility to tune the interactions' strength and nature using *Feshbach resonances*, thus allowing to explore different interaction regimes.
Neutral atoms interact via Lennard-Jones potentials $V(r) = -\frac{C_6}{r^6} + \frac{C_{12}}{r^{12}}$. The $-r^{-6}$ component of the potential is attractive and short ranged, meaning that it is negligibly small after a certain inter-particle distance r_0. However, at few a_0 distance (*Bohr's radius*, $a_0 \simeq 0.5\,\mathring{A}$) the electron clouds of the atoms start overlapping and the interaction becomes strongly repulsive due to the Pauli exclusion principle. This effect is included in the potential by the r^{-12} repulsive component.
As we have seen, in order to avoid three-body collisions, ultracold gases must be incredibly dilute. This means that the interparticle spacing is indeed much higher than the interaction range: $n\, r_0^3 \ll 1$. Therefore, the probability of having three-body interactions is negligible and we can consider only two-body elastic collisions. Since the degeneracy condition is given by $n\lambda_{dB}^3 \simeq 1$, in degenerate systems the typical atomic size is also much larger than the interaction range ($r_0 \ll \lambda_{dB}$). This means that when two atoms interact they do not feel the details of the short-range microscopic potential, but rather an effective potential averaged over the whole wavefunction, so that we can neglect the microscopic details of the potential.
The Lennard-Jones is a central potential $V(r)$ and the description of the scattering of two particles in such a potential is described in many quantum mechanics textbooks [25] and reviews [4, 26]. Away from the collision region the asymptotic scattered wavefunction can be written as the superposition of the incoming and scattered waves:

$$\psi_{as}(\mathbf{r}) \sim e^{i\mathbf{k}\cdot\mathbf{r}} + f(\mathbf{k},\mathbf{k}')\frac{e^{i\mathbf{k}'\cdot\mathbf{r}}}{r} \tag{1.22}$$

where $\mathbf{k}$ and $\mathbf{k}'$ are the incoming and outoing momenta respectively, and $f(\mathbf{k},\mathbf{k}')$ is the *scattering amplitude*. This last quantity describes the probability amplitude that the incoming wave is scattered in the direction $\mathbf{r} = \mathbf{k}'/k$, where $k' = k$ due to energy conservation. The scattering amplitude is related to the scattering cross section by the relation $\frac{d\sigma}{d\Omega} = |f(\mathbf{k},\mathbf{k}')|^2$, where Ω is the solid angle.

Since particles interact via a central potential, it is possible to write the scattered wavefunction with a partial wave expansion:

$$\psi_{as}(\mathbf{r}) = \sum_l Y_l^0(\theta)\frac{u_l(r)}{r} \tag{1.23}$$

where Y_l^0 are the spherical harmonics with $m = 0$ and $u_l(r)$ is the radial wavefunction. By inserting such expansion in the Schrodinger equation we get:

$$\frac{\hbar^2}{2m}(\partial_r^2 + k^2)u_l(r) = V_{eff}(r)u_l(r) \tag{1.24}$$

where $V_{eff}(r) = V(r) + \frac{\hbar^2 l(l+1)}{2mr^2}$ is the effective potential.
At low temperatures the centrifugal barrier $\frac{\hbar^2 l(l+1)}{2mr^2}$ inhibits collisions with $l > 0$, thus only $l = 0$ s-wave scattering is permitted. However, the wavefunction describing the collision between two identical fermions must be antisymmetric, which limits the partial waves expansion to odd values of l. Therefore, identical fermions in ultracold samples cannot interact with each other via s-waves because of symmetry reasons, while l-wave scattering is strongly suppressed by the low temperature. This means that identical ultracold fermions effectively do not interact with each other, which can be an undesired feature, since interactions are needed to evaporative cool the gas and to observe physically interesting phenomena. To overcome this limit it is possible to work with two different atomic species or, as we do, to work with mixtures of same-species atoms in two different hyperfine states. Since these states have a different spin, the antisymmetry of the wavefunction is taken over by the spin degree of freedom and the spatial component of the wavefunction must be symmetric. Therefore, fermions in different spin states can interact via symmetric s-wave scattering processes, which are effectively the only interactions present in an ultracold atomic sample.
Considering s-wave scattering only, the radial solution of Eq. 1.24 can be written as $u_0(r) \simeq \sin(kr - \delta_0(k))$, where $\delta_0(k)$ is the phase-shift imprinted on the scattered wavefunction by the collision. Introducing the *scattering length*

$$a = -\lim_{k\to 0}\frac{\tan(\delta_0(k))}{k} \tag{1.25}$$

we can approximate the interaction potential with a delta-like pseudopotential:

$$V_p(r) = \frac{4\pi\hbar}{m}a\delta(r). \tag{1.26}$$

This approximation is justified because, in cold atoms systems, the scattering length is typically orders of magnitude larger than the Lennard-Jones potential range r_0. Thus the interatomic interactions can be approximated by a contact potential of effective range $r_e = 0$ and the whole scattering process is described by the scattering length a whose sign and magnitude determine the properties of the potential. In the following we will briefly describe how we can tune the scattering length using Feshbach resonances, for a more comprehensive discussion on the topic we refer to the review in Ref. [3].
The interaction potential between two alkali atoms in two different hyperfine states depends on their electron spin configuration, identifying a triplet and a singlet potential. The state of the incoming particles defines which one of the two is the *open channel*, that is populated before the

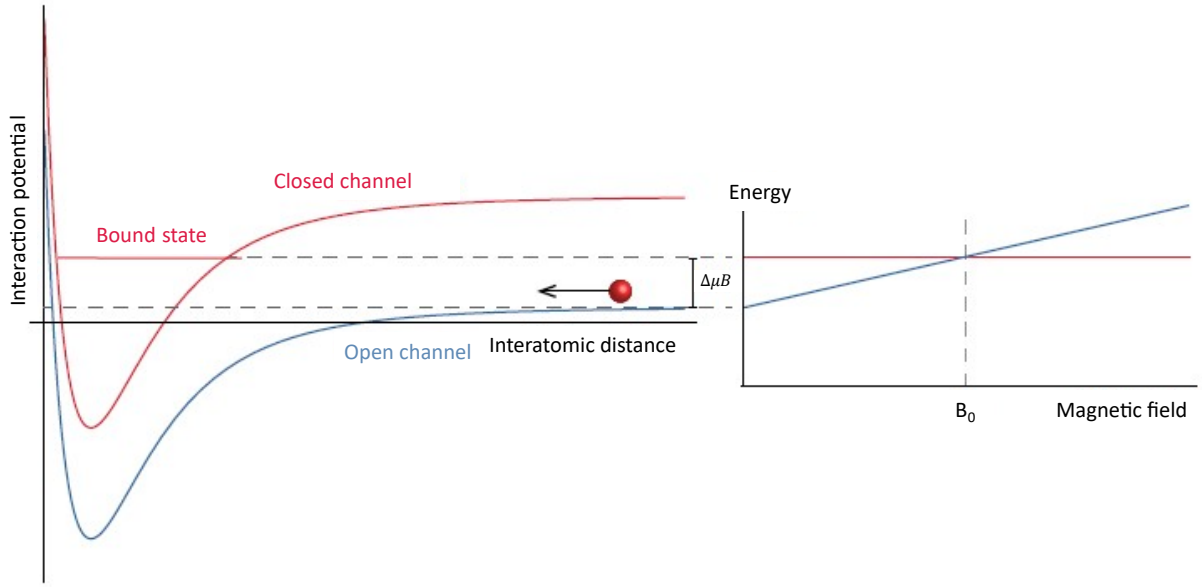

Figure 1.3: Resonant coupling between the closed and open channels. Closed and open channels for a scattering event (left): the closed channel presents a bound state that affects the properties of the scattering particles in the open channel. It is possible to tune the energy difference between the two channels with an external magnetic field (right). When $B = B_0$, the two channels are resonant and the scattering length diverges.

scattering event, while the other is the *closed channel*. Because of hyperfine coupling between the two channels, the presence of a bound state in the closed channel modifies the scattering properties of particles in the open one. In fact, a bound state in the interaction potential causes a divergence of the scattering length when its energy is resonant with the one of the scattering particles in the open channel. Usually this is not the case, however, since the open and closed channels have different magnetic moments, it is possible to exploit an external magnetic field to tune the energy difference between them. When the energy shift is such that the bound state in the closed channel is resonant with the particles' energy in the open one, the scattering length diverges, giving rise to a Feshbach resonance.
The phenomenological magnetic field dependence of the scattering length can be expressed as:

$$a(B) = a_{bg}\left(1 - \frac{\Delta B}{B - B_0}\right) \tag{1.27}$$

where a_{bg} is the off-resonance background scattering length, ΔB is the resonance width and B_0 is its center. When $B = B_0$ the scattering length diverges ($a \to \infty$) and interactions are the highest allowed in nature. However, none of the scattering process observables actually diverges as the cross section for s-wave scattering remains finite even for $a \to \infty$ [27]. One of the most appealing properties of Feshbach resonances is that it is possible to tune not only the size but also the sign of the scattering length, thus being able to explore different interaction regimes for both strongly and weakly interacting systems with either attractive ($a < 0$) or repulsive ($a > 0$) interactions.

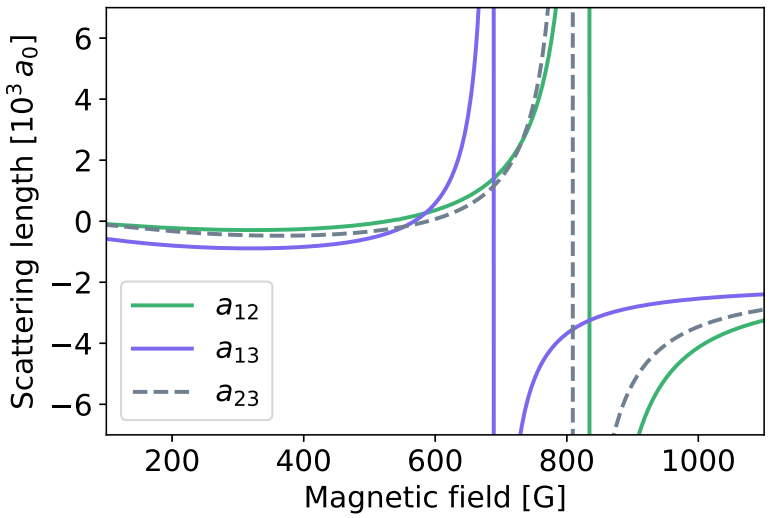

Figure 1.4: Feshbach resonances of the three lowest ^{6}Li hyperfine states. The scattering length of collisions between two atom in different states depends on the external magnetic field. Thus, by changing this magnetic field we can effectively tune the interaction strength and sign over a wide range. Data are taken from Ref. [28]

We report in Fig. 1.4 the Feshbach resonances of the three lowest Zeeman sublevels of ^{6}Li, which have very broad Feshbach resonances. Both $|1\rangle - |2\rangle$ and $|1\rangle - |3\rangle$ Feshbach resonances are about 250 G broad, enough to ensure a mild influence of magnetic field fluctuations on the scattering length. Feshbach resonances are a fundamental tool for producing ultracold Fermi gases in different interaction regimes and we exploit them extensively in all our experiments. In particular we exploit the 690 G $|1\rangle - |3\rangle$ resonance [3, 29] to produce a non-interacting or weakly interacting Fermi gas and the 832 G $|1\rangle - |2\rangle$ resonance to produce fermionic superfluids [27].

1.3.4 The BEC-BCS crossover

The tuning of interactions provided by Feshbach resonances, combined with the low temperatures achievable in ultracold Fermi gases allow to investigate the phenomenon of fermionic superfluidity. This kind of superfuidity arises from the pairing of atoms in opposite spin states due to the presence of strong interactions between them. Fermionic pairs are indeed bosons which can undergo Bose-Einstein condensation and display a superfluid behavior [4–6].
In particular, for attractive interactions the Fermi gas is unstable towards the formation of long-ranged Cooper pairs analogous to that described by the BCS theory of conventional superconductivity [9]. In the ideal zero-temperature regime even an infinitely small attractive interaction ($a \to 0^-$) is sufficient to induce pairing between fermions living near the Fermi surface. At finite temperature, instead, a stronger attraction is needed. This can be easily achieved by increasing the interaction strength between atoms with Feshbach resonances, so that for stronger attractive interactions the pairing temperature T^* is indeed higher. Instead, for sufficiently low interaction strength and $T > T^*$ the system is a weakly attractive Fermi gas. On the opposite side of the resonances, where interaction are repulse, the repulsive Fermi gas

is unstable towards the formation of tightly bound bosonic molecules. When $T > T_c$, where T_c is the critical temperature of the superfluid transition, the molecules are not condensed while they condense into a coherent system and become superfluid as temperature is lowered below T_c. This regime is that of the molecular Bose-Einstein condensate (mBEC), usually referred to simply as BEC regime fo fermionic superfluids.
Despite the differences in constituents, the BCS and BEC regimes are described by formally equivalent ground state wavefunctions and are thus smoothly connected by an intermediate regime. This is the unitary Fermi gas (UFG) region where interactions are the highest possible and the pair size is comparable to the interparticle spacing. The whole spectra of regimes is the so-called *BEC-BCS crossover* and its characterization has been one of the greatest achievements in the field of ultracold Fermi gases. [4, 5]. We report the BEC-BCS phase diagram of a homogeneous fermionic gas composed by atoms in two spin states in Fig. 1.5.

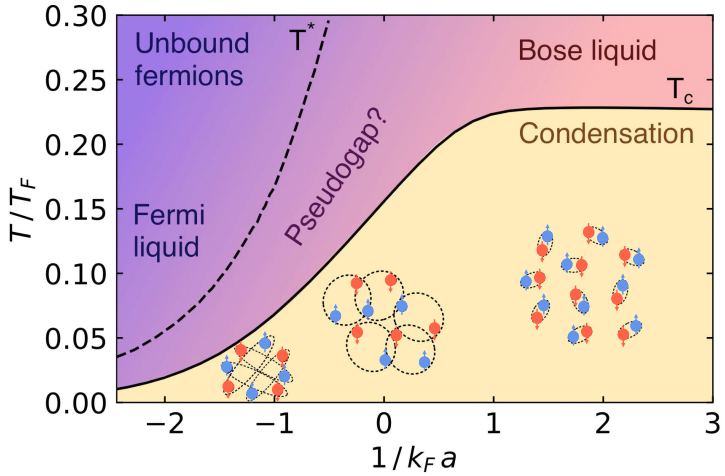

Figure 1.5: Phase diagram for the BEC-BCS crossover of an homogeneous fermionic gas. Below the pairing temperature T^* fermions in opposite spin states are coupled into pairs. The pair size depends on the interactions, which can be parameterized as $1/k_F a$, where k_F is the Fermi momentum and a is the s-wave scattering length that can be tuned with Feshbach resonances. By tuning the interaction strength between the two fermionic spin states it is possible to smoothly cross from a regime of tightly bound molecules to a regime of long-range Cooper pairs. In between these two extremes there is an intermediate regime where the pair size is comparable to the interparticle spacing and the interactions are the highest (UFG). When temperature is lowered below the critical temperature T_c, pairs undergo condensation, giving rise to fermionic superfluidity. The intermediate region $T_c < T < T^*$ where pairs are formed and not yet condensed is referred as pseudogap region, in analogy with high-T_c superconductors. The curves T^*/T_F and T_c/T_F are extracted from Ref. [4, 30].

A particularly interesting condition is that of temperature above the condensation temperature and below the pairing temperature: $T_c < T < T^*$. This region is expected to be characterized by the presence of "preformed" pairs, where fermions in opposite spin state are already paired but the pairs are not yet condensed. In the BCS-limit, where $T^* \to T_c$, condensation occurs at the same time as pairing, so no preformed pairs can exist, as is the case of conventional superconductors. However, as we increase the interaction strength towards unitarity we find

that it is possible to have uncondensed pairs. This is similar the molecular BEC case, where we can find thermal molecules above T_c. The presence of uncondensed pairs in the crossover region has attracted much attention since these preformed pairs also occur in a part of the phase diagram of high-T_c superconductors, which is called the pseudogap region [10]. Even though the existence of a pseudogap in ultracold Fermi gases is still under debate, this crossover region of $T > T_c$ is often referred as pseudogap in the phase diagram of fermionic gases as well. The investigation of the pseudogap regime is currently one of the main research themes in ultracold Fermi gases.

1.4 Cooling and manipulation of a ^{6}Li gas

Cooling an atomic gas to the degenerate regime is quite a complex process which requires many stages. In fact, atoms need to start from a rather high temperature to be in the gaseous phase and their slowing, cooling and trapping is obtained with a series of different techniques. All of these operations must be performed under Ultra-High-Vacuum (UHV) conditions, so that the atoms are isolated from external contaminants which would significantly affect our system.
The atomic sample is initially produced inside an oven, where an artificially enriched ^{6}Li sample is heated up to 420° to create an atomic beam which is successively collimated. The hot atomic beam is decelerated by a Zeeman slower down to a velocity of about 60 m/s before entering the science chamber where the real cooling and trapping are performed. Pressure inside the science chamber is kept below 10^{-11} mBar. Our cooling procedure starts with a standard Magneto Optical Trap (MOT) and a gray molasses subdoppler cooling [20]. Atoms are then transferred into an optical dipole where they are evaporatively cooled down to the degenerate regime. In the following we will briefly describe our cooling procedure, referring to Ref. [29] for a more detailed description.

1.4.1 Laser setup

Laser light is the fundamental tool for cooling and manipulating atomic samples. In our experimental setup we use laser sources of different wavelengths to perform different operations. We use resonant light for the first stages of cooling and for imaging our sample, while we employ non-resonant light for the generation of the optical potentials that we use for evaporative cooling and for manipulating our ultracold atomic gas.
As we have seen, the D_1 and D_2 lines of ^{6}Li are both at almost 671 nm but are separated by around 10 GHz, which prevents addressing them with a single laser source. Therefore, to address the two transitions we use two Toptica TA-Pro lasers and we amplify them with one Master Oscillator Power Amplifier (MOPA) each. The frequencies of D_1 and D_2 lasers are locked to the respective atomic transition with a Saturation Absorption Spectroscopy (SAS) setup. In particular, the D_2 laser is locked to the $|^2S_{1/2}, F = 3/2\rangle \rightarrow |^2P_{3/2}, F' = 5/2\rangle$ transition and the D_1 is locked to the $|^2S_{1/2}, F = 3/2\rangle \rightarrow |^2P_{1/2}, F' = 1/2\rangle$ transition. Since the natural linewidth of the D_2 line ($\Gamma \simeq 6$ MHz) is larger than the hyperfine splitting of the excited state (4.4 MHz), the hyperfine structure is not resolved in the absorption spectrum. Therefore, even though the $|F = 3/2\rangle \rightarrow |F' = 5/2\rangle$ transition is theoretically closed, we can't avoid that, as we cool atoms using this transition, some of them decay in the $|^2S_{1/2}, F = 1/2\rangle$ hyperfine state and are lost from the cooling cycle. To recover these atoms we employ rempuper lights that pump the lost

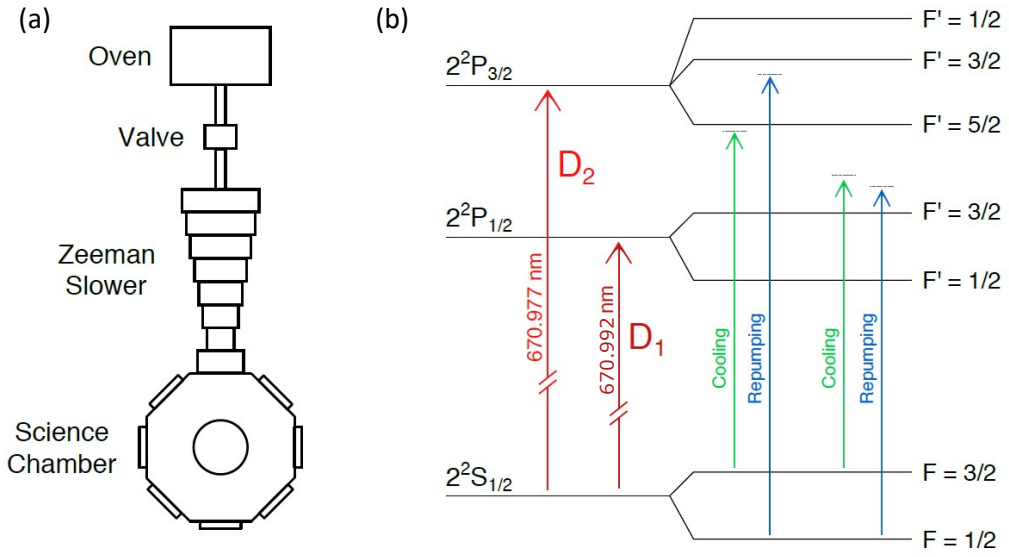

Figure 1.6: Experimental apparatus for the production of ultracold fermionic gases of ^{6}Li. (a) Vacuum system for the production of the sample. A collimated atomic beam exits the oven, it is slowed down by the Zeeman slower and reaches the science chamber, where it is cooled to degeneracy. (b) Zero field structure of ^{6}Li. We highlight the cooling and rempumping transitions for both the D_1 and D_2 lines.

atoms to the $|F' = 3/2\rangle$ state for both the D_1 and D_2 transitions. Since the ground state hyperfine splitting is 228 MHz large, we can use the D_1 and D_2 lasers for producing both the cooling and rempumping lights for their respective transition. The fine tuning of the wavelength between the cooling and repumping beams is done using a chain of Acousto-Optics Modulators (AOMs) [29]. The D_2 light is also used for imaging the atomic cloud by means of an absorption imaging technique. Using an optical waveplate and a polarizing beam splitter (PBS) we can couple the imaging light in one of two different optical fibers. Depending on the chosen fiber we can either shine our imaging light from the top of the science chamber (vertical imaging) or from the side (horizontal imaging), to observe atoms from different directions.
To manipulate the atomic gas with optical potentials we employ two different wavelengths. We use far red-detuned light for trapping our atoms in an attractive optical dipole trap (ODT) where we perform evaporative cooling. Once we have an ultracold sample, we can switch on far blue-detuned lights that provide repulsive potentials through which we can spatially manipulate our atomic gas [27]. In particular, for the evaporation process we employ two high-power infrared beams: the IPG and the Mephisto. The former is a 1073 nm laser with a maximum power of 200 W that is used to trap the atoms after the MOT phase and to perform a first evaporation. The latter is a 1064 nm laser with a maximum power of 50 W that crosses the IPG with a 14° angle to create the final ODT for completing the evaporation process. The intensities of both these beams, as well as of all the other beams we employ in our setup, are tuned and stabilized by AOMs controlled with PID feedback loops. To manipulate the geometry and the dimensionality of our atomic cloud we use two beams derived from the same Coherent Verdi V-8 laser source. This is 532 nm green light that is far blue-detuned from the lithium D-line

and provides a very good tool for manipulating our atoms with repulsive optical potentials and negligible absorption probability. The first green beam that we use is a $TEM_{(0,1)}$ beam that we can shine in the science chamber from the horizontal direction to squeeze our sample along the vertical direction. This allows us to confine our atomic gas in an oblate, nearly two-dimensional geometry [24, 27]. The second repulsive beam that we employ is instead shone on our sample from the bottom, along the vertical direction. Before entering the science chamber, this beam impinges on a Digital Micromirror Device (DMD, see Chapter 3), which allows us to manipulate the spatial intensity profile of the light. Using the DMD and an high numerical aperture objective (more on this in the following section), we are able to shine high-resolution tailored light on our cloud and thus manipulate our atomic sample with arbitrarily shaped optical potentials [22–24, 27].
As we will see in Chapter 3, we have another laser source that emits near-resonant light at 671 nm that we employ for the realization of the spin-dependent and spin-selective optical potentials.

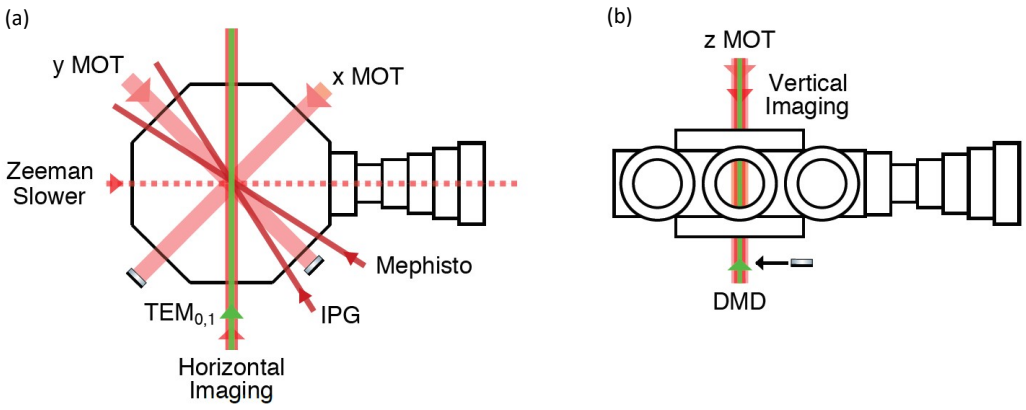

Figure 1.7: Sketch of the laser beams employed to manipulate the atomic cloud in the science chamber in a top view (a) and in a side one (b). The Zeeman slower beam is depicted as red dashed line and it is switched off as soon as the atoms enter the science chamber. x and y MOT beams are retroreflected by static mirrors, while the z one has a movable mirror that retroreflects the beam during the MOT stage. The mirror is then removed to free the way for the imaging and DMD beams, impinging on the atom cloud from top and bottom, respectively. The angle between the IPG and Mephisto beams is 14°, while the $TEM_{(0,1)}$ beam is collinear to the horizontal imaging one.

1.4.2 Cooling the atoms to degeneracy

The hot atomic beam exiting the oven needs to be slowed down before entering the science chamber. To do so, we employ a Zeeman slower [17, 18] that decelerates our atoms from a velocity of around 800 m/s down to 60 m/s thanks to the interplay between a counterpropagating laser beam resonant with the D_2 transition of the outgoing atoms and an inhomogeneous magnetic field that keeps the light resonant with the atomic transition as atoms slow down.
The slowed beam is then captured in a Magneto Optical Trap [17, 18] composed by three

retroreflected laser beams, one for each spatial direction, and a quadrupolar magnetic field produced by a pair of coils in anti-Helmholtz configuration. The MOT exploits the magnetic field and the retroreflected laser beams to both cool the atomic sample and trap it in the center of the quadrupole field. In the MOT stage we trap 10^9 atoms with a temperature of around 500 μK in 5/6 seconds. The minimum theoretical temperature achievable in a MOT is restricted to the Doppler temperature ($T_D = 140\,\mu$K for ^{6}Li). For most alkali atoms, sub-Doppler cooling below T_D is generally achieved with Sisyphus cooling in optical molasses [17, 18, 31]. However, in ^{6}Li the standard sub-Doppler mechanism is hindered by the unresolved hyperfine splitting of the $^2P_{3/2}$ level. To achieve sub-Doppler cooling, we exploit a scheme based on gray molasses acting on the D_1 transition [20]. Therefore, when the loading in the MOT is completed, we switch off the MOT lights and field while we switch on the D_1 molasses light. With this sub-Doppler cooling process we are able to lower the temperature of our sample to about 50 μK.
After this gray molasses stage, atoms are loaded into the optical dipole trap for evaporative cooling. The sample is transferred into the IPG beam where we perform a second stage of gray molasses and a first evaporation, where we lower the intensity of the beam with an exponential ramp. After this first ramp, the IPG beam is crossed with the Mephisto so that we have a crossed-beam dipole trap [21] where we complete our evaporation with another exponential ramp. At the end of the evaporation our sample is composed by around 10^5 atoms per spin state at a temperature of the order of 30 nK. Our gas is trapped in a cigar shaped potential formed by the two infrared crossed beams.
To optimize the evaporation, we ramp the Feshbach magnetic field to 832 G, on top of the $|1\rangle-|2\rangle$ resonance (see Fig. 1.4), so that the interactions are the highest possible and thermalization is enhanced. It is worth noting that before ramping up the Feshbach field the atoms are in the zero field ground state, namely the $F = 1/2$ hyperfine sublevel of the $^2S_{1/2}$ manifold, and it is only when we ramp the Feshbach field that this ground state is split into the $|1\rangle$ and $|2\rangle$ sublevels. To produce fermionic superfluids we keep the Feshbach field at 832 G for the whole evaporation process, and we change it only at the end of the evaporation for varying the $|1\rangle - |2\rangle$ scattering length and exploring different interaction regimes. To produce a non-interacting Fermi gas, we employ a different evaporative protocol that we will describe in section 1.5.

1.4.3 High resolution imaging and manipulation

We extract information on our atomic sample, such as number of atoms, temperature and density distribution, by means of absorption imaging. By shining resonant light pulses on the cloud and recording the shadow cast by the atoms on a camera we are able to acquire an image of our sample. Using two different optical paths, we can take images of our sample both from the horizontal and vertical directions. In order to focus and magnify the atoms' image on the camera, we use a simple telescope in the horizontal direction and a more sophisticated high-resolution microscope objective in the vertical one.
The horizontal imaging setup is composed by a telescope of two $f_1 = 150$ mm and $f_2 = 1000$ mm lenses, providing a magnification of 6.87. The atoms image is focused on an Andor Ultra camera, set on the Fast Kinetic Series (FKS) acquisition mode, which allows to take a sequence of a few images with a short delay time of the order of 200 μs, at the price of using a smaller portion of the CCD chip [32]. Each camera pixel is a 16 μm $\times$ 16 μm square, that, considering the magnification factor corresponds to a 2.3 μm side square on the atoms. In between the

horizontal imaging path, we can add a movable imaging setup with a low magnification of 0.5, that we use for checking the MOT cloud and the efficiency of the IPG loading. For this secondary horizontal imaging, the light is focused on a Stingray camera by a movable $f_S = 75$ mm lens.

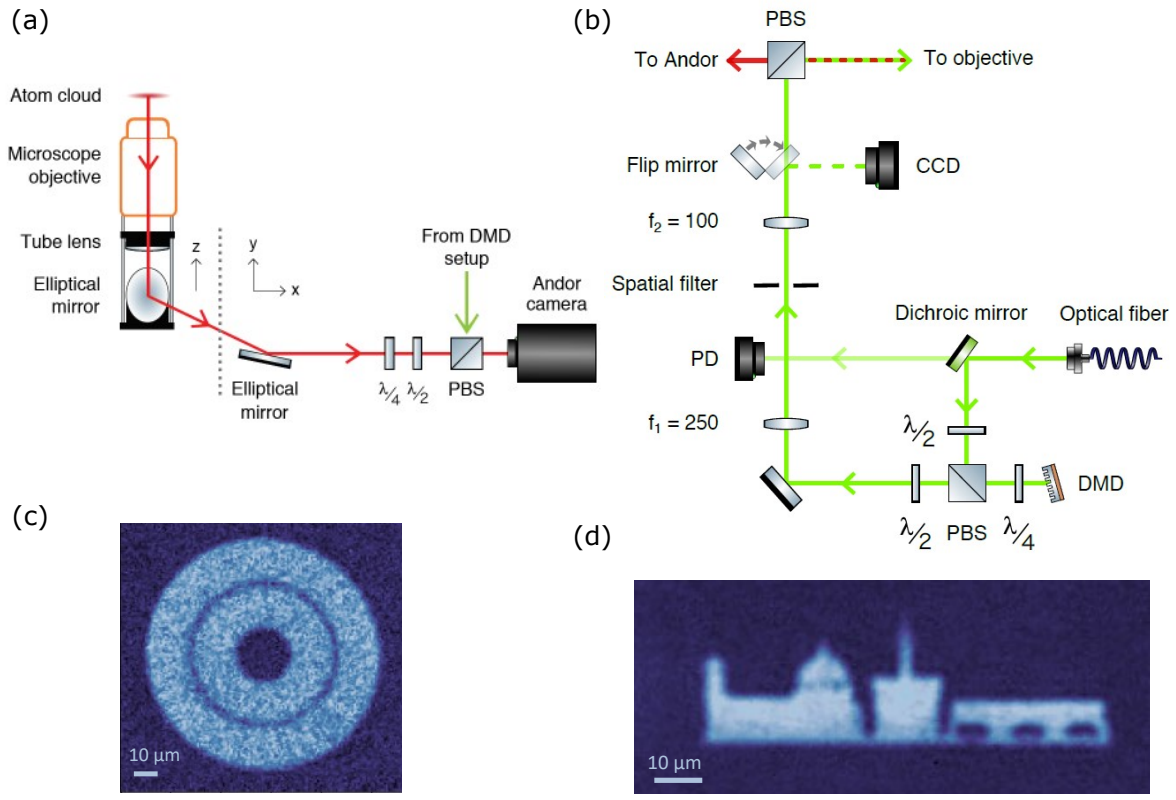

Figure 1.8: Vertical imaging setup. (a) Optical path of the resonant imaging light. The light is shone from the top of the chamber and it is focused on the Andor camera with the microscope objective and a lens. Using a set of two waveplates we tune the polarization of the imaging beam so that it is fully transmitted through the PBS. (b) Optical path of the DMD light. After a first telescope, the DMD light is reflected by the PBS towards the objective and the atomic cloud so that we can produce arbitrarily shaped optical potential. (c) Projection of a double torus potential on a quasi-2D atomic cloud. (d) Projection of the Florence skyline.

The vertical imaging system is thoroughly described in Ref. [27]. Its main element is a high-resolution, high numerical aperture, microscope objective custom made by Special Optics. The microscope objective features the same focal point for both resonant light at 671 nm and blue-detuned light at 532 nm, so that it can be employed both for imaging the atomic cloud and projecting DMD-tailored optical potentials on the atomic cloud with a high resolution. The resolution of this imaging system, defined as the minimum distance between two objects to appear separated on the imaging plane, is below one micron for both 671 and 532 nm light. The imaging light is focused on an Andor IXon3 EMCCD camera via a $f = 1000$ mm lens, resulting in a total magnification of $M = 21.8$.
Both the vertical imaging beam and the z-MOT beam are shone from the top of the cell. Since

the z-MOT beam must be retroreflected, we need to have a mirror in the imaging path, which will, of course, block the imaging light. To avoid this, we use a motorized movable mirror that we insert during the MOT stage of each experimental cycle and that we remove after the MOT loading is completed to clear the path for the other vertical beams (imaging and DMD potentials).
To image the atomic cloud we use short (4 μs) pulses of high intensity ($I \simeq I_s$) resonant light. We use an AOM for finely tuning the frequency of the imaging light so that we can be resonant with the transition from either one Zeeman sublevel or the other and we can selectively image atoms in the two spin states. From the Lambert-Beer law (see Ref. [27] for details) we are able to determine the atomic density integrated along the vertical direction as:

$$n_{2D}(x,y) = -\frac{\alpha}{\sigma_0}\ln\left(\frac{I_{out}}{I_i n}\right) + \frac{\alpha}{\beta}\frac{1}{\sigma_0}\frac{I_{in}-I_{out}}{I_s} \tag{1.28}$$

where $\sigma_0 = \frac{3\lambda^2}{2\pi}$ is the ideal value of the absorption cross section while α and β are parameters that relate the ideal and effective cross section and saturation intensity respectively. I_{in} and I_{out} are the incident and transmitted intensities that we measure with the fast kinetic acquisition mode of our cameras. In particular, both from the horizontal and vertical direction, we take three successive images separated by 200 μs. The first is an image of the atoms' shade that allows us to measure I_{out}, the second is an image of the imaging beam in absence of the atoms, yielding I_{in}. The third is a dark, background image that we use to remove any offset in the two previous images.
As mentioned, the vertical imaging setup is not used only for imaging the atomic sample, but also for projecting arbitrarily tailored optical potentials on the cloud. To generate the repulsive potentials we use 532 nm blue-detuned light and we shape its intensity profile using a Vialux V-7000 High-Speed Module DMD, whose properties and characterization can be found in Ref. [27, 33]. As we will see in more detail in Chapter 3, the DMD is composed by an array (1024×768 for this model) of tiltable micromirrors that act as a light mask: when light is shone on the DMD, the spatial intensity profile of the reflected beam depends on the state of each micromirror. By individually controlling these mirrors, it is possible to shape the light intensity so that the outgoing beam has the desired intensity profile. To shine such tailored potentials on the atomic cloud with high resolution we take advantage of the vertical imaging setup. We combine the green DMD beam and the red imaging on a PBS in such a way that the the imaging light is transmitted towards the camera while the DMD beam is reflected towards the atomic cloud. This beam passes through the imaging setup and it is thus demagnified by a factor 21.8. However, before the beam enters the imaging path we already demagnify it by a factor 2.52 using a two-lenses telescope. Therefore the total demagnification of the DMD image is 54.99, resulting in a 0.25 μm size of each micromirror in the atomic plane. Thanks to this vertical setup, we are able to both manipulate and image our atomic sample with very high spatial resolution.

1.5 Production of a non-interacting Fermi gas

The presence of broad Feshbach resonances between the three lowest Zeeman state of ^{6}Li allows to prepare systems in many different interactions regimes. Between such regimes, there is the possibility to effectively cancel any interatomic interaction and produce an ideal, non-interacting Fermi gas. In principle, an ultracold Fermi gas composed by atoms in one state only is really a

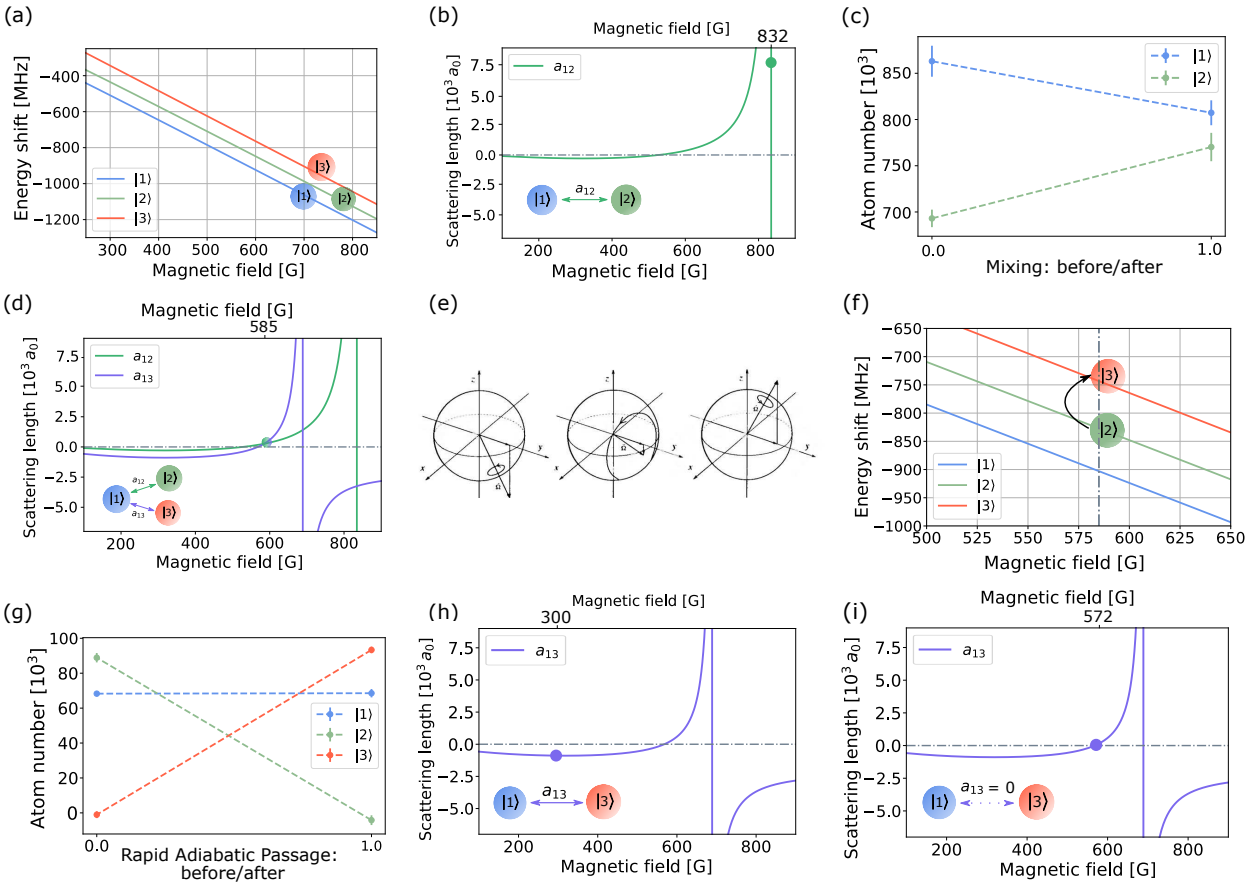

Figure 1.9: Overview of the protocol for producing a non-interacting Fermi gas. (a) Hyperfine states of ^{6}Li at the working magnetic fields. (b) The evaporation starts with atoms in states $|1\rangle$ and $|2\rangle$ on top of the $|1\rangle - |2\rangle$ Feshbach resonance (832 G) in order to enhance thermalization. (c) Using a fast RF source we mix the atoms in the two states so that we have a balanced population with $\sim 50\%$ atoms in each spin state. (d) We sweep the magnetic field to 585 G where $a_{12} = a_{13}$. Here we transfer atoms from $|2\rangle$ to $|3\rangle$. (e) Representation of the Adiabatic Rapid Passage on the Bloch sphere. As the detuning of an external RF drive is swept around resonance, the Bloch vector follows adiabatically from the ground ($|2\rangle$) to the excited ($|3\rangle$) state. Image taken from Ref. [18]. (f) The $|2\rangle \rightarrow |3\rangle$ frequency transition is 80 MHz. Through our RF source we are able to excite atoms from $|2\rangle$ to $|3\rangle$. (g) Effect of the Rapid Adiabatic Passage on the states' population. While atoms in state $|1\rangle$ are not affected, all the atoms in state $|2\rangle$ are successfully transferred to $|3\rangle$. (h) Our $|1\rangle - |3\rangle$ mixture is evaporated at 300 G. (i) After evaporation we sweep the magnetic field to 572 G where the a_{13} Feshbach resonance has a zero-crossing. We now have a non-interacting Fermi gas composed by atoms in states $|1\rangle - |3\rangle$.

non-interacting system due to the antisymmetry of the fermionic wavefunction and the suppression of interactions via $l > 0$ waves. However, to cool an atomic sample we need interactions so that the system thermalizes during the evaporative cooling process. Therefore, to produce a non-interacting Fermi gas we have to prepare the system in two spin states and use Feshbach resonances to cancel the interaction between atoms with different spin. Here we describe

our experimental protocol to produce such system and how we can measure its properties with absorption imaging.

1.5.1 Experimental protocol

Since interactions play a fundamental role in enhancing thermalization during evaporative cooling, as we cool down our sample we make extensive use of the different interactions regimes at our disposal. An overview of all the stages for the preparation of a non-interacting Fermi gas is given in Fig. 1.9. We start from the usual 832 G $|1\rangle - |2\rangle$ resonance and we use radio-frequency (RF) pulses to mix the population of the two states so that we have $\sim$50% atoms in each spin state (*mixing*). Our RF source is provided by a fast circuit that has been developed in our laboratory [34]. After a brief evaporation at 832 G, we change the Feshbach field before reaching the pairing temperature in order to avoid the formation of bonds between atoms in different states. We sweep the magnetic field to about 300 G, where interactions are not strong enough to enter the superfluid regime. However, as visible in Fig. 1.9, the $|1\rangle - |3\rangle$ resonance is much more favorable for the evaporation at such field, presenting a scattering length a_{13} that is almost 3 times a_{12}. In order to exploit this resonance, we need to transfer the atoms from $|2\rangle$ to $|3\rangle$ before moving to 300 G. Therefore, immediately after the beginning of the evaporation, we sweep the magnetic field down to 585 G, where $a_{12} \simeq a_{13}$ and here we transfer the population from $|2\rangle$ to $|3\rangle$ by means of RF pulses. In particular, we employ the Rapid Adiabatic Passage (RAP) technique to transfer the whole population of $|2\rangle$ in the $|3\rangle$ state [32]. By sweeping the detuning between our RF and the $|2\rangle \rightarrow |3\rangle$ transition (80 MHz), we are able to adiabatically transfer atoms from $|2\rangle$ to $|3\rangle$. This happens because the Bloch vector $\vec{R}$ describing the state of each atom precedes around the vector $\vec{\Omega}$, whose direction is changed from the south to the north pole of the Bloch sphere as the detuning is swept around resonance [18, 35]. Once we have a sample composed by atoms in $|1\rangle$ and $|3\rangle$, we sweep down the field to 300 G where the rest of the evaporative process takes place. As the scattering length a_{13} is much lower at 300 G than on top of the resonance, the evaporation ramps for the ideal Fermi gas have to be slower than the ones employed for fermionic superfluids, lasting about 3 s more. At the end of the evaporation, the Feshbach field is swept to 572 G where $a_{13} = 0$ and the $|1\rangle - |3\rangle$ mixture is non-interacting. Typically, we can produce up to 10^5 atoms per spin state at $T/T_F \simeq 0.1$, where $T_F = E_F/k_B$ is the Fermi temperature of our system.

1.5.2 Thermometry of a Fermi gas

As we have seen, we extract information from the atomic cloud via absorption imaging. By measuring the light intensity absorbed by our sample we are able (see Eq. 1.28) to determine the two dimensional atomic density integrated in the imaging direction (vertical/horizontal). We can then appropriately fit this density profile in order to find the physical quantities of interest. We consider a non-interacting Fermi gas trapped in a harmonic potential and we assume that the thermal energy $k_B T = 1/\beta$ is much larger then the quantum mechanical level spacing $\hbar\omega_{x,y,z}$ (*Thomas-Fermi approximation*). The density distribution of the thermalized Fermi gas is then [4]:

$$n_{th}(\mathbf{r}) = \int \frac{d^3\mathbf{p}}{(2\pi\hbar)^3} f(\mathbf{r},\mathbf{p}) = -\frac{1}{\lambda_{dB}^3} Li_{3/2}(-e^{\beta(\mu - V(\mathbf{r}))}) \tag{1.29}$$

where $Li_n(z)$ is the n^{th}-order polylogarithmic function, related to the gamma function and Riemann zeta function that naturally appear in integrals over the Bose-Einstein and Fermi-Dirac distributions. The polylogarithmic function smoothly interpolates between the $T \ll T_F$ regime near the center of the trapping potential and the higher temperature regime of the atoms in the outer region. Therefore, for very cold Fermi gases, temperature affects only the far wings of the density distribution. While for thermal clouds above T_F the size of the cloud is a direct measure of temperature, for cold Fermi gases we need to extract the temperature from the shape of the distribution's wings.

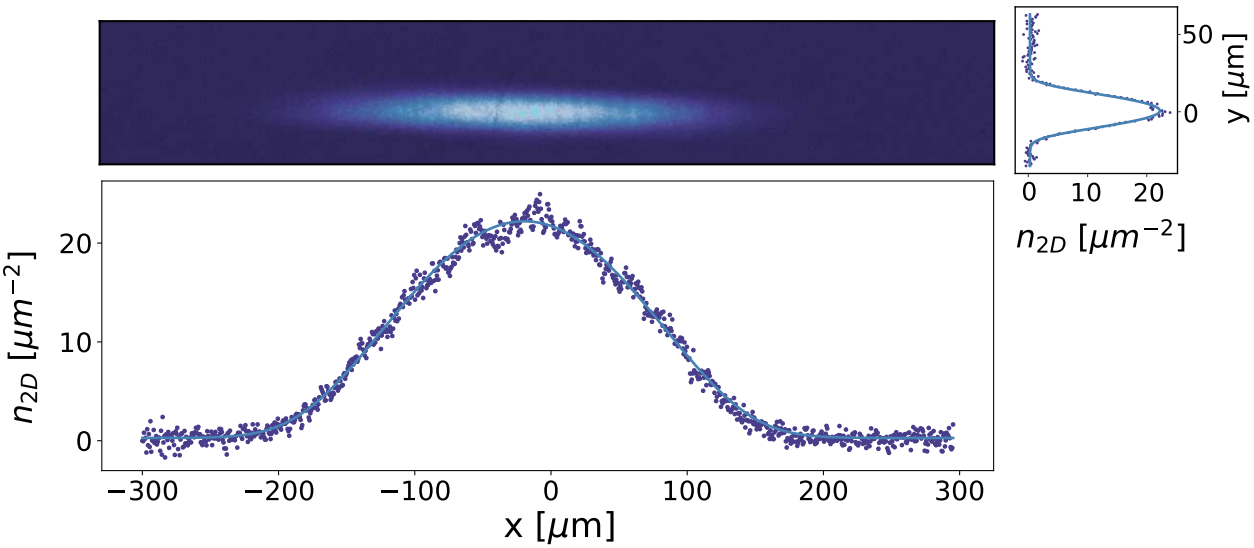

Figure 1.10: In-situ image of a non interacting Fermi gas trapped in the crossed optical dipole trap. The image consist of an average over about 10 experimental realizations. We report the density profile integrated along the x and y directions. Fitting the density with Eq. 1.31 allows to estimate the temperature of our sample as $T/T_F = 0.11(1)$, corresponding to ~ 50 nK.

In the classical regime at $T/T_F \gg 1$, the density distribution reduces to the Maxwell-Boltzmann distribution and the characteristic cloud size is given by the gaussian radius $\sigma_i = \sqrt{\frac{2k_BT}{m\omega_i^2}}$. In the degenerate regime, instead, the cloud size saturates at the Thomas-Fermi radius R_{Fi} (see Eq. 1.21). It is thus convenient to define a fit parameter describing the cloud size that interpolates between the two limits [4]:

$$R_i^2 = \frac{2k_BT}{m\omega_i^2} f(e^{\beta\mu}) \longrightarrow \begin{cases} \sigma_i & T \gg T_F \\ R_{Fi} & T \ll T_F \end{cases} \tag{1.30}$$

where $f(x) = \frac{1+x}{x}\ln(1+x)$. For all temperatures R_i is directly related to the size of the cloud and it is thus a better fit parameter than σ_i and R_{Fi}. We can fit the density profile of a thermal non-interacting Fermi gas imaged from the vertical (z) direction with [4]:

$$n_{2D}(x,y) = n_{2D,0} Li_2 \frac{\left(-\exp\left[\beta\mu - (x^2/R_x^2 + y^2/R_y^2) f(e^{\beta\mu})\right]\right)}{Li_2\left(-e^{\beta\mu}\right)} \tag{1.31}$$

where $n_{2D,0}(1-\frac{x^2}{R_{Fx}^2})$ is the zero-temperature distribution and $n_{2D,0}$ is the peak density of the cloud. With this expression we can fit the measured density profile of our cloud and find the fundamental parameters β and μ describing the properties of our system. Once we know these values we can find the degeneracy parameter T/T_F as [4]:

$$\tilde{T}/T_F = \left[-6Li_3\left(-e^{\beta\mu}\right)\right]^{-1/3}. \tag{1.32}$$

However, we find that the actual degeneracy parameter T/T_F of the cloud is well approximated by $T/T_F \simeq \sqrt{\xi}\,\tilde{T}/T_F$ [23], where $\xi \simeq 0.37$ is the universal Bertsch parameter [36]. This method is particularly robust against fluctuations of the image background, since it relies on a two-dimensional fitting procedure, and yields a reliable estimation of the cloud temperature.
The number of atoms in the observed spin state can be obtained from the total absorption recorded in the camera image. The transmission of resonant light for the pixel in position (x, y) is given by $P(x,y) = e^{-\sigma_0 \int n_{3D}(x,y,z)dz}$, where σ_0 is the resonant atom-photon cross section for light absorption and $n_{3D}(x,y,z)$ is the 3D density of the cloud [4]. The number of atoms in state i is then:

$$N_i = \frac{A}{M\sigma_0}\sum_{pixels} -\ln(P(x,y)) \tag{1.33}$$

where A is the area of a pixel and M the optical magnification. Considering the peak optical density of the cloud $n_{2D,0}$ and fitting the density profile of our sample we find:

$$N_{fit} \longrightarrow \frac{A}{\sigma_0}\begin{cases}\frac{\pi}{3}\, n_{2D,0}\,\tilde{R}_{Fx}\tilde{R}_{Fy} & T \ll T_F \\ \pi\, n_{2D,0}\,\tilde{\sigma}_x\tilde{\sigma}_y & T \gg T_F\end{cases} \tag{1.34}$$

where $\tilde{R}_{Fi}$ and $\tilde{\sigma}_i$ are the Thomas-Fermi and gaussian radius in the i-direction respectively, measured in camera pixels.

Chapter 2

Spin transport in fermionic systems

The coupling between the motion of particles and their spin degree of freedom plays a fundamental role in defining the transport properties of many materials. In this chapter we will describe the fundamental features of spin transport in correlated Fermi systems. In the first part of this chapter we will describe spin transport in solid state materials, introducing the fields of *spintronics* and *spin caloritronics*. In the second part of this chapter we will show how we can quantum simulate the spin transport properties of different systems in the framework of ultracold Fermi gases, with particular focus on ^{6}Li atoms with tunable interactions. Finally we will introduce the idea of spin manipulation using spin-dependent optical potentials and we will show how this allows to access new physical phenomena and to address open questions concerning spin transport in highly-correlated Fermi systems.

2.1 Spin transport in electronic materials

The transport properties of solid state materials stem from their internal lattice structure. Vibrations of atoms around their equilibrium positions result in heat propagation, while mobile particles such as electrons and holes can carry electric charge across a metallic material. However, electrons, and consequently holes, do not carry only charge as they posses another fundamental, intrinsically quantum, property: spin.
Many of the properties of solid state materials are indeed related to the spin degree of freedom of the electrons composing them. All magnetic properties arise from the presence of spin-spin correlations and correlations between electrons with opposite spin orientation lead to the formation of Cooper pairs, the building block of conventional superconductivity [9]. The presence of such attractive correlations between electrons with opposite spin is also acknowledged as the most promising theory for describing the properties of high T_c cuprate superconductors [10]. Antiferromagnetic correlations play a fundamental role also when a localized spin impurity interacts with the surrounding bath. This effect, known as the Kondo effect [8], is responsible for the increase of the low temperature resistivity of doped metals and for the enhancement of conductance through quantum dots [37]. Other than in quantum dots, the spin degree of freedom can affect the electronic transport properties of other low-dimension systems, such as graphene or two-dimensional magnetic nanostructures [38]. Such coupling between spin and charge currents in meso- or nanoscopic structures has drawn the attention of the scientific community due to promising technological applications.

As most spin investigations have been focused on the magnetic properties of matter, until recently charges and spins have been considered separately and little interest has been directed towards the electronic transport of spin. This spin transport has been somehow overshadowed by the great interest towards charge currents for their application in charge-based electronic devices. However, after decades of constant advance, the development of electronic devices with ever increasing performances seems to be slowing down. Due to the high miniaturization required by state-of-the-art technologies we are currently observing the breakdown of Moore's law, as further decreases in feature size and transistor speed go in parallel with intolerable levels of ohmic energy dissipation associated with the motion of electrons in conducting circuits [39]. One way of addressing this issue is to look for a new electronics paradigm, that is to develop circuits based on the spin degree of freedom of the electron. Either adding the spin degree of freedom to conventional charge-based electronic devices or using spin alone as information carrier has the potential advantages of increased data processing speed and decreased electric power consumption. However, the successful incorporation of spin control into electronic devices requires solving a number of technical issues concerning the injection, manipulation and detection of spin polarization as well as of spin-polarized currents [11].
Historically, the first theoretical hint at the realization of spin currents was the development of the so-called *two-current* model for explaining the unusual behavior of the low temperature resistance in ferromagnetic metals [40]. In fact, at sufficiently low temperatures electrons with magnetic moment parallel and antiparallel to the magnetization of a ferromagnet, being the majority or minority component respectively, do not mix in scattering events. The conductivity can then be expressed as the sum of two independent and unequal parts for the two different spin components, so that currents in ferromagnetic materials are spin polarized.
The first experimental demonstration of the coupled manipulation of electrons and spins was provided by the discovery of the giant magnetoresistance (GMR) in 1988 [13, 14]. GMR is a quantum mechanical effect observed in the resistance of superlattices composed by alternated layers of ferromagnetic and non-magnetic metals. In such structures, it is possible to significantly change the electrical resistance by acting on the relative orientation of the magnetization of adjacent ferromagnetic layers. In fact, due to the dependence of electron scattering on spin orientation, the electrical resistance is much lower for parallel than for antiparallel alignment. Since the magnetization direction can be controlled, for example, by applying an external magnetic field, GMR provided the experimental breakthrough for manipulating electronic currents through the spin degree of freedom. GMR is at the basis of magnetoresisitve-random-access-memories (MRAMs) which are non-volatile random-access-memories where data are stored in magnetic domains so that they can be retained without any applied power.
The discovery of GMR and its subsequent applications triggered the development of a new field of research and technology, namely *spintronics*, whose main goal is to understand how to manipulate the electrons' spin degree of freedom for the development of new spin-based solid state quantum devices.

2.1.1 Spintronics

After the discovery of GMR, a great number of spintronics devices have been proposed, where the spin degree of freedom complements or replaces charge as the information carrier. These devices combine standard microelectronics with spin-dependent effects that arise from the interaction

between the spin of the carrier and either the magnetic properties of the material or externally applied electromagnetic fields.
The paradigmatic spintronics device is the so-called Datta-Das *spin field-effect transistor* (SFET) [15]. The structure of the SFET, of which we report a scheme in Fig. 2.1, is analogous to that of a three terminals field-effect transistor (FET) with a drain, a source and a gate for controlling the current in the narrow channel connecting drain and source. The gate either allows the current to flow (ON) or does not (OFF). In usual FETs this control is provided by an applied voltage, which alters the conductivity of the channel. In the Datta-Das SFET instead, the source and the drain are ferromagnetic materials and, since a current flowing through a ferromagnet gets polarized, the electrons injected in the channel by the drain have a well-defined spin orientation (usually parallel to the transport direction). Electrons are transported ballistically through the semiconductor channel and their spin is detected when they arrive at the drain. In a simplified picture, the electron can enter the drain (ON) if its spin points in the same direction of the drain magnetization, otherwise it is scattered away (OFF). The gate generates an effective magnetic field arising from the spin-orbit coupling in the semiconductive material, from the confinement geometry of the transport channel and from the electrostatic potential of the gate. This effective magnetic field causes the electrons' spins to precess and, by modifying the gate voltage, it is possible affect the precession so that the electrons' spins at the drain will be either parallel or antiparallel to the magnetization, effectively controlling the current.

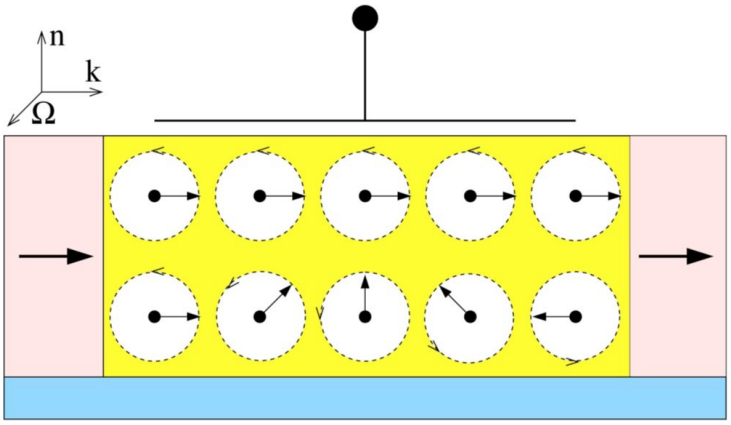

Figure 2.1: Scheme of the Datta-Das spin field-effect transistor (SFET). The source (spin injector) and the drain (spin detector) are ferromagnetic metals or semiconductors, with parallel magnetic moments. The injected spin-polarized electrons move ballistically along a quasi-one-dimensional channel formed by a semiconductive material. Electron spins precess around the effective field Ω, which arises from spin-orbit coupling and which is defined by the structure and the properties of the channel. The magnitude of Ω is tunable by the gate voltage. If the electron spin at the drain is parallel to its initial direction (top row), which can happen when e.g. the precession period is much larger than the traveling time in the channel, then the current is large. The current is instead the smallest if the spin direction a the drain is reversed (bottom row). Image is taken from Ref. [12].

The Datta-Das SFET exploits spin-orbit coupling (SOC) in semiconductors for introducing a spin precession and thus controlling the current flowing in the device. Spin-orbit interactions

arise from relativistic corrections to the electronic Hamiltonian and result in a coupling between the spin and the momentum of an electron in an external potential $V(\mathbf{r})$. We can write such Hamiltonian as [38, 41]:

$$H(\mathbf{r}, \mathbf{p}) = \frac{p^2}{2m} + V(\mathbf{r}) + H_{SO} + H_Z \tag{2.1}$$

where the first two terms account for the electron kinetic energy and the external potential respectively. The last two terms, instead, are the spin-orbit Hamiltonian H_{SO} and the Zeeman Hamiltonian H_Z and are related to the electron spin $\mathbf{s}$. We can write such terms as:

$$\begin{aligned} H_{SO} &= \frac{\hbar}{2m^2c^2} \left(\nabla V(\mathbf{r}) \times \mathbf{p}\right) \cdot \mathbf{s} \\ H_Z &= g\mu_B \, \mathbf{s} \cdot \mathbf{B} \end{aligned} \tag{2.2}$$

where μ_B is Bohr's magneton, $\mathbf{B}$ is an external magnetic field and g is the Landé g-factor which has a value of 2 for a free electron but it can vary greatly and even be negative for electrons in semiconductors [41]. Both the spin-orbit interaction and the Zeeman effect lead to a splitting of the conduction bands of semiconductor materials into two energy bands, populated by electrons with opposite spin projection. This energy splitting can be exploited for the manipulation of electron spins in semiconductor devices.

As the Datta-Das SFET, most of the proposed spintronics devices are based on the SOC instead than on the Zeeman effect. This is because of the interest in integrating the spin degree of freedom in existing non magnetic semiconductor devices and manipulating it by purely electrical means, without external inhomogeneous magnetic fields. Modern day spintronics is mainly focused on semiconductor materials because doping, gating and heterojunctions can be used to engineer different material properties and because of the intimate relationship between optical and transport properties in semiconductors. However, the injection and sustainment of spin currents in non-magnetic semiconductors is indeed one of the main fundamental and technical issues that need to be addressed for realizing efficient spintronics devices.

One of the proposed ways for injecting spin currents in semiconductors is through the spin Hall effect, in which flowing electrons experience orthogonal, spin-dependent forces, analogous to the magnetic Lorentz force in the conventional Hall effect. However, in the spin Hall effect the forces have opposite signs for two spin states, due to the spin-orbit interaction resulting in anisotropic scattering of electrons with different spin orientation. This leads to an accumulation of opposite spins on opposite sides of the sample so that a transverse spin current arises in response to a longitudinal charge current, without the need for magnetic materials or externally applied magnetic fields [41]. An anisotropy of the spin-orbit interaction may arise due to the presence of impurities (extrinsic spin Hall effect) or from asymmetries in the material itself, such as reduced dimensionality (intrinsic spin Hall effect) [42]. Both extrinsic [43] and intrinsic [44] spin Hall effects have been observed in semiconductor materials and the intrinsic spin Hall effect has been reproduced with a bosonic quantum gas [45].

The spin Hall effect is a viable way of injecting a spin current in a spintronic device. Other proposed methods for generating polarized out-of-equilibrium spin populations include optical techniques in which circularly polarized photons transfer their angular momenta to electrons or electrical spin injection with magnetic electrodes, similarly to the case of the Datta-Das SFET [12].

The injection of a spin polarization or current is only one of the technological and fundamental issues concerning the development of spin-based devices. Other central questions relate to the loss of such spin orientation, namely spin relaxation, and to the detection of spins in solid state materials. When we have spin accumulation, that is an out-of-equilibrium spin polarization that may induce, or be induced by, a spin current, the spin population relaxes back to equilibrium at a certain rate. Also, spin relaxation phenomena lead to a finite size of the non-equilibrium spin accumulation. If such accumulation is provided by a local spin injector such as a magnetic electrode, then its spatial extent will be given by the spin diffusion length, after which the polarization relaxes back to its equilibrium value.
The two main processes that lead to spin equilibration are spin relaxation and spin dephasing [12]. Their theoretical and experimental investigation plays a central role in spintronics since only when the spin polarization is sufficiently long lived (typically a few nanoseconds) the spin degree of freedom can be used to encode and carry information. This two equilibration processes have usually different timescales, namely T_1 for spin relaxation and T_2 for spin dephasing. Considering not one but an ensemble of electrons, relaxation and dephasing are often referred to the average value of the electron spin, that is the magnetization $\mathbf{M} = \langle \mathbf{s} \rangle$. The equations describing spin precession and decay, as well as the diffusion of the magnetization in an applied magnetic field $\mathbf{B(t)} = B_0 \hat{z} + \mathbf{B}_1(t)$, with a longitudinal constant component B_0 defining the quantization axis and a time-dependent transverse component $\mathbf{B}_1$, are [12]:

$$\begin{aligned} \frac{\partial M_{x,y}}{\partial t} &= \gamma (\mathbf{M} \times \mathbf{B})_{x,y} - \frac{M_{x,y}}{T_2} + D_s \nabla^2 M_{x,y} \\ \frac{\partial M_z}{\partial t} &= \gamma (\mathbf{M} \times \mathbf{B})_z - \frac{M_z - M_z^0}{T_1} + D_s \nabla^2 M_z \end{aligned} \tag{2.3}$$

where $\gamma = \mu_B \, g/\hbar$ is the electron gyromagnetic ration, D_s is the spin diffusion coefficient and $M_z^0 = \chi B_0$ is the thermal equilibrium magnetization with χ denoting the system's static susceptibility. These phenomenological equations are equivalent to the optical Bloch equations describing the dynamics of a two-state quantum system interacting with electromagnetic radiation. Expressions for the relaxation times T_1 and T_2 can be obtained from a microscopic description of the electronic motion [12, 41]. From a phenomenological point of view, T_1 describes the relaxation rate of the longitudinal magnetization due to phenomena such as spin-flipping in scattering events between electrons and impurities or phonons. T_2 is instead related to the dephasing of an ensemble of transverse electron spins, initially precessing in phase around the longitudinal field and losing their phase due to fluctuations of the precessing frequencies. Typically, these relaxation times are of comparable size and are usually considered as a single relaxation time τ_s of the order of 1 ns. Instead the single spin decoherence time τ_{sc} is usually shorter than τ_s, and can be as small as a few picoseconds. While τ_s is relevant for spin transport applications τ_{sc} sets the timescale for solid state spin-based quantum computing so that understanding the microscopic mechanisms of spin decoherence and how to inhibit them may help in the development of spin-based quantum computers.
The last fundamental challenge of manipulating spins in solid state materials is spin detection. Spin detection typically relies on sensing changes in signals caused by the presence of non-equilibrium spin populations or currents in the system. This is usually done by either a ferromagnetic drain such as that of the Datta-Das transistor or by optical means. In the latter case it is customary to use spin light-emitting diodes (LEDs) where, due to spin-polarized carriers,

the emitted light is circularly polarized, thus allowing to detect the spin polarization. However, as for spin injection, many issues remain to be solved before achieving efficient detection of the spin degree of freedom of solid state electrons with high sensitivity.
Despite the many challenges, the great interest in the realization of spin-based devices has led to a fast development of the field of spintronics. Being born from the investigation of ferromagnetic properties of metals, spintronics has now extended to the study of spin transport in many promising materials from semi- [41] to superconductors [46], including interfaces between different materials [47], nanostructures and low dimensional materials such as graphene [38]. All these research areas focusing on spin transport in different materials are already branching into new subfields of spintronics. Further, even other research fields are emerging from the investigation of spin manipulation in solid state systems, including researches on spin-based quantum computing and on the coupled transport of heat and spin currents, namely spin caloritronics [39].

2.1.2 Spin caloritronics

While spintronics investigates the coupled transport of electronic spin and charge in condensed-matter structures and devices, the field of spin caloritronics focuses on the interaction of spins with heat currents. The interest in the coupled transport of spin and heat is motivated by newly discovered physical effects that hold promises of applications in the development of thermoelectric devices [39].
Thermoelectric effects arise from the coupling of heat and charge currents and are already widely diffused in both in scientific and commercial areas. The two most well-known thermoelectric effects are the development of an electromotive force in conducting materials due to a temperature gradient, namely the Seebeck effect, and its reverse process of a heat flow originating from an electric current that is the Peltier effect. While heat is always generated by flowing currents due to dissipative Joule heating, the Seebeck and Peltier effects are thermodinamically reversible processes which can be exploited in many devices, including thermocouples for temperature measuring and generators that convert waste heat into additional electrical power. However, despite decades of research into thermoelectric materials and applications, the efficiency of such devices has remained low. One promising approach for increasing the efficiency and versatility of thermoelectric devices involves exploiting the spin of the electron, in addition to its charge and heat-transport properties.
Since heat currents also interact with spin currents, the investigation of out-of-equilibrium phenomena related to spin, charge and energy transport in magnetic structures and devices has led to the emergence of spin caloritronics. This new field combines conventional thermoelectronics, that does not consider spin transport, and conventional spintronics, which instead does not consider heat transport. This research in the coupling of heat and spin transport in magnetic materials emerged at first as a branch of spintronics but it is recently acquiring its own independent visibility. Further, spin calorinotrics does, in a sense, run parallel to spintronics in the race for developing new sustainable devices with improved computational power, as one of the main issues with further miniaturization of electronic components is excessive ohmic dissipation. Spintronics proposes to deal with this by encoding information in the spin instead of charge of electrons while spin caloritronics may offer ways of either containing this unwanted heating or exploiting it as waste heat.

Since the electrons involved in thermoelectric effects are indeed spin-1/2 particles, spin-dependent Peltier and Seebeck effects are expected to arise from spin currents or to generate them respectively. The microscopic description of thermoelectric effects stems from the thermal broadening of the Fermi-Dirac distribution (Eq. 1.15) in presence of a temperature gradient. As temperature is increased the step-like profile of the Fermi-Dirac distribution around the Fermi energy (E_F) gets smoothed, as more electrons have sufficient thermal energy to occupy states above the Fermi energy. Thus, the hot electrons above E_F diffuse from the low-temperature to the high temperature regions of the conductive materials. Since holes below the Fermi energy flow in the opposite direction, a net charge current is obtained whenever the electron and hole flows are somehow different [39]. Including the spin degree of freedom, we can describe an electric current as the sum of two currents corresponding to the two spin states of the electron (two-current model [40]). If the energy of the two spin states is split by spin-orbit coupling or by external magnetic fields, it is possible that the temperature-induced current described above will indeed be a spin current.
Considering two spin states($|\uparrow\rangle$, $|\downarrow\rangle$), we can phenomenologically write the spin current $\mathbf{J}_s = \mathbf{J}_\uparrow - \mathbf{J}_\downarrow$ and the spin-heat current $\mathbf{Q}_s = \mathbf{Q}_\uparrow - \mathbf{Q}_\downarrow$ as [48]:

$$\begin{pmatrix} \mathbf{J}_s \\ \mathbf{Q}_s \end{pmatrix} = \sigma_s \begin{pmatrix} 1 & S_s \\ TS_s & \frac{k_s}{\sigma_s}(1 + Z_s\, T) \end{pmatrix} \begin{pmatrix} \mathbf{F}_s \\ -\nabla T_s \end{pmatrix} \tag{2.4}$$

where $\mathbf{F}_s = \mathbf{F}_\uparrow - \mathbf{F}_\downarrow$ is the spin force, $T_s = T_\uparrow - T_\downarrow$ is the spin temperature, T is the equilibrium temperature, σ_s is the spin conductivity, k_s is the spin-heat conductivity and $Z_s = \sigma_s S_s^2/k_s$ is a parameter describing the efficiency of the spin thermoelectric effect. S_s is the spin-dependent Seebeck coefficient which relates the spin chemical potential $\mu_s = \mu_\uparrow - \mu_\downarrow$ and the spin temperature gradient: $\nabla\mu_s = S_s \nabla T_s$. The spin-dependent Peltier coefficient is related to the spin-dependent Seebeck coefficient by the Onsager reciprocity relations connecting reciprocal flow of thermodynamic and can be written as TS_s. Notably, the above expression Eq. 2.4 is not strictly valid in bulk solid state materials where spin-dependent temperatures T_s and heat flows $\mathbf{Q}_s$ are often quenched by interspin and electron-phonon scattering, so that T_s and $\mathbf{Q}_s$ should be substituted by their spin-insensitive counterparts T and $\mathbf{Q}$. However, for nanoscopic or very cold systems, including quantum gases [48–50], such scattering processes can be suppressed and a spin-dependent temperature may arise.
Both the spin-dependent Seebeck and Peltier effects have been experimentally observed in solid state magnetic|non-magnetic interfaces and in nanostructures [39]. Further, other spin-heat phenomena are currently under investigation in ferromagnetic materials where the effects may originate from sources other than conduction electrons. This is the case of the spin-Seebeck effect (not to be confused with the aforementioned spin-dependent Seebeck effect) where heat currents induce collective thermal excitations of the magnetic order parameter, namely spin waves [51]. This phenomenon has been unexpectedly observed in magnetic materials and the hunt for detecting its Onsager reciprocal, the spin Peltier effect, as well as thermoelectric relativistic effects such as a thermal spin Hall is currently on [39].
Despite the many open questions, the promise of useful applications such as highly localized thermopower generation or nanoscale refrigeration have drawn a growing interest towards spin caloritronics phenomena. In this context, where many predicted effects have yet to be observed, while others have popped out unexpectedly, the alternative approach of quantum simulating spin-heat phenomena with ultracold quantum gases may offer a valuable contribution to this

emergent field of physics.

2.2 Spin transport in ultracold Fermi gases

In the last decades, the investigation of spin transport in solid state materials has drawn considerable attention due to both technological and fundamental reasons. As we have seen, understanding the fundamental mechanisms favouring or obstaculating the out-of-equilibrium manipulation of the spin degree of freedom in solid state materials may contribute to the development of the next generation of spintronics and spin caloritronics devices. Further, many of the most interesting and exotic systems across all fields of physics display strong quantum correlation which are often related to the spin degree of freedom. Describing such spin correlations may help shed light on the fundamental many-body phenomena underlying the macroscopic properties of such strongly correlated systems both in and out-of-equilibrium.
However, the accurate spin manipulation and detection required for investigating such fundamental phenomena in solid state materials are rather difficult to achieve. As we have seen, the spin of electrons in condensed matter systems is not an easily accessible degree of freedom and the injection and detection of spin currents in solid state materials are research area themselves. Moreover, solid state systems are actually rather complex environments where the presence of scatterers such as impurities, phonons or other electrons leads to fast spin relaxation rates and short coherence times, often being in the nanoseconds range or below. Though this typical timescales can be tuned by working at lower temperatures or in particular geometries, they represent an evident obstacle to the investigation of quantum phenomena underlying the properties of solid state materials.
Even though the complexity of such systems is indeed a reason behind the great interest towards them, it also leads to difficulties in their theoretical description. Since it is nearly impossible to include all the processes involved in out-of-equilibrium materials in a single theory, it is often necessary to work with an increasing-complexity approach and include only the most relevant phenomena in mean-field theories, adding other effects as successive corrections. While this simplifying procedure can be done in theoretical works, it is impossible to exclude certain phenomena from real-life systems where all processes may be strongly intertwined. Other theories, such as Landau's Fermi liquid theory, tend to treat many-body phenomena by appropriately renormalizing the parameters of an ensemble of non-interacting quasiparticles. However, there are systems where correlations and interactions are so strong that Fermi liquid and mean-field descriptions fail. This often prevents direct comparison between first-principles theories and experiments, thus forestalling a full understanding of many complex systems.
In this context, an increasing interest is being directed towards the investigation of spin transport in ultracold Fermi gases. In fact, ultracold atoms can be exploited to quantum simulate a wide range of quantum systems and are particularly well suited for the investigation of spin transport phenomena. The Zeeman sublevels of alkali atoms provide a simple way of encoding the spin degree of freedom in an atomic system. In fact, the interaction between magnetic fields, which are ubiquitous in ultracold atoms experiments, and the atomic angular momentum results in a splitting of the electronic ground state into different Zeeman sublevels labeled by different spin quantum numbers. This is the case of the $|1\rangle$, $|2\rangle$, $|3\rangle$ states of ^{6}Li but the same is true for other commonly used alkali atoms such as rubidium or potassium. These states have a different nuclear spin projection along the quantization axis, usually defined by the external magnetic

field, and can thus be used to investigate spin related phenomena. In particular, considering fermionic isotopes, ensembles of atoms in different Zeeman states are used to quantum simulate electrons in different spin states.
Encoding the spin degree of freedom in the internal energy levels of atoms results in rather easy spin manipulation and detection. When the energy difference between atoms in different spin states is large compared to the linewidth of the optical transition used for imaging them, it is possible to selectively image the two spin states. In this way, the detection of spins in a mixture of atoms in different spin states can be achieved by simply imaging the different components independently. This is the case of the Zeeman states of ^{6}Li, whose energy splitting is of the order of 80 MHz, compared to a 6 MHz linewidth of the D_2 transition used for imaging them. In non-alkali atomic species, where the Zeeman splitting can be to low to be optically resolved, it is still possible to detect spins by mapping the spin states into either different states with a much higher, and thus resolvable, energy difference or by spatially separating the spin states with a spin-dependent optical force [52].
Beside detection, atomic spin states in alkali atoms can be easily manipulated with electromagnetic radiation in the radiofrequency (RF) range. As we have seen, it is possible to use RF pulses to drive transitions between different spin states to produce either balanced or spin-imbalanced mixtures. Radiofrequency transitions can also be exploited as a spectroscopic tool to investigate the energy spectra of spin states in different experimental conditions [4]. We will see that it is also possible to use laser light to either selectively and locally remove spin components from an atomic sample or to spatially manipulate them using spin-dependent or spin-selective optical potentials. As we have seen in Chapter 1, Feshbach resonances are another fundamental tool for the manipulation of spin in atomic systems as they can be exploited to tune the interactions between atoms in different spin states, thus allowing to investigate spin transport in regimes where spin states interact either very weakly or very strongly [3].

2.2.1 Spin transport across different interaction regimes

Due to its light mass and broad Feshbach resonances, ^{6}Li is one of the best suited atomic isotopes for investigating fermionic spin transport in different interaction regimes. The interaction strength in fermionic quantum gases is usually parameterized by $1/k_F a$, where $k_F = \sqrt{2mE_F/\hbar}$ is the Fermi momentum (considering an homogeneous system for simplicity) and a is the s-wave scattering length that can be tuned with Feshbach resonances. As we have seen in the previous chapter, we can produce both weakly ($|1/k_F a| > 1$) and strongly ($|1/k_F a| \simeq 1$) interacting systems, with either attractive ($1/k_F a < 0$) or repulsive interactions($1/k_F a > 0$). To discriminate between weak and strong interactions, we take into account k_F since, in a degenerate Fermi system, k_F sets the typical interparticle spacing. Therefore, we call weakly interacting a system where the interparticle spacing is smaller than the scattering length and strongly interacting a system where the two length scales become comparable. In the extreme case of diverging scattering length $1/k_F a \to 0$, the interactions are the highest possible and the system is in the UFG regime. This regime has attracted particular interest since the divergence of the scattering length leaves k_F as the only remaining length scale and the Fermi energy E_F as the only energy scale. Thus, the properties of a UFG do not depend on the nature of its constituents and an atomic gas at unitarity shares universal properties with other strongly interacting systems such as neutron stars and quark-gluon plasma [53].

For weak interaction strength the system is well described by Landau's Fermi liquid theory where the ensemble of interacting fermions is described as a non-interacting Fermi gas with the "bare" particles substituted by quasiparticles. The Fermi liquid picture successfully describes many of the most common fermionic systems, including electrons in a normal metal, liquid helium-3 and nucleons inside the atomic nucleus. However, we are now aware of many systems where this picture breaks down. Interacting fermions in one dimension [54], heavy fermions and high-T_c superconductors near their quantum critical point [55] and other strongly correlated materials are all systems that cannot be described by simple Fermi liquid behavior. The power of ultracold quantum gases is that, by tuning the interaction strength, it is possible to purposefully move away from the Fermi liquid regime and investigate the properties of all the aforementioned systems.
Many spin transport experiments in ultracold atomic gases are performed by spatially separating atoms in the two spin components, hereafter called $|\uparrow\rangle$, $|\downarrow\rangle$, and observing spin currents develop as the two components diffuse in the trapping potential [56, 57]. This diffusion can be captured by the magnetization continuity equation [58]:

$$\frac{\partial \mathbf{M}}{\partial t} + \frac{\partial \mathbf{J}_{s,i}}{\partial x_i} = \mathbf{M} \times \boldsymbol{\omega}_L \tag{2.5}$$

where $\mathbf{M}(\mathbf{r}, t)$ is the local magnetization, $\mathbf{J}_s(\mathbf{r}, t)$ is the spin current and $\boldsymbol{\omega}_L$ is the Larmor frequency of the magnetization precession. In fact, the magnetization is a Bloch vector in spin space and may evolve due to either a spin current or to an external torque. This torque may lead to spin rotation and to the precession of the spin current around the magnetization axis, in the Legget-Rice effect [58]. While this phenomenon can indeed be investigated with ultracold Fermi gases [59], in this work we focus only on the longitudinal components of the spin current and neglect the rotational term in Eq. 2.5.
Considering the even simpler picture of a one dimensional system we can write [56]:

$$J_s = -D_s \frac{\partial (n_\uparrow - n_\downarrow)}{\partial x} \tag{2.6}$$

where $n_{\uparrow,\downarrow}$ are the densities of atoms in the two spin states and D_s is the spin diffusion coefficient.
Spin diffusivity does indeed depend on both temperature and scattering length. At high temperatures $T \gg T_F$, where T_F is the Fermi temperature, the system can be considered classical and D_s will be determined by the kinetic theory of gases. When the gas is degenerate and weakly interacting, instead, it can be described by Fermi liquid theory. In either case we can write [58]:

$$D_s = v\, l_{mfp} = v^2\, \tau_D \tag{2.7}$$

where v is the root-mean-square (quasi)particle velocity, l_{mfp} is the mean free path and τ_D is a characteristic diffusion time. When spin is efficiently transported through the system with large mean free path between collisions, the spin diffusion coefficient is maximum. This is the case of both the high-temperature and Fermi liquid limits. In the classical limit, the high-temperature diffusion coefficient has the universal behavior $D_s \propto \left(\frac{T}{T_F}\right)^{3/2}$ so that diffusivity increases with increasing temperature [56, 58]. On the other hand, the diffusivity of an unpolarized Fermi liquid at $T \ll T_F$ increases with decreasing temperature as $D_s \propto T^{-2}$. This is due to fermionic

excitations near the Fermi surface becoming long lived quasiparticles, leading to longer τ_D.
A very different behavior of D_s is observed in strongly interacting systems near the superfluid transition. Here the mean free path between collisions is $l_{mfp} \simeq 1/k_F$ and the root-mean-square velocity is of the order of the Fermi velocity $v \simeq v_F = \hbar k_F/m$. Therefore, in a strongly interacting system diffusivity has a minimum value $D_s \simeq \hbar/m$, where m is the particles' mass [56, 58]. This is an example of a transport bound in which quantum mechanical scattering imposes a lower bound on a transport coefficient, setting a quantum limit of diffusion that depends only on $\hbar$ and the particles' mass. This bound arises due to the strong interactions breaking the quasiparticle picture at unitarity, where interactions are so strong that no long lived quasiparticle survives and transport is suppressed by frequent atomic collisions. In such case, the transport properties of the system do not depend on the system itself, but have a universal behavior shared by all strongly interacting Fermi systems. For this reason, the investigation of spin transport in strongly interacting Fermi gases can help shed light on the spin transport properties of other strongly correlated fermionic systems across all fields of physics.
To the spin diffusivity minimum at strong interactions corresponds a maximum of the spin drag coefficient Γ_{sd} [56–58]. This coefficient is defined as the rate of momentum transfer between atoms in opposite spin states and it is therefore related to the collision rate. Typically, Γ_{sd} is measured, along with the spin diffusion coefficient, by observing the relative motion of two spin imbalanced clouds moving towards one another (*spin-dipole mode*). Considering the relative position of the centers of mass of the two spin states $d(t) = \langle x_\uparrow(t) - x_\downarrow(t)\rangle$, its motion inside a trapping potential, such as that provided by a crossed optical dipole trap, follows the equation of a damped harmonic oscilator [58]:

$$\ddot{d}(t) + \Gamma_{sd}\,\dot{d}(t) + \omega_x^2\, d(t) = 0 \tag{2.8}$$

where ω_x is the trap frequency along the considered direction. This expression shows that spin drag results in an effective viscosity damping the spin current. The microscopic origin of this drag is related to atoms in opposite spin states colliding and transferring momentum between each other, thus suppressing the spin current in case of counter propagating spin states. Another consequence of spin drag is that when atoms in only one spin state are moving, the collisions with atoms in the other state should set the latter into motion [60]. This results in a suppression of the spin current as both spin states will eventually move together. As expected, the spin drag effect is stronger in presence of stronger interactions and Γ_{sd} has indeed an opposite behavior compared to the spin diffusivity having a maximum in correspondence of the diffusivity minimum.
The last fundamental quantity relevant to spin transport is the spin susceptibility $\chi_s = \frac{\partial(n_\uparrow - n_\downarrow)}{\partial(\mu_\uparrow - \mu_\downarrow)}$. This quantity describes the spin response to an infinitesimal chemical potential difference $\mu_\uparrow - \mu_\downarrow$ between the two spin states [56]. In non-degenerate systems the susceptibility follows the Curie law $\chi_s \propto 1/T$, while it is described by Fermi liquid theory at lower temperatures. As T is lowered below the the critical temperature for the superfluid transition, χ_s is expected to drop as bound singlet pairs may prevent the development of a spin current.
In fact, since superfluidity arises from pairs of bound fermions in opposite spin states, spin currents are expected to be strongly suppressed in superfluids, as atoms with opposite spin follow one another resulting in a suppression of spin transport. This is expected to result in negligible spin diffusivity and the highest spin drag coefficient between all possible regimes. From this reasoning emerges that it is not the superfluid phase itself that is spin-insulating, rather it is the presence of bound fermionic pairs that prevents the developing of a spin current.

Therefore, investigating spin transport in a paired system could provide information on the pairs themselves. While the spin-insulating behavior of the superfluid regime has been observed in the spin transport properties of a quantum point contact [61, 62] many questions, including the presence of transport bounds and the stability of the superfluid and of the pairing to spin-dependent perturbations remain open.
Investigating spin transport in a paired system by trying to inject a spin current, which can be achieved by setting in motion only one spin state, may help to further probe its spin insulator properties. The injection or non-injection of spin currents can be used to probe the stability of the superfluid and of the pair-binding across different regimes. Other ways of probing the stability of the superfluid include temperature, scattering length and, focusing on the spin degree of freedom, population imbalance [4]. Considering the BCS side, a balanced gas below the critical temperature is unstable towards Cooper pairing for arbitrarily weak attractive interactions and the pairs condense as soon as they are formed, resulting in superfluid behavior. Instead, in an imbalanced case the superfluid will become normal for too weak interactions as the spin imbalance suppresses pairing. This effect gets stronger as the imbalance is increased, eventually leading to a normal fluid behavior at all interaction regimes for a highly polarized Fermi gas, where pairing is strongly suppressed. Therefore, by imbalancing the relative population of the two spin states of an attractive Fermi gas it should be possible to tune its spin transport properties from a perfect spin insulator to a very good spin conductor.
Spin transport and the effect of the spin degree of freedom on transport properties can indeed be investigated in both paired and unpaired systems, exploiting temperature, population imbalance and Feshbach resonances to access different regimes within a single physical system.

2.3 Spin transport with spin-dependent optical potentials

As we have seen, by spatially separating atoms in opposite spin states and then letting them propagate in the trapping potential it is possible to investigate spin diffusion in different interaction regimes. The two spin populations are often segregated using a magnetic field gradient that induces opposite motion to the two spin states. This requires working at a magnetic field for which one spin state is attracted by a low magnetic field (low field seeker) whereas the other is attracted by a high magnetic field (high field seeker). The behavior of atomic states in inhomogeneous magnetic fields is determined by the slope of their energy $E(B)$ (see Fig. 2.2 (a)): states with a positive slope have lower energy for lower magnetic fields and are low field seekers while states with a positive slope are high field seekers. In the case of ^{6}Li, but this is true for all alkali atoms, the Paschen-Back regime, where the experimentally relevant spin states share the same slope, is attained at rather low magnetic fields, so that separating spin states with a magnetic field gradient requires working at fields of the order of 1-50 G [56, 57]. As shown in Fig. 2.2, such values are indeed very far from the Feshbach resonances located at 700-800 G so that it is not possible to tune the interaction strength as the two spin states are separated. To investigate spin currents in strongly interacting systems, the spin states are thus segregated into spin imbalanced reservoirs, possibly adding an optical barrier between to prevent any overlap [57], and only then interactions are ramped up as the two spin states are let free to move towards each other. This allows to access fundamental spin transport properties, such as the spin diffusivity and the collisional spin drag coefficient. However, this approach does have some limitations.

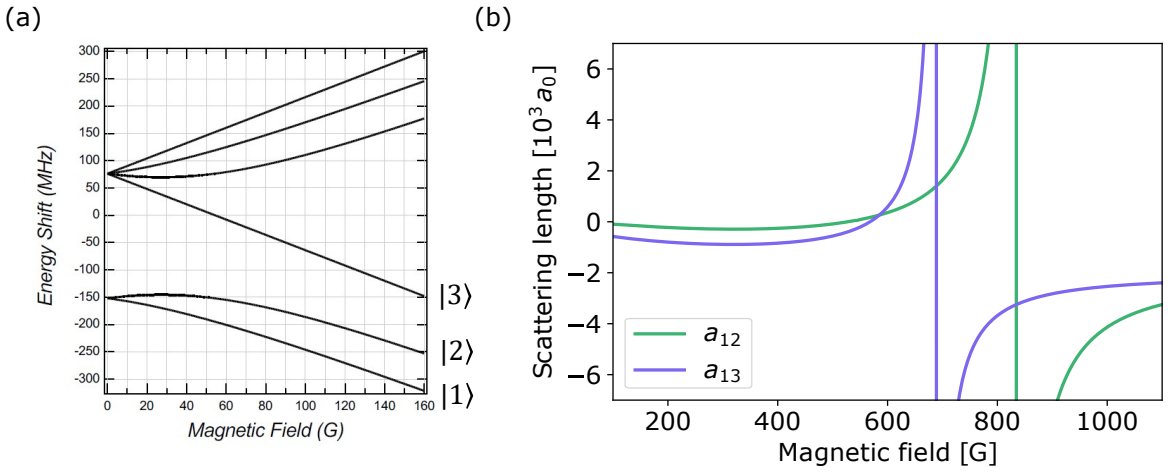

Figure 2.2: Comparison beyween the magnetic field dependence of Zeeman energy levels and scattering lengths. (a) Low field behavior of ^{6}Li Zeeman states. A positive slope indicates a low field seeker state, whereas a negative one indicates an high field seeker. The three lowest sublevels have different character for low (¡ 50 G) magnetic fields. For fields higher than 100 G they have the same negative slope and they cannot be differentially manipulated with magnetic fields. Figure from [19]. (b) Feshbach resonances of relevant ^{6}Li hyperfine states. The magnetic fields necessary to tune the interaction strength are much higher than those where relevant Zeeman states can be addressed differentially. Data are taken from Ref. [28]

First, spin currents are generated by the free motion of spin states into the trapping potential. This does not allow to have complete control on the spin current itself as the velocity of the atoms is set by the trapping frequency ω_x. While this frequency can indeed be tuned, doing so results in changing the properties of the trapping potential, which in turn affect the properties of the whole atomic sample thus intertwining many different parameters.
Second, this approach is not well-suited for studying spin imbalanced systems. The two spin states can be either completely segregated, thus having two perfectly polarized reservoirs as in [56, 57], or they can be partially separated so that the reservoirs have a certain degree of spin imbalance [61]. The latter case induces a chemical potential difference for the spin states in the two reservoirs and this chemical potential difference drives the spin current. However, while in both cases the two reservoirs are indeed spin imbalanced, the whole system is not. Moreover, investigating transport in a spin imbalanced system with this segregation technique may be rather complicated. In fact, separating the minority and majority components of an imbalanced mixture results in two reservoirs with very different properties. One reservoir will contain many more atoms than the other so that the reservoirs will have either different densities or different spatial extents. Extracting information on spin transport from the relative harmonic motion of such different atomic clouds may indeed be non-ideal.
Moreover, separating the two spin states poses some limitations to the investigation of spin currents in fermionic superfluids. The spin-insulating nature of the superfluid state has indeed been observed as a decrease of spin conductance between terminals [61]. This is due to atoms in different spin states coming from the two reservoirs forming singlet pairs which do not carry any spin current. The inverse phenomena, that is the breaking of pairs due to a spin-dependent

force is instead difficult to observe in the aforementioned experiments.
Therefore, to extend the range of spin transport phenomena that can be investigated in the ultracold atoms framework new tools for the manipulation of the atomic spin degree of freedom need to be developed. The most promising approach to achieve better control on spin manipulation is offered by spin-dependent optical potentials. These potentials allow to use laser light to differentially manipulate atomic states, providing numerous advantages over the traditional magnetic-based spin segregation.
By tuning the laser frequency it is possible to introduce not only opposite forces for the two spin states but also spin-selective effects. A spin-selective optical potential is a potential that is zero for one state and not zero for the other, allowing to manipulate atoms in one spin state without affecting the other:

$$\text{spin-dependent potentials} \begin{cases} V_\downarrow = -V_\uparrow & \text{opposite potentials} \\ V_{\downarrow(\uparrow)} = 0,\ V_{\uparrow(\downarrow)} \neq 0 & \text{spin-selective potential.} \end{cases} \tag{2.9}$$

where $V_{\downarrow(\uparrow)}$ is the optical potential applied to state $|\downarrow(\uparrow)\rangle$. Such spin-dependent optical potentials allow to combine the versatility of atomic manipulation through optical potentials with a differential effect on the two spin states.
One of the greatest advantages of spin-dependent optical potentials is the decoupling between magnetic field and spin manipulation. As we have seen, at the high magnetic fields near a Feshbach resonance, the relevant spin states are both high field seekers. Therefore, it is not possible to induce spin-dependent forces with magnetic field gradients and spin states need to be segregated at low field before ramping up the magnetic field. Instead, using laser light to induce relative motion between the spin states allows to avoid the low field segregating process. This not only simplifies the experimental procedure, but also allows to tune the interaction strength before, after or as the spin currents are developing thanks to the decoupling between magnetic field and spin manipulation.
Moreover, generating a spin current with an optical potential gives access to a much higher degree of control on the properties of the current itself, compared to simply letting the spin states move in the trapping potential. In fact, tuning the intensity or the shape of the laser beam allows to give higher or lower velocities to the atoms, thus controlling the magnitude of the induced current. As we will see in more detail in section 4.4, by giving different shapes to a laser beam it is also possible to imprint currents in systems with many different geometries. These atomic currents can mimic charge currents in solid state materials and the quantum simulation of electronic circuits with atomic circuits has led to the emergence of the field of *atomtronics* [7], which is one of the most active research areas in the quantum gases community. Imprinting an atomic current with a spin-dependent potential allows to give opposite velocities to atoms in different spin states, whereas a spin-selective potential imprints a velocity to only one of two spin states. In both cases the resulting current is indeed a spin current, as the spin degree of freedom is transported by the moving atoms. Using spin-dependent optical potentials it is therefore possible to extend the field atomtronics to the quantum simulation of spintronics devices.
Combining optical potentials with high resolution optical elements, allows to realize local spin-dependent perturbations that address only some areas of the atomic sample, opening up the possibility of introducing spin-dependent elements such as barriers or obstacles. Further, a local spin-dependent laser beam can be used to introduce a local spin-imbalance in the atomic sample, that is a spin or magnetic impurity. This can be achieved by removing one spin component from

the trap with a resonant light pulse. However, the same local polarization can be achieved by a spin-dependent Gaussian potential that attracts atoms in one state and repels atoms in the other as proposed in [63]. The resulting spin impurity is a spin polarized droplet usually referred to as a *ferron* [63, 64]. Spin-dependent optical potentials allow to introduce and investigate such impurities in ultracold Fermi gases at all interaction regimes. In particular, ferrons are expected to arise even in the superfluid regime, where atomic pairs can be broken by the spin-dependent optical potential. It is however necessary to take into account that the energy required to break a pair may indeed be sufficient to ultimately destroy superfluidity itself and that, due to the near-resonant light usually employed to realize spin-dependent potentials, the heating effect of the laser beam may result in unacceptable levels of thermal excitations [63].

A sufficiently strong spin-dependent perturbation may indeed affect the spin transport properties of a fermionic superfluid or, more generally, of a paired system. As we have seen, a paired system has vanishing spin susceptibility, thus being a spin insulator. However, an optical potential that has an opposite sign for the particles composing the pairs may indeed break them, leading to an increase of spin conductivity. The pairs broken in this way may in principle differ from those broken by thermal excitations, and spin-dependent optical potentials may open up the possibility of realizing a Cooper pair splitter [65, 66]. In this way it may be possible to quantum simulate the crossed Andreev reflection process, that is the reverse process of the formation of a Cooper pair.

The energy required to break a fermionic pair does indeed depend on the nature of the pair itself, being the lowest in the BCS side and increasing towards the molecular BEC regime. A spin-dependent optical potential may provide an alternative way to more traditional RF spectroscopy [4] to probe the pairing energy across different interaction regimes. A spin-selective potential, instead, can be used to test the spin-insulating nature of the superfluid by imprinting a velocity to only one spin state and observing the unaddressed state follow as a consequence of pairing. As the presence of fermionic pairs results in a spin insulating character, the investigation of the spin transport properties of a Fermi gas in the pseudogap regime may help shed light on the actual presence of preformed, non superfluid, pairs. Combining measurements of pair binding energy with measurements of spin conductivity may help investigate the spin transport properties of a fermionic spin mixture as a function of both temperature and interaction strength [67].

Other than offering advantages over typical spin transport experiments, optical potentials allow to investigate spin drag phenomena with unprecedented control over length and timescales. As we have seen, a spin current in a strongly interacting system is damped by collisions between atoms in opposite spin states, leading to the phenomenon of collisional spin drag. This effect may add to pairing in giving a velocity to the unaddressed spin component, thus complicating the interpretation of experimental data. However, while collisional spin drag is a dissipative process, pairing should transform a spin current into an unpolarized current without significant dissipation so that it should be possible to discriminate between the two phenomena. Moreover, collisional spin drag is expected to take place over relatively long timescales, thus investigating the dragging effect at short timescales (*fast spin drag* [68]) allows to exclude this dissipative effect. We report intuitive sketches of the described phenomena concerning spin transport in different regimes in Fig. 2.3.

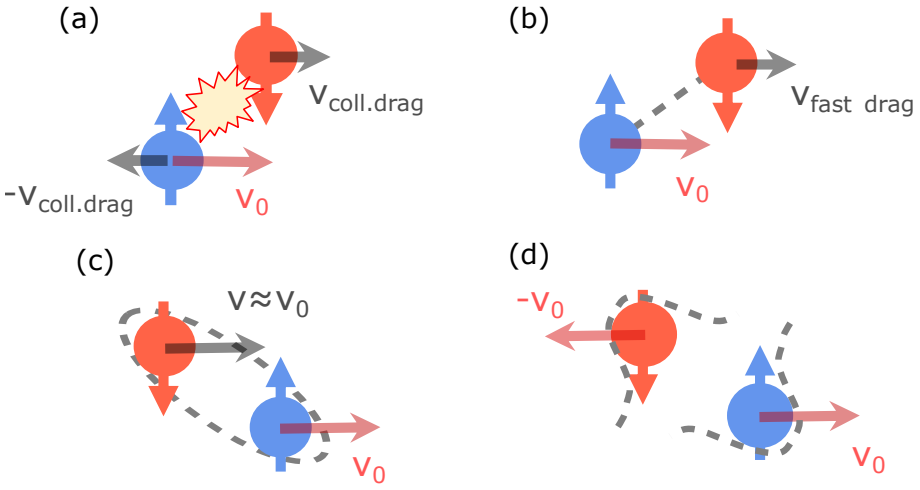

Figure 2.3: Spin transport in a two-components Fermi mixture. (a) Collisional spin drag. Imprinting a velocity v_0 to one state with a spin-selective potential leads to collisions with the other component. This results in transferring the velocity $v_{coll.drag}$ to the unaddressed spin state and in a damping of the spin current. (b) Fast spin drag in an unpaired systems. On short timescales the drag phenomenon is non dissipative and it is driven by correlations between the two spin states. (c) Spin drag in a paired system. Since a paired system is a spin insulator, giving a velocity to one spin state results in the other following with comparable speed. (d) Pair breaking due to spin-dependent perturbations. By pulling atoms in opposite directions with a sufficiently strong spin-dependent optical potential it should be possible to break a fermionic pair and restore spin conductivity.

2.3.1 Short timescales accessibility: fast spin drag and AC spin currents

Compared to experiments based on spin transport between reservoirs, spin-dependent optical potentials allow to access a wider range of timescales. Thanks to the fast timing properties of the tools used to manipulate laser light, the most diffused being Acousto Optic Modulators (AOMs), the time dependence of the spin-dependent perturbations produced through optical potential can be controlled with microseconds resolution. It is therefore possible to produce laser pulses and shine the spin-dependent optical potentials on the atomic cloud for very short times in order to investigate the short time response of the system. Further, by tuning and shaping the light intensity it is possible to realize time-dependent optical potentials and generate periodic AC spin currents which have yet to be observed in ultracold atomic systems [69].
As we have seen, putting in motion one spin state with a spin-selective potential affects the other state that is thus put into motion as well. Such spin drag effect can have a dissipative nature and arise from collisions between atoms in the two spin states (Fig. 2.3 (a)). This is the origin of spin diffusion and the collisional spin drag coefficient as been measured in both weakly and strongly interacting Fermi gases [56, 57]. However, this collisional effect is expected to develop on a timescale that is comparable to the low energy excitations of the system, corresponding to the frequencies of the trapping potential. While spin currents induced by separating spin components are inevitably developed on the typical timescales of the trapping potential, the employment of spin-dependent optical potentials allows to induce spin currents on much shorter

timescales. This gives access to a short time regime where a different spin drag effect is expected to develop, namely fast spin drag [68].
Fast spin drag is a collisionless and non dissipative effect driven by correlations between atoms in different spin states. Such correlations may arise from current-dependent interactions, where the momentum of one state has an effect on the momentum of the other. This is the case of the Andreev-Bashkin effect, which is a beyond mean-field phenomenon taking place in mixtures of interacting superfluids [68]. A similar effect is also expected to arise in normal Fermi systems described by Landau's Fermi liquid theory. The dynamic properties of such systems can be described by the Landau parameters F_1 and G_1, accounting for the in-phase and out-of-phase interaction effects respectively. In a weakly interacting Fermi gas these parameters can be computed with perturbation theory [68], while they cannot be theoretically determined for strongly interacting systems where the Fermi liquid theory is expected to fail. If we induce a velocity $v_\uparrow$ to state $|\uparrow\rangle$, as can be done a with spin-selective optical potential, the velocity $v_\downarrow$ acquired by state $|\downarrow\rangle$ is predicted by perturbation theory to be [68]:

$$\begin{aligned} v_\downarrow &= \frac{\langle n_{drag}/n\rangle}{\langle 1/2 - n_{drag}/n\rangle}\, v_\uparrow \\ n_{drag} &= \frac{F_1 - G_1}{3 + F_1}\frac{n}{4} \end{aligned} \tag{2.10}$$

where n is the atomic density. For a weakly interacting 3D system ($k_f a = -0.5$) the predicted effect is rather small as the ratio $v_\downarrow/v_\uparrow$ is of the order of 4%. However, the effect is expected to increase in lower dimensions and in presence of stronger interactions. Also, investigating deviations from the predicted behavior at higher interaction strengths may help shed light on the applicability of Fermi liquid theory to strongly interacting systems. Further, fast spin drag measurements can be used to probe the effective mass of polaronic quasiparticles in spin imbalanced systems. These are particular fermionic quasiparticles where atoms in a minority component get dressed by interactions with the majority atoms so that the resulting impurity is a so-called *polaron* quasiparticle [70, 71]. Inducing a velocity to the majority atoms in $|\uparrow\rangle$ results in the polaron being dragged with velocity [68]:

$$v_\downarrow = \frac{\langle 1 - m_\downarrow/m^*_\downarrow\rangle}{\langle m_\uparrow/m^*_\uparrow\rangle}\, v_\uparrow \simeq \left\langle 1 - \frac{m_\downarrow}{m^*_\downarrow}\right\rangle v_\uparrow \tag{2.11}$$

where $m_{\uparrow,\downarrow}$ and $m^*_{\uparrow,\downarrow}$ are the mass and the effective mass of the particles in the two spin states. Therefore, the polaron effective mass $m^*_\downarrow$ can be measured by investigating its short time response to a spin-selective perturbation to the majority component.
Beside fast spin drag, the rapid manipulation of laser light allows to introduce time and spin-dependent optical potentials which can be used to investigate frequency-resolved spin transport, as proposed in [69]. This will give access to the AC optical spin conductivity σ^S defined as:

$$\langle \tilde{J}_{S,\alpha}(\omega)\rangle = \sigma^S_{\alpha,\beta}(\omega)\tilde{f}_\beta(\omega) \tag{2.12}$$

where α and β denote Cartesian components while $\tilde{J}_{S,\alpha}(\omega)$ and $\tilde{f}_\beta(\omega)$ are the Fourier transforms of the spin current $J_{S,\alpha}(t)$ and the time-dependent perturbation $f_\beta(t)$ respectively [69]. The AC spin conductivity is expected to depend non trivially on ω and to have a different behavior in different interaction regimes as the excitation spectra may or may not be gapped due to the presence of fermionic pairing.

2.3.2 Coupling heat and spin transport

Finally, spin-dependent optical potentials may be used to quantum simulate the two fundamental spin caloritronics processes, namely the spin-dependent Seebeck and Peltier effects. The question on whether it is possible to quantum simulate spin caloritronics phenomena with ultracold atoms has been addressed in the case of both Bose and Fermi gases [48–50] and the answer seems to be affirmative.
Looking at Eq. 2.4, we see that to introduce a spin current $\mathbf{J}_s$ and a spin-heat current $\mathbf{Q}_s$ it is necessary to have a spin-dependent force $\mathbf{F}_s$ and a spin-temperature gradient ∇T_s. Both these elements can be realized with spin-dependent optical potentials. By using these potentials to induce a spin current in an atomic sample it should be possible to investigate the spin-dependent Peltier effect, that is the generation of a spin-heat current. This spin-heat current could be detected by looking at differences between heat currents carried by the two spin states. On the other hand, to investigate the spin-dependent Seebeck effect it is necessary to induce a gradient in the spin-temperature and look for the generation of a spin current. As we already mentioned, the observation of spin currents in ultracold atomic gases is easily achieved by looking at the relative position of the centers of mass of the two spin states. The generation of a spin-temperature gradient, instead, may prove rather complicated. Nonetheless it should be possible to realize it with a spin-selective optical potential that can be employed to heat one side of the atomic cloud in a spin-selective way. Heating only part of the atomic cloud, or shaping the intensity profile of the laser beam, allows to achieve a temperature gradient, while the spin-selectivity of the heating process ensures that the temperature of the two spin states is indeed different.
Many questions remain open on the feasibility of such spin caloritronics measurements as the detection of the spin-heat current generated in the spin-dependent Peltier effect can indeed be non trivial. Further, the sustainability of a temperature difference between the two spin states cannot be taken for granted due to thermalization processes. In fact, as the externally applied spin-dependent heating is turned off, the spin-dependent temperature will ultimately equilibrate due to interspin scattering. A possible way of stabilizing the spin-temperature may be to use a Feshbach resonance to tune the p-wave scattering length so that intraspin scattering, which is forbidden in the case of s-wave interactions, is much more favoured then interspin scattering [48]. This may help in preventing thermalization between the two spin components but requires an usual tuning of the p-wave scattering length which could lead to other experimental issues. To quantify the stability of a spin-temperature it is possible to compute the spin-heat relaxation time and length, that are the typical time and length scales over which the spin-temperature accumulation is lost. Computing such quantities for different temperatures and interaction strengths seems to confirm the stability of the spin-temperature accumulation for ultracold atomic gases due to a divergence of the relaxation parameters at degenerate temperatures [48, 50]. Further, depending on the interspin scattering lengths, the spin-heat relaxation length in fermionic systems can be of the order millimeters, which is well within experimental resolution being actually larger than the typical sample size. These theoretical predictions seem to confirm that the realization of spin caloritronics with ultracold Fermi gases is indeed feasible and that spin-dependent optical potentials could be the most suited tools for the task.

Chapter 3

Realization of tailored spin-dependent optical potentials

In this chapter we present the physical origin of spin-dependent optical potentials and the setup we have realized for their implementation on the main experimental apparatus. First we show how spin-dependent and spin-selective optical potentials arise from the polarizabilities of the hyperfine ^{6}Li Zeeman levels and how we have to go beyond the two-level approximation for accurately computing such polarizabilities. Further, we show how we realize such potentials by tuning the frequency of a laser source between the ^{6}Li D-lines and by controlling the light polarization. Since the laser frequency is a fundamental parameter for the realization of spin-dependent optical potentials, we describe the offset-lock setup we implemented for tuning and stabilizing the frequency of our laser source. In the last part of this chapter we present the experimental setup we designed and built for tailoring the spin-dependent optical potentials using a Digital Micromirror Device and for shining them on our atomic cloud, taking advantage of the horizontal imaging optical path.

3.1 Origin of spin-dependent optical potentials

As we have seen in Chapter 1, a two-level atom exposed to non-resonant light feels an optical potential whose sign and magnitude are related to the intensity of the light and to the detuning between the light frequency and the considered atomic transition. In the light shifts picture [16, 21], this potential can be interpreted as a dressing of the atomic levels by the electromagnetic field. This dressing shifts the energy of the levels so that the atoms see an energy landscape that depends on the presence and on the intensity of the external field, as if under the action of an external potential. For a given light frequency, different internal states get different light shifts, so that the optical potential acting on an atom depends by the atom's internal state. Therefore, in principle, every light frequency has a differential effects on atoms in different states.
In many cases, these differential effects can either be neglected or they can be a troublesome feature which needs to be coped with. However, exploiting this effect for purposely engineering state-dependent optical potentials opens up the possibility of using laser light for differentially manipulating atoms in different internal states. In our experiment we work with atoms in two of the three lowest ^{6}Li hyperfine Zeeman sublevels ($|1\rangle, |2\rangle, |3\rangle$) which have an energy spacing

of the order of 80 MHz. For trapping and manipulating these states in our experiments we usually use far-detuned laser light (infrared or green) so that the whole ^{6}Li internal structure is not resolved and can be completely neglected. In particular, we can neglect the fine splitting of the D-line and consider lithium as a two-level atom with just one available transition from the 2S ground state to the 2P excited state. Since the state-dependent effect arises due to the laser light having different detunings from the transitions available from each state and since we work with $\simeq 10^8$ MHz detunings compared to an energy difference of $\simeq 80$ MHz between the internal states, the differential light shift between such state can be completely negligible. There are, however, situations in which these effects are not negligible and can actually be a troublesome experimental issue. Usually this happens in experiments working with mixtures of atoms in very different states, such as mixtures of different atomic species or of atoms in the ground and in metastable excited states. In such cases, the energy difference between the states composing the system can be much more significant than our 80 MHz splitting and state dependent light shifts are actually the norm. This can be a problem when it is necessary to act on the different components in the same way for cooling and trapping them together. However, this difficulty can be overcome by exploiting so-called *magic wavelengths*, that are particular wavelengths that allow to have the same light shifts for different atomic states. On the other hand, once the system is sufficiently cold and trapped in the desired potential, manipulating the components in a differential way opens up many interesting possibilities such as addressing one component without affecting the other. The wavelengths resulting in light shifts that affect one atomic state significantly more than another are usually called *tune-out* wavelengths and are a very promising tool for selectively trapping or manipulating components in a two-components mixture. State-selective optical potentials result from ideal tune-out wavelengths where the light shift of one state is zero while that of the other is not, thus resulting in an optical potential that addresses only one of the two components. As already mentioned, these special wavelengths are usually exploited in experiments working with systems where the components have very different transition energies and the light needed to realize such selective potentials is usually quite off-resonance ($\simeq$ nm) for all the components involved.
Conversely, the components of our ^{6}Li system are atoms in different hyperfine levels and the energy difference between transitions to the excited state starting from one level or the other are indeed small, thus suppressing the effect of differential light shifts for nearly all wavelengths. However, we will show that there are particular configurations of light frequency and polarization that lead to the emergence of state-dependent optical potentials even for our ^{6}Li hyperfine states. In particular, we will show that to resolve the atomic internal structure and thus realize state-dependent effects it is necessary to use near-detuned laser light.

3.1.1 Multi-level light shifts of ^{6}Li Zeeman states

Since our system is composed by atoms in different hyperfine spin states, their energy difference is indeed small and to induce differential light shifts on them we need to work with near-detuned laser light. In this particular condition, the two-level approximation breaks down and we have to compute the multi-level light shifts of our hyperfine states considering all the relevant atomic transitions. While this is indeed more complicated than considering only two atomic levels, it is the presence of more than one available excited state that gives rise to the strong state-dependency of our optical potentials.

Starting from Eq. 1.12 and relaxing both the two-level and the rotating wave approximation we can find the most general expression for the AC Stark shift of a level $|g\rangle$ [16]:

$$\Delta E_g(\omega, \mathbf{r}) = -\sum_e \frac{2\omega_{eg}|\langle g|\hat{\epsilon}\cdot\mathbf{d}|e\rangle|^2}{4\hbar\left(\omega_{eg}^2-\omega^2\right)}|E_0(\mathbf{r})|^2 \tag{3.1}$$

where the summation is over all possible excited states $|e\rangle$, ω_{eg} is the transition frequency between $|g\rangle$ and $|e\rangle$, $\mathbf{d}$ is the dipole operator while E_0 and ω are the field amplitude and frequency respectively. To eliminate the linear dependency of the light shift on the squared laser amplitude we can introduce the state's complex polarizability $\alpha_g(\omega)$, whose real part determines the light shift.

$$\begin{aligned}\Delta E_g(\omega, \mathbf{r}) &= Re\left[\alpha_g(\omega)\right]|E_0(\mathbf{r})|^2 \\ Re\left[\alpha_g(\omega)\right] &= -\sum_e \frac{2\omega_{eg}|\langle g|\hat{\epsilon}\cdot\mathbf{d}|e\rangle|^2}{4\hbar\left(\omega_{eg}^2-\omega^2\right)}.\end{aligned} \tag{3.2}$$

Therefore, for computing the polarizabilities of our hyperfine states we need to know the energy of all the possible excited states and dipole matrix elements $\langle g|\hat{\epsilon}\cdot\mathbf{d}|j\rangle$ associated to each transition. Our light source for realizing the spin-dependent potentials is a 671 nm laser, which is near-detuned with respect to both the D_1 and D_2 lines but it is far-detuned from the next transition (the UV 2S-3P transition at 323 nm) so that we can neglect this last transition and consider only the available states in the $2P_{1/2}$ and $2P_{3/2}$ manifolds.
Since all our experiments heavily rely on the ^{6}Li Feshbach resonances, both our ground state and all the available excited states are strongly affected by the external Feshbach fields which are typically in the range $300-1000$ G. Therefore, the fine structure energy levels of our atoms are shifted by an Hamiltonian that includes both the hyperfine coupling and the interaction with the external magnetic field:

$$H = \frac{\mu_B}{\hbar}(g_J\hat{\mathbf{J}}\cdot\mathbf{B} + g_I\hat{\mathbf{I}}\cdot\mathbf{B}) + \frac{a_{hf}}{\hbar^2}\hat{\mathbf{J}}\cdot\hat{\mathbf{I}} \tag{3.3}$$

where g_J and g_I are the electronic and nuclear gyromagnetic factors, and a_{hf} is the hyperfine coupling energy. While $g_I = -0.0004476540$ [19] is not affected by the atomic state, g_J and a_{hf} depend on the electron orbital momentum L and total angular momentum J which characterize each level manifold. We report the values of g_J and a_{hf} for the relevant states in Table 3.1 [19]. Both the excited states have a very small hyperfine energy splitting so that we can completely

	2S	$2P_{1/2}$	$2P_{3/2}$
g_J	2.0023010	0.6668	1.335
a_{hf}	152.1368407 MHz	17.386 MHz	-1.155 MHz

Table 3.1: Values of the electronic gyromagnetic factor g_J and hyperfine coupling energy a_{hf} for the experimentally relevant states of ^{6}Li. Values are taken from Ref. [19].

neglect their hyperfine structure for all significant magnetic fields. Further, being the nuclear gyromagnetic factor much smaller than the electronic one we can neglect also the nucleus-magnetic field interaction term of Hamiltonian 3.3. Therefore, the eigenvalues that give the energy of the states in the $2P_{1/2}$ and $2P_{3/2}$ manifolds at high fields can be approximated by:

$$\Delta E_Z \simeq \frac{\mu_B}{\hbar} g_J m_J B \tag{3.4}$$

where m_J is the projection of the total angular momentum along the quantization axis. From this expression it is evident that the external magnetic field lifts the m_J degeneracy of the $2P_{1/2}$ and $2P_{3/2}$ states that are thus splitted into two and four levels respectively. We report the Zeeman shifts of the $2P_{1/2}$ and $2P_{3/2}$ manifolds in Fig. 3.1 (a)-(b).
Due to a stronger hyperfine coupling, the diagonalization of the Hamiltonian for the 2S ground state is more complicated and it is usually done numerically. We report its eigenvalues as a function of the external field in Fig. 3.1 (c). These values are computed with a Wolfram Mathematica code available in Ref. [19]. While it is customary to solve the hyperfine Hamiltonian

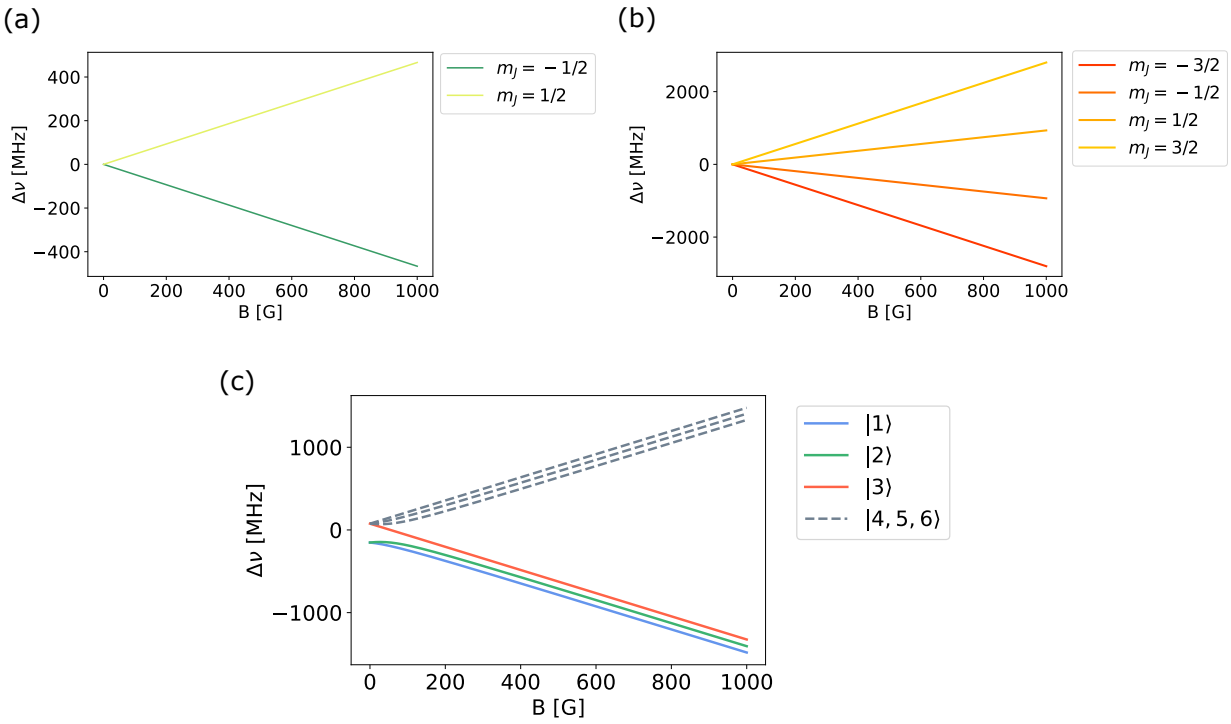

Figure 3.1: Zeeman states of ^{6}Li in strong magnetic fields. (a) Zeeman shift of the $2P_{1/2}$ manifold. The zero-field state is split in two Zeeman subleves labeled by their m_J quantum number. (b) Zeeman shift of the $2P_{3/2}$ manifold. (c) Zeeman levels of the ground state manifold. Here the stronger hyperfine coupling causes a non negligible shift between states with the same m_J. This results in a splitting into six levels labeled in order of increasing energy. The experimentally relevant states are the three with the lowest energy, namely $|1\rangle, |2\rangle$ and $|3\rangle$. Data in (a) and (b) are computed analytically, data in (c) are obtained from a numerical diagonalization of the Hamiltonian with a Wolfram Mathematica code available in Ref. [19].

numerically, when either $J = 1/2$ or $I = 1/2$ the eigenvalues have an analytical expression given by the *Breit-Rabi* formula [16]. Since the ground state of ^{6}Li has $J = 1/2$, the Hamiltonian can be analytically diagonalized and its eigenstates can be expressed as linear combinations of $|J = 1/2, m_J, m_I\rangle$ states [19, 72, 73]. The resulting eigenstates are six energy levels which we label $|1, 2, 3, 4, 5, 6\rangle$ in increasing energy order. From an experimental point of view we can

consider only the three lowest energy states which we can write in the $|m_J, m_I\rangle$ basis as:

$$\begin{aligned} |1\rangle &= \sin\theta_+|1/2,0\rangle - \cos\theta_+|-1/2,1\rangle \\ |2\rangle &= \sin\theta_-|1/2,-1\rangle - \cos\theta_-|-1/2,0\rangle \\ |3\rangle &= |-1/2,-1\rangle \end{aligned} \tag{3.5}$$

where:

$$\begin{aligned} \sin\theta_\pm &= 1/\sqrt{1+(Z^\pm+R^\pm)^2/2} \\ R^\pm &= \sqrt{(Z^\pm)^2+2} \\ Z^\pm &= \frac{g_I+g_J}{a_{hf}}\mu_B B \pm 1/2 \\ \cos\theta_\pm &= \sqrt{1-\sin^2\theta_\pm}. \end{aligned} \tag{3.6}$$

With the exception of $|3\rangle$, which is a pure $|m_J = 1/2\rangle$ state, all these levels are expressed as linear combinations of states with different quantum numbers. For all significant magnetic fields the energy spacing between these Zeeman levels is around 80 MHz so that the difference between $|1\rangle$ and $|3\rangle$ is 160 MHz. Knowing the zero field energies of the D_1 and D_2 transitions and having computed the Zeeman and hyperfine shifts of the involved levels we can easily determine all the transition frequencies ω_{ge} in the summation of Eq. 3.2.
To compute the multi-level polarizability of each state we also need to determine the dipole matrix elements $\langle g|\hat{\epsilon}\cdot\mathbf{d}|e\rangle$ between each ground state and each excited state. Since all our levels can be labeled as $|J, m_J\rangle$, we can use the Wigner-Eckart theorem to write [16] :

$$\begin{aligned} \langle J, m_J|\hat{\epsilon}\cdot\mathbf{d}|J', m'_J\rangle &= \langle J||\hat{\epsilon}\cdot\mathbf{d}||J'\rangle\langle J, m_J|J', m'_J; 1, q\rangle \\ &= \langle J||\hat{\epsilon}\cdot\mathbf{d}||J'\rangle(-1)^{J'-J+m'_J-m_J}\sqrt{\frac{2J+1}{2J'+1}}\langle J', m'_J|J, m_J; 1, -q\rangle \end{aligned} \tag{3.7}$$

where $\langle J||\hat{\epsilon}\cdot\mathbf{d}||J'\rangle$ is the reduced matrix element of the $|J\rangle \to |J'\rangle$ transition, $\langle J', m'_J|J, m_J; 1, -q\rangle$ is a Clebsch-Gordan coefficient and $q = 0, \pm 1$ for π or $\sigma^\pm$ polarized light respectively. Decomposing the matrix element in this way allows to decouple the radial dependence, taken over by the reduced matrix element, and the orientation dependence of the dipole matrix element, which appears as a Clebsch-Gordan coefficient. We can express these coefficients through the Wigner 3-j symbols as [16]:

$$\langle J', m'_J|J, m_J; 1, -q\rangle = (-1)^{J-1+m'_J}\sqrt{2J'+1}\begin{pmatrix} 1 & J' & J \\ q & m'_J & -m_J \end{pmatrix} \tag{3.8}$$

where the term in parenthesis is the Wigner3-j symbol.
Since all the considered excited states belong to either the $2P_{1/2}$ or $2P_{3/2}$ manifolds, there are only two possible values for the reduced matrix element $\langle J||\hat{\epsilon}\cdot\mathbf{d}||J'\rangle$. These can be calculated by explicitly overlapping the radial part of the atomic wavefunctions, however a much easier way to obtain them is through the spontaneous decay rate from the $|J'\rangle$ to the $|J\rangle$ level, which are known to good precision:

$$\Gamma_{J',J} = \frac{\omega_0^3}{3\pi\epsilon_0\hbar c^3}\frac{2J+1}{2J'+1}|\langle J||\hat{\epsilon}\cdot\mathbf{d}||J'\rangle|^2. \tag{3.9}$$

Combining the previous expressions and computing the reduced dipole matrix elements from the linedwith of the D_1 and D_2 transitions ($\Gamma_{D_1} = \Gamma_{D_2} = 2\pi\, 5.8724$ MHz) allows to obtain the final expression for our dipole matrix elements [74]:

$$\langle J, m_J|\hat{\epsilon}\cdot\mathbf{d}|J', m'_J\rangle = (-1)^{J'-1-m_J}\sqrt{2J+1}\begin{pmatrix}1 & J' & J\\ q & m'_J & -m_J\end{pmatrix}\langle J||\hat{\epsilon}\cdot\mathbf{d}|J'\rangle \tag{3.10}$$

Knowing the energy and the matrix elements of all possible transitions we can compute the multi-level polarizability of each ^{6}Li Zeeman state for all magnetic fields and for all possible light polarization.

3.1.2 Spin-dependent and spin-selective optical potentials

We compute the real part of the polarizability $\alpha(\omega)$ of the $|1\rangle$, $|2\rangle$ and $|3\rangle$ states using expression 3.2. We report a comparison between such polarizabilities for the relevant state mixtures ($|1\rangle - |2\rangle$, $|1\rangle - |3\rangle$) in Fig. 3.2, computing them for different light polarization at fixed magnetic field (572 G). The atomic polarizabilities present resonances at the frequencies corresponding to the D-lines of lithium, appropriately shifted by the hyperfine coupling and Zeeman shift. Furthermore, the $|1\rangle$ and $|2\rangle$ polarizabilities display other resonant frequencies at wavelengths slightly smaller than the D_2 line, corresponding to additional transitions to excited states that are accessible thanks to their $|m_J = 1/2\rangle$ component. On the other hand, $|3\rangle$ is a pure $|m_J = -1/2\rangle$ state and it does not have any available transition at such frequencies, resulting in a much lower polarizability. This frequencies, which are resonant for $|1\rangle$ and $|2\rangle$ but not for $|3\rangle$, could in principle be used in a $|1\rangle - |3\rangle$ mixture to generate strongly spin-dependent perturbations, as proposed in Ref. [73].
Another frequency range displaying strongly spin-dependent polarizabilities correspond to the region between the D_2 transitions of the two spin states. For such frequencies, the light will be red-detuned for the state with the highest transition energy (state $|1\rangle$) and blue detuned for the other state (either $|2\rangle$ or $|3\rangle$), resulting in light shifts with opposite sign for the two spin-states. By finely tuning the laser frequency in this region we can find a so-called *anti-magic* wavelength, that is a wavelength for which the two states have a equal and opposite polarizabilities (see Fig. 3.4 (a)).
A particularly appealing region is that corresponding to frequencies between the D_1 and D_2 lines. Here, the contributions of the two transitions add up resulting in zero-crossings of the multi-level polarizability. In fact, light with frequency ν, where $\nu_{D_1} < \nu < \nu_{D_2}$, is blue-detuned with respect to the D_1 transition and red-detuned with respect to the D_2. Therefore the two atomic transitions yield oppositely-signed light-shifts which, for a particular value of ν, have also the same magnitude. When this happens the light shifts related to the two transitions cancel out yielding a zero crossing of the polarizability, which can be exploited to realize a spin-selective optical potential (see Fig. 3.4 (b)).

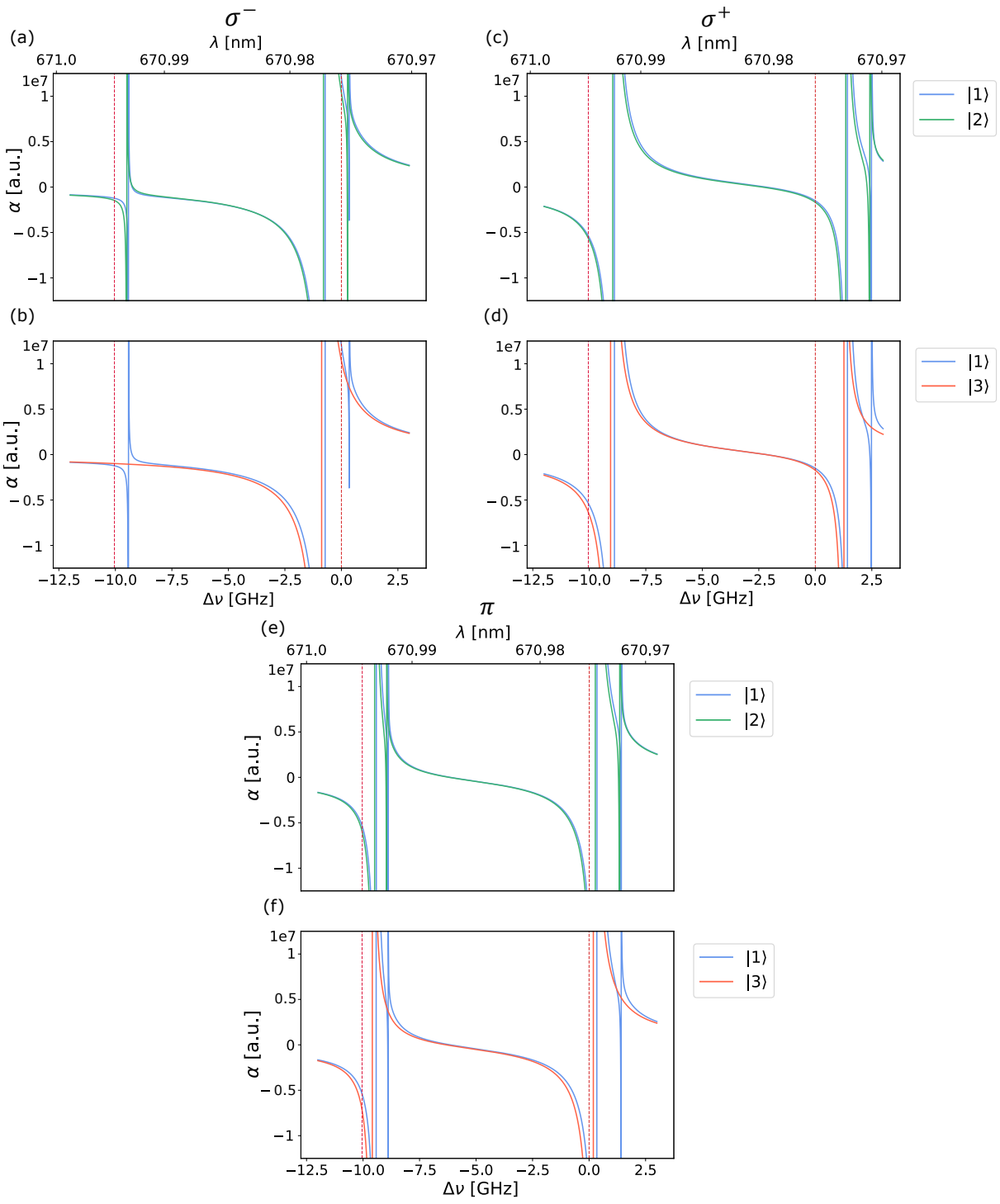

Figure 3.2: Polarizabilities of the three lowest Zeeman states of ^{6}Li at 572 G for different light polarization. Polarizabilities are computed using Eq. 3.2 and are plotted as a function of the detuning $\Delta\nu$ from the zero field D_2 transition (lower x-axis) and of the light wavelength (upper x-axis). We report the D_1 and D_2 wavelengths as dashed red lines. (a) and (b) are the polarizabilities of states $|1\rangle - |2\rangle$ and $|1\rangle - |3\rangle$ for σ^- polarized light. (c) and (d) are the polarizabilities of states $|1\rangle - |2\rangle$ and $|1\rangle - |3\rangle$ for π polarized light. (a) and (b) are the polarizabilities of states $|1\rangle - |2\rangle$ and $|1\rangle - |3\rangle$ for σ^+ polarized light. Polarizabilities are reported in atomic units, where 1 a.u. $= 1.64877727436\times10^{-41}\,\frac{C^2m^2}{J^2}$.

When deciding which are the most suited frequencies for generating spin-dependent optical potentials we need to also take into account the probability of photon absorption. As mentioned in Chapter 1, each time a photon is absorbed and spontaneously re-emitted the atom recoils in a random direction, resulting in an heating of the sample or in losses due to atoms escaping the optical confinement whenever their temperature reaches a sufficient fraction of the trap depth. To quantify the scattering rate of photons by our atoms we can, analogously to what we did for the light shifts, generalize expression 1.7 to the case of many excited levels:

$$\Gamma_{sc,i}(\omega, \mathbf{r}) = \sum_j \frac{\Omega_{ji}^2(\mathbf{r})/\Gamma}{1 + 2\Omega_{ji}^2(\mathbf{r})/\Gamma^2 + 4\delta^2/\Gamma^2} \tag{3.11}$$

where $\Omega_{ji}(\mathbf{r}) = \frac{\langle i|\hat{\epsilon}\cdot\mathbf{d}|j\rangle E_0(\mathbf{r})}{\hbar}$ is the Rabi frequency for the $|i\rangle \rightarrow |j\rangle$ transition and $\Gamma = 2\pi\, 5.8724$ MHz is the linewidth of both the D_1 and D_2 transitions. We report the computed scattering rates for our Zeeman levels at 572 G and I = 0.1 ,W/cm^2 for different light polarization in Fig. 3.3. The resonances corresponding to the transitions from the $|m_J = 1/2\rangle$ components of states $|1\rangle$ and $|2\rangle$ are clearly visible as peaks in the scattering rates on the right shoulder of the D_2 resonance. Therefore, while those frequencies provide strongly spin-dependent polarizabilities, they are not ideal for the generation of spin-dependet optical potentials as they lead to high photon absorption and strong heating of the sample. Nonetheless, such frequencies can indeed be exploited for producing spin-selective dissipative perturbations in a $|1\rangle - |3\rangle$ mixture by strongly heating the spin component in state $|1\rangle$ while having only a mild effect on atoms in $|3\rangle$. Unfortunately, this selective heating cannot be applied to $|1\rangle - |2\rangle$ mixtures since both these states present resonances related to the mixing of $|m_J = 1/2\rangle$ components.

The requirement of engineering non-dissipative perturbations also prevents us from exploiting the high spin-dependency of the polarizability for frequencies between the D_2 transitions of the two spin states. In fact, these near-resonant frequencies come, again, with the downside of strong dissipation due to high photon absorption. Therefore, while having large and strongly state-dependent polarizabilities, these frequencies are not suited for the implementation of spin-dependent optical potentials.

Instead, the most appealing frequencies for the realization of such potentials are those between the D_1 and D_2 lines, as these are the frequencies giving spin-dependent polarizabilities which are the farthest from the atomic resonances. In Fig. 3.4 we report a comparison between the polarizabilities and scattering rates for near-resonant light (i.e. light that is almost resonant with the D_2 transition) and for light with frequency between the D_1 and D_2 atomic lines. As already mentioned, while using near-resonant light results in much larger polarizabilities and light shifts, it comes at the cost of much larger photon absorption. Conversely, finely tuning the light frequency between the two atomic resonances allows to achieve state-dependent polarizabilities with a much smaller scattering rate. While the smaller size of the polarizabilities results in smaller light shifts, their size can be easily increased by increasing the light intensity. This inevitably leads to larger photon absorption as well, however, being a few GHz detuned from the transitions, the scattering rate remains reasonably low even increasing the light intensity. In general, when evaluating the scattering rate for a given light frequency it is not the absolute value of the detuning that is relevant, but rather the ratio between the detuning and the linewidth of the atomic transition Γ. Therefore, whenever we say that a few GHz detuning results in a low scattering rate we are always implicitly comparing this detuning to the 5.8 MHz linewidth of both the D-lines of ^{6}Li. In the previous comparison of the scattering rates for

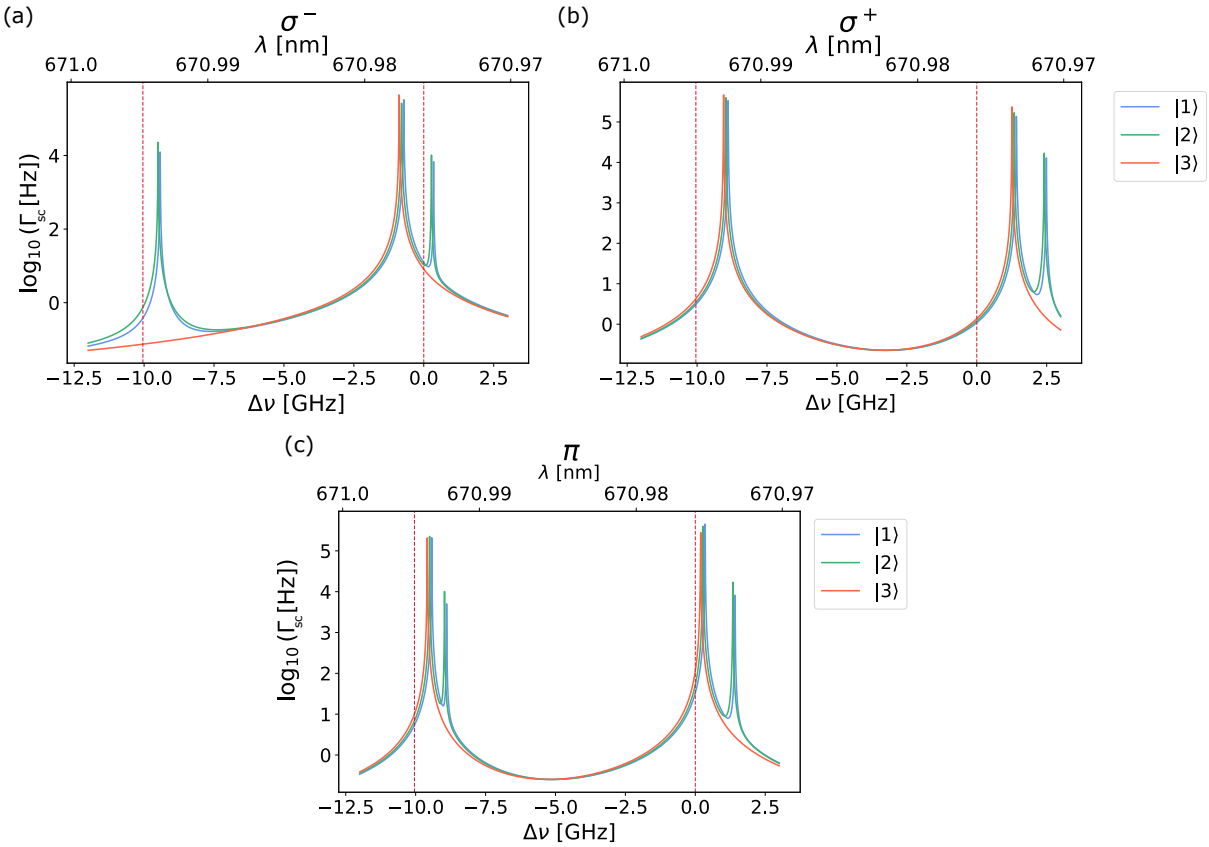

Figure 3.3: Scattering rate of the three lowest Zeeman states of ^{6}Li at 572 G for different light polarization. Scattering rates are computed using Eq. 3.11 and are plotted as a function of the detuning $\Delta\nu$ from the zero field D_2 transition (lower x-axis) and of the light wavelength (upper x-axis). We report the D_1 and D_2 wavelengths as dashed red lines. (a), (b) and (c) are computed for σ^-, π and σ^+ polarization respectively. For all plots the light intensity is $I = 0.1$ mW/cm^2, corresponding to a saturation parameter $s = I/I_s = 0.01$ for the D_1 line and $s = 0.04$ for the D_2. Values for the saturation intensity of the ^{6}Li lines can be found in Ref. [19].

near-resonant light and for a few GHz detuned light we are actually comparing a detuning of $\sim 15\,\Gamma$ to one of $\sim 10^3\,\Gamma$.

Another very appealing perspective of the polarizabilities' spectra for frequencies between the two lines of lithium is the presence of the zero-crossing itself, which opens up the possibility of engineering spin-selective optical potentials. Setting the wavelength of our laser source to the value where the polarizability of one state is zero (tune-out wavelength) allows to produce a state-selective optical potential that affects only the state that has a non-zero polarizability. Such selective potential is an ideal tool for manipulating the spin degree of freedom in our sample in a controlled way since it allows to address only one spin component in our mixture. Moreover, by tuning the light wavelength between the zero crossings of the two states it is possible to find an anti-magic wavelength that results in opposite light-shifts for the two spin states, as in the near-resonant case. Therefore, tuning the light frequency in the range between the two zero crossings allows to produce optical potentials that smoothly change from being selective

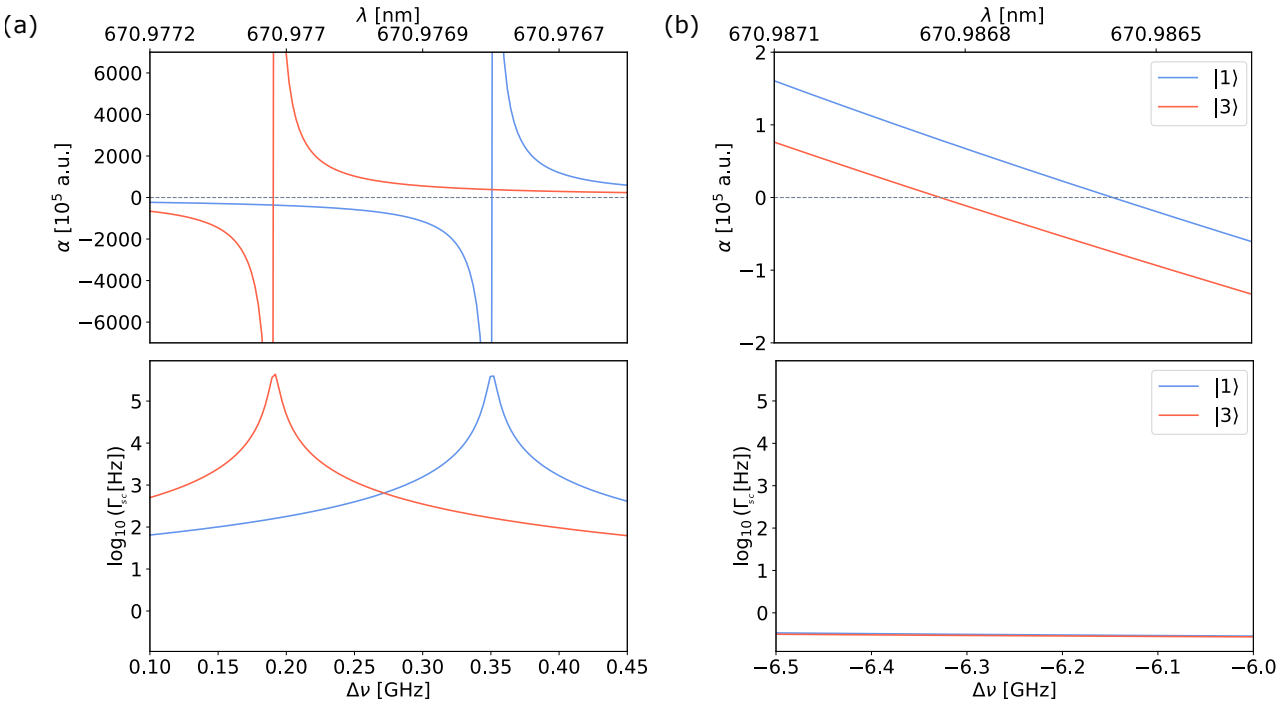

Figure 3.4: State-dependent polarizabilities (top) and scattering rates (bottom) for the $|1\rangle$ and $|3\rangle$ Zeeman states. Data are plotted as a function of the detuning $\Delta\nu$ from the zero field D_2 transition (lower x-axis) and of the light wavelength (upper x-axis). Light that is almost resonant with the D_2 transition results in large state dependent polarizabilities (a, top) at the cost of high scattering rates (a, bottom). Frequencies between the D_1 and D_2 lines are more detuned from the transitions and result in smaller polarizabilities (b, top) and scattering rates (b, bottom) while retaining their state-dependent character. Therefore, these frequencies are more suited for the realization of state-dependent optical potentials. All data are computed for π-polarized light at 572 G. The light intensity for computing the scattering rates is arbitrarily set at $I = 0.1$ mW/cm^2.

for one state to being selective for the other, passing for a wavelength where they are opposite for the two spin states. While in this region the real part of the polarizability clearly depends on the light frequency and on the considered state, the imaginary part, related to the photon absorption probability and scattering rate, is effectively the same for all the spin states and it is nearly independent from the light frequency. This is a desirable feature since it allows to tune the laser frequency to change the character of the optical potential without having any incidence on its dissipative effects.

For all these reasons, we elect this frequency range between the two resonances to be our working region for the generation of spin-dependent optical potential, while we use near-resonant light to engineer spin-selective dissipative perturbations. Such effects are not the main focus of our work, but they are interesting nonetheless and we will show that, beside tailored spin-dependent and spin-selective optical potentials, our experimental setup is capable of producing local spin-selective dissipative perturbations as well.

Discussing the origin of the spin-selective optical potentials we have focused on computing the multi-level polarizabilities at a 572 G fixed magnetic field because this value corresponds to a zero crossing of the $|1\rangle - |3\rangle$ scattering length a_{13} (see Fig. 1.9) and it is the magnetic field we employ for producing the non-interacting Fermi gas over which we test our potentials. However, for investigating more interesting phenomena it is necessary to introduce interactions between the two spin components by changing the external magnetic field. Due to the Zeeman effect, changing the magnetic field affects the energies of the atomic transitions and the frequencies needed to generate the spin-dependent optical potentials. However, assuming a linear relation between the energy shift and the external magnetic field for simplicity, we expect a linear coefficient of less than 1 MHz/G for the shift of the zero crossings in presence of an external field. Therefore, a few hundred Gauss span results in less than 1 GHz shift in the frequency necessary for realizing the spin-dependent potentials. As we will see in the following section, this shift can be easily achieved by our frequency-locking setup, so that we are able to set our light frequency to the desired values for all the relevant magnetic fields.
As a final remark, it is worth to highlight the role of the light polarization in determining the shape and the features of the atomic polarizabilities. When computing the multi-level polarizability of the Zeeman states, the contribution of each transition is weighted by the corresponding dipole matrix element which strongly depends on the light polarization. In particular, to different light polarization correspond different dipole-allowed or prohibited transitions as it is evident in the polarizability of state $|3\rangle$ for σ^--polarized light. For this polarization there is no allowed transition from $|3\rangle$ to any of the excited states of the D_1 manifold (see Figs. 3.2, 3.3).Therefore, these states do not contribute to the polarizability and state $|3\rangle$ does not have any zero crossing in the considered frequency range. This makes working with σ^--polarized light unsuitable for the generation of spin-dependent optical potentials in a $|1\rangle - |3\rangle$ mixture. On the other hand both π and σ^+-polarized light allows to generate spin-dependent and spin-selective potentials for both $|1\rangle - |2\rangle$ and $|1\rangle - |3\rangle$ mixtures, even though the relevant frequencies for the two polarization states are a few GHz different.

3.2 Laser locking

As we have seen in the previous section, a key parameter for realizing spin-dependent optical potentials is the frequency of the laser light used to generate them. Therefore, it is crucial to use a monochromatic laser source and to tune and stabilize its frequency as reliably as possible. For these reasons, we implement an offset-lock setup based on a Phase-Locked Loop (PLL) circuit that allows us to reliably set and lock the frequency of our laser. The PLL circuit reads the frequency difference between our laser source and a locked reference laser. It compares this frequency difference to an externally provided offset signal and acts on our laser to set the detuning between our laser an the reference equal to the provided offset via a feedback loop.
As laser source for the spin-dependent potentials we use a commercial 671 nm diode laser (Toptica D.L. Pro) which is amplified by an external home-made tapered amplifier [75]. The reference for locking the frequency of our laser is provided by a beam derived from the D_2 laser of the main experimental apparatus, which is locked to the $|F = 3/2\rangle \rightarrow |F' = 5/2\rangle$ hyperfine transition of the ^{6}Li D_2 line via Saturated Absorption Spectroscopy (SAS). However, due to the presence of a 140 MHz double-pass Acousto Optic Modulator (AOM) in the lock path, the frequency of this reference laser is 280 MHz red-detuned with respect to the atomic transition.

We report a scheme of the frequencies involved in the lock setup in Fig. 3.5.

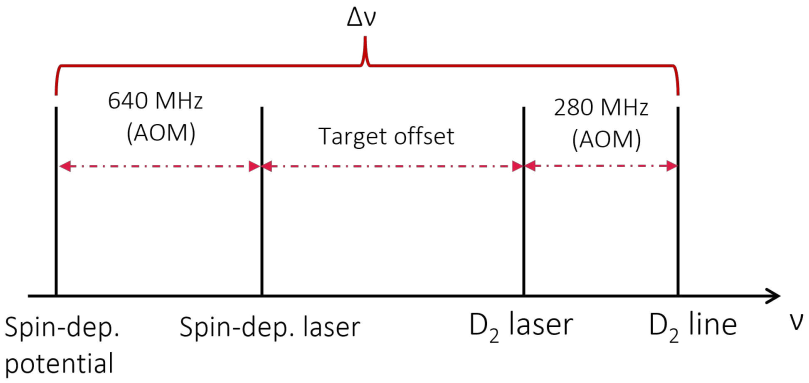

Figure 3.5: Frequency scheme of the lock setup. The D_2 reference laser is red-detuned compared to the atomic line by a -140 MHz double pass AOM. The laser source that we use for realizing spin-dependent optical potentials is locked to a target offset from the reference laser. Before impinging on the atomic cloud the spin-dependent beam is frequency shifted by -640 MHz through a -320 MHz double pass AOM. $\Delta\nu$ is the final detuning between the light used for the spin-dependent optical potentials and the D_2 line.

To compare the frequency of our source to the D_2 reference we superimpose two beams coming from the two lasers and we detect the combined light with a fast photodiode. The signal of this photodiode is then sent to the PLL, which acts as a feedback loop: it reads the beat note between the two frequencies, compares it to the externally provided frequency offset and outputs an error signal proportional to the phase difference between them. This output signal is amplified and sent to our laser driver which tunes the laser frequency in order to compensate for the error, thus allowing to set and stabilize the frequency of our laser by changing the target offset from the D_2 reference.

3.2.1 Phase-locked-loop scheme

The PLL circuit is based on a XOR gate which works as a phase detector and generates an output error signal that represents the phase difference between two input signals. In our case, one of the input signals is the beat note between our laser and the D_2 reference while the other is provided by a programmable frequency generator whose frequency is set at the target offset value for the frequency difference between the two lasers. The XOR gate output is zero when the two input signals are completely in phase, while it gets larger the more they are out of phase. Thus, the phase detector produces an output error signal proportional to the instantaneous phase difference between the inputs. This logic error signal is converted in an amplitude signal through a low-pass filter placed after the phase-detector. This filter includes a capacitor that gets charged when the error signal is high while it discharges when it is low. Therefore, a large phase difference between the signals generates a large voltage on the capacitor, i.e. a large output signal from the phase detector. This signal is sent to the driver of our laser, which acts on the diode injection current in order to reduce the phase difference between the input signals. A change in diode current results in a change in temperature of the active medium inside the

laser, which affects its index of refraction and the cavity's optical length. Therefore, by acting on the injection current of our laser we are able to finely tune the frequency of our laser and to stabilize it to a desired detuning from the D_2 reference. We report a simple scheme of the PLL circuit in Fig. 3.6.

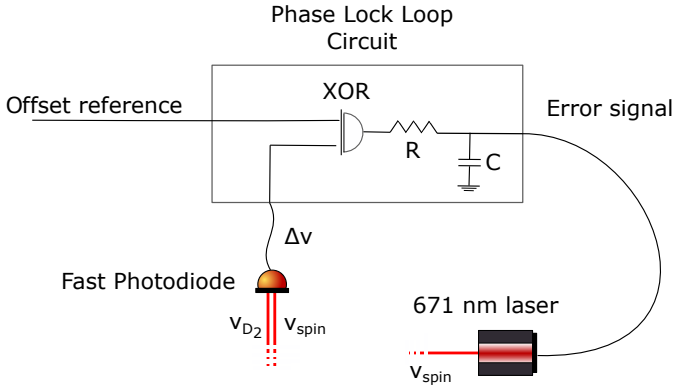

Figure 3.6: Phase Lock Loop circuit. The PLL reads as input the beat note signal ($\Delta\nu$) between our 671 nm laser source (ν_{spin}) and a laser locked to the ^{6}Li D_2 line (ν_{D_2}). The circuit also read a reference signal with frequency equal to the target offset. Using a XOR gate as a phase detector and a low pass filter it outputs an error signal that acts on the diode current of our laser to set the beat note signal equal to the offset reference.

3.2.2 Implementation of the offset-lock setup

In order to set and stabilize the frequency of our laser source using the described PLL-based offset-lock we implement an experimental setup on a dedicated optical table. We report an optical scheme and a picture of our setup in Fig. 3.7.
We use a polarizing beam splitter (PBS) to split the laser beam coming from our source into two paths, a main path that is carried to the main experimental table and shone on the atomic cloud and a secondary path that we use for locking the laser frequency. Through a set of $\lambda/4 - \lambda/2$ waveplates we tune the intensity ratio between the main and the secondary path to be around 90:10. The main path, carrying most of the power ($\sim$ 35 mW), passes through a double pass -320 MHz AOM which provides a -640 MHz shift. This AOM allows to control the beam intensity and could in principle be used to finely tune the light frequency. However, we never use it to this purpose as the degree of control on the frequency provided by our offset-lock is satisfactory for our needs. On the other hand, we use this AOM to produce short light pulses by turning on and off its radiofrequency injection. After the AOM, the polarization of the main beam is stabilized by a set of $\lambda/4 - \lambda/2$ waveplates and the beam is coupled to a polarization-maintaining optical fiber which carries the light to the main experimental apparatus, where it is further manipulated before being shone on the atomic sample.
The secondary path is used for the offset lock itself. The lower power beam ($\sim$ 5 mW) is superimposed with the reference beam which is obtained from a secondary port of the the D_2 laser and it is carried to the lock-dedicated optical table through an optical fiber. The combined light is focused on a fast photodiode (818-BB-45A Amplified High Speed Photodetector, 20 kHz - 10 GHz bandwidth) which detects the beat note between the two beams, corresponding to the

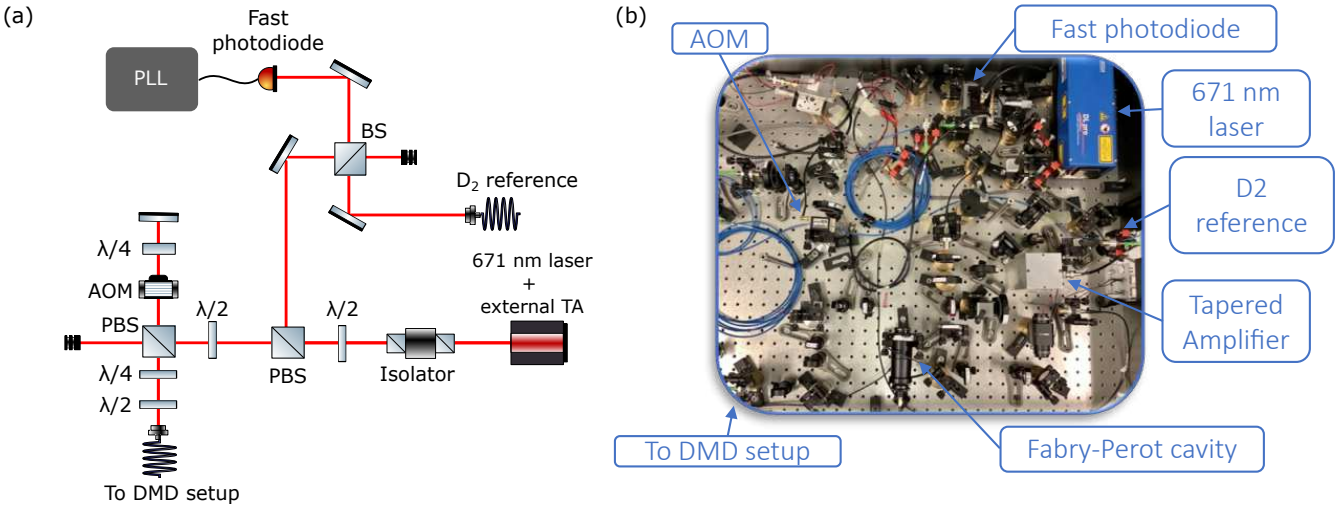

Figure 3.7: Optical scheme (a) and picture (b) of the offset-lock setup. We split the beam coming from our 671 nm laser into two paths. The light from the main path goes through a -320 MHz double pass AOM and it is carried to the DMD setup in the main experimental apparatus with a polarization-maintaining optical fiber. The secondary beam is combined with a beam originating from the D_2 reference using a 50%-50% beam splitter. The combined light is detected by a fast photodiode which provides the beat note signal for the PLL circuit. The Fabry-Perot cavity in (b) is not strictly necessary for the offset-lock and we use it only for checking that our laser source is single-moded before locking.

frequency difference between our laser and the reference. The output signal of the photodiode is split into two equal-amplitude signals using a RF power splitter (model: ZX10-2-183-S+). One signal is sent to a spectrum analyzer (Tektronix RSA306B) for monitoring the beat note between the lasers, the other is amplified by +15 dBm with a ZX60-6013E-S+ amplifier and then sent as input to the PLL circuit. The PLL reads the beat note signal and compares it to an externally provided frequency offset which we produce using an appropriate function generator. The output error signal of the PLL is then sent to the laser driver and the laser frequency is tuned to stabilize the beat note frequency to the desired offset reference.
Our offset lock is efficient only if the detuning between our unlocked laser source and the D_2 reference is already close to the target value. Therefore, before being able to lock we have to adjust the laser frequency by tuning the laser current, temperature and the laser piezoelectric voltage control, which changes the length of the external cavity. We measure the D_2 laser wavelength with a wavemeter, then we use the same wavemeter to measure the wavelength of our laser source and we tune the parameters at our disposal to bring this wavelength close to that of the D_2 laser. As we change the laser wavelength, we use a Fabry-Perot cavity to monitor that the laser remains single-moded. Once the detuning between the two lasers is sufficiently small (a few GHz) we can monitor the beat note peak with the spectrum analyzer and use only the piezoelectric control to bring the peak close ($\sim$ 300 MHz) to the target offset. We use a function generator to generate a periodic signal of 1.5 V amplitude with a frequency equal to the target offset and we feed this signal as input to the PLL circuit. When we turn the PLL circuit on, we see the beat note signal shift and stabilize to the target offset value. We confirm

the efficiency of our lock by changing the target offset and observing the beat note signal change accordingly. Further, when our laser is locked we are not able to change the beat note frequency by slightly touching the laser's piezoelectric control, since the PLL circuits locks its frequency.
To realize a spin-selective optical potential in a non-interacting Fermi gas using π-polarized light (see next section for the choice of light polarization) we need to lock our laser at a detuning of ~ -6.1 GHz from the zero-field D_2 line. Due to the presence of the -280 MHz AOM in the lock path of the D_2 laser and the - 640 MHz AOM in the main path of the spin-dependent laser source, we effectively need to lock our laser to an offset of $-6100 + 280 + 640 = 5180$ MHz from the D_2 laser. Our setup allows us to lock to such offset and we report a comparison between the locked and unlocked beat note signals measured with the spectrum analyzer in Fig. 3.8. When our laser is unlocked, the beat note peak is unstable due to the laser's fluctuations and it drifts with time due to thermal effects. Once the laser is locked the beat note peak is, instead, centered on the provided offset, having only a small jitter due to high-frequency fluctuations.
With our setup, we achieve frequency locking for offsets between 0 and – 5.5 GHz, with a jitter of about 2 MHz. This stability allows us to reliably lock at a frequency where the two spin states have oppositely-signed light shifts, since this happens in a ~ 160 MHz wide region (see Fig. 3.4). To produce a spin-selective potential we need to fix the frequency of our laser as close as possible to the zero crossing of the polarizability for one spin state which requires locking our laser with higher precision compared to the previous case. However we find that, locking the frequency to the zero crossing for one state, the jitter of our laser results in a frequency uncertainty that is sufficiently small to have a spin-selective potential. In fact, an uncertainty of 2 MHz around the zero-crossing of one state results in a polarizability for such state that is at most $\pm$ 0.5% that of the other state. Therefore, with our set up we can reliably lock at frequencies resulting in both spin-dependent and spin-selective optical potentials for all three ^{6}Li lowest Zeeman states.
Our lock is stable for long period of times (hours) and it is robust against ambient noise. However, we see a general tendency of our lock to become less stable as we increase the size of target offset below -5.5 GHz. We ascribe this to the difficulty of our PLL circuit in processing high-frequency signals. This could become a limit of our setup in the investigation of weakly interacting Fermi systems. In fact, reducing the magnetic field from 572 G (non-interacting Fermi gas) to 300 G (weakly-interacting Fermi gas) results in a ~ -270 MHz shift in the zero crossings, which would push our lock to its limit. However, this limit can be easily overcome by employing appropriate tools for manipulating the input signal of the PLL circuit and reducing its frequency. By inserting a HMC-C006 divide-by-4 prescaler before the PLL circuit we have been able to feed to the circuit a signal whose frequency is four times lower than the real beat note signal, thus effectively reducing the target offset of the PLL. In this way we can in principle lock our laser up to a ~ -20 GHz offset from the D_2 line which is a detuning far larger than our needs, being the D_1 transition at ~ -10 GHz from the D_2. Further, we observe that inserting the frequency-divider results in a slightly more precise and stable lock.
Another way of reducing the input offset frequency of the PLL circuit, while maintaining the spin-selective nature of the potentials, is to tune the light polarization. We have seen that for π-polarized light the zero-crossing of the polarizability is found at ~ -6 GHz from the D_2 line, which is close to the limit of our lock setup. The zero-crossing for σ^+-polarized light is, instead, much closer to the atomic line (~ -2 GHz). Thus, realizing a spin-selective optical potential using σ^+-polarized light requires locking at a lower offset, which is less demanding for our circuit. For experimental reasons (see next section), we choose to work with π-polarized light. However,

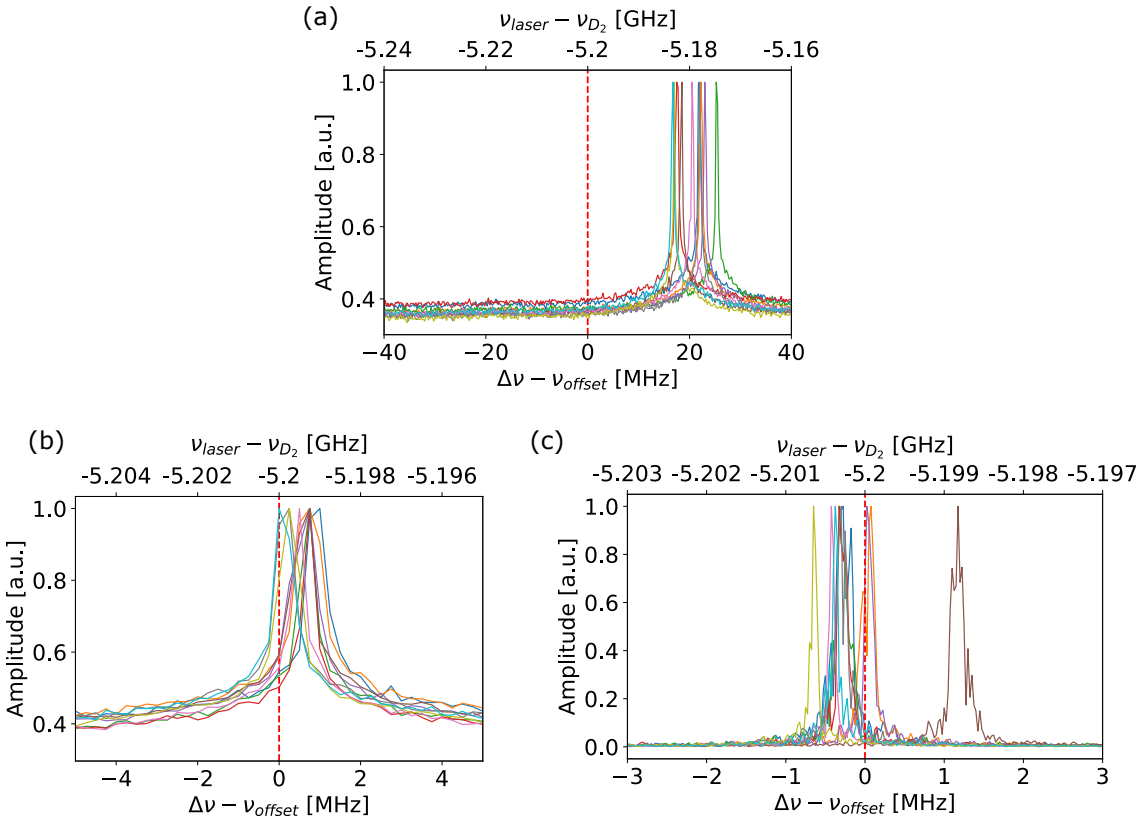

Figure 3.8: Beat note signal for -5.2 GHz target offset. When the laser is unlocked (a) but it is brought close to the target frequency with the piezoelectric control, the beat note peak drifts with time and it is not fixed at the target frequency. When the laser is locked (b, c) the lock circuit keeps the beat note peak at less than 1 MHz from to the target offset. The red dashed line indicates to the target frequency offset of - 5.2 GHz, corresponding to an optical potential that is selective for state $|3\rangle$ (i.e. the light shift of $|1\rangle$ is zero while that of $|3\rangle$ is not) of a $|1\rangle - |3\rangle$ non-interacting Fermi gas. The beat note signal is measured with a Tektronix RSA306B spectrum analyzer and is reported in logarithmic (a, b) and linear (c) scale. Data correspond to 10 successive measurements of the beat note signal taken at a few seconds steps.

we will see that the presence of a small σ^+ component in the polarization does indeed help in reducing the detuning necessary for the realization of spin-selective optical potentials.

3.3 Tailoring the optical potentials

Once we have set and stabilized the frequency of our laser source with the offset-lock setup we can shine our spin-dependent optical potentials on the atomic cloud. To this end, we couple the main beam of our laser source to a polarization-maintaining optical fiber and we carry it to the main experimental apparatus. Out of the fiber, our beam has a Gaussian intensity profile, thus resulting in a Gaussian-shaped potential on the atomic cloud.
However, being able to manipulate the light intensity spatial profile opens the possibility to

sculpt the potential felt by the atoms and realize arbitrarily shaped optical potentials. To this end, an entire class of devices, the Spatial Light Modulators (SLMs) has been exploited in recent years. In our experiment, we shape the intensity profile of our laser beams using two Digital Micromirror Devices (DMDs), each composed by a grid of tiltable square micromirrors. The tilt state of each mirror can be independently controlled by applying an external voltage to set it into an ON or OFF state. Mirrors in ON and OFF states reflect the light impinging on the device in different directions, so that a DMD acts as a light mask. In fact, when a black-and- white image is loaded on the device, the DMD mirrors are arranged in the ON and OFF states and the intensity profile of the light reflected in the ON direction has the same shape of the binary image sent to the DMD. The DMD can be used in both static and dynamic mode, thus allowing to generate both stationary and time-dependent tailored optical potentials. In our setup we use a DMD for manipulating a 532 nm green beam to shape repulsive optical potentials (see Chapt. 1 and Ref. [27] for details) and we implement a new DMD for tailoring the spin-dependent potentials.

3.3.1 Digital Micromirror Device static characterization

The DMD we use for tailoring the spin-dependent potentials is a DLP9500 0.95" produced by Vialux, with a V4395 board. This device is composed by an 1920×1080 array of square micromirrors, with 10.8 μm pitch.
Each mirror can be independently tilted over its diagonal axis by an angle of 12°. The state of a single mirror is thus binary and can be accessed using a computer through the board. Mirrors can be arranged in any kind of binary pattern to reproduce a previously generated black and white image. Pictures of the DMD, of its board and mount are reported in Fig. 3.9 together with a sketch of the tiltable mirrors functioning.

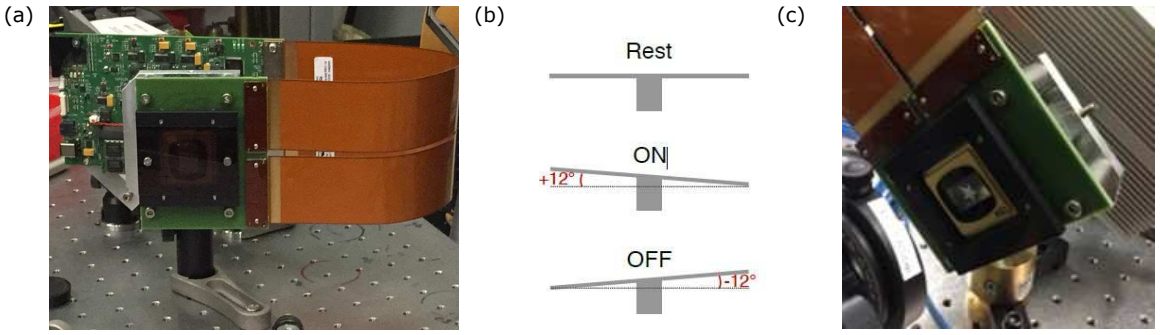

Figure 3.9: The Digital Micromirror Device (DMD). (a) Picture of the DMD at rest with its control board and mount. (b) Sketch of the tilt states of the DMD: when the DMD is off all micromirrors occupy the rest position. When a voltage is applied to a mirror it tilts by either +12° or -12°, labeled as ON and OFF state, according to the sign of the voltage. Mirrors in different states reflect light in different directions, thus acting as a light mask. (c) DMD mounted at 45° and displaying the image of a star.

To fully understand the optical behavior of the DMD, its diffraction properties have to be taken into account. In fact, the DMD is composed by an array of micrometer-sized mirrors that have a dimension comparable to that of the impinging laser light ($0.5 - 0.7$ μm). Thus, the DMD acts

as a diffraction grating that reflects the incident light into several diffraction orders and not only in the two directions defined by the tilt state of the mirrors. This is an unfavorable situation since only one order can be used for shining the light on the atomic cloud. However, the light power in the main order can be maximized by fulfilling the blazing condition of the diffraction grating. We refer to References [27, 33] for a detailed description of the blazing condition for a DMD. We find the blazing condition by optimizing the light intensity in one of the diffraction orders (the central order), which we do by slightly changing the relative angle between the DMD surface and the impinging beam. It is worth mentioning that, while obtaining the blazing condition, it is preferable to have the smallest possible angle between the normal to the DMD surface and the reflected beam. This means that the plane where the DMD surface lies is almost orthogonal to the propagation direction of the reflected light, which is useful to avoid aberrations and distortions in the DMD image caused by an imaging setup aligned to the selected order. Since the square micromirrors are tilted along their diagonal axis, if we mount the DMD parallel to the horizontal plane (as in Fig. 3.9 (a)) the reflected light will not travel along the horizontal direction but will be tilted with respect to the horizontal plane and the propagation direction of the light will have a vertical component. This is particularly unpractical for building an optical path for this light. To avoid this, we rotate the DMD by 45° respect to the horizontal plane as in Fig. 3.9 (c). In this way the tilting angle of the micromirrors is horizontal and the light is completely reflected along the horizontal direction. By comparing the power of the impinging and reflected light we optimize the reflection efficiency of the central order to be around 60%.

3.3.2 Digital Micromirror Device dynamic characterization

One of the most appealing properties of the DMD is the possibility to store a sequence of images into its memory and then display them at fixed time intervals to obtain a time-dependent light pattern. The dynamical properties of the DMD can therefore be used to project time-dependent optical potentials on the atomic cloud. This was done in previous works by our group where the Vialux V-7000 DMD working with blue-detuned green light was used for moving a repulsive barrier [22, 23] or a couple of beams [24] in the atomic cloud. The crucial parameter determining the dynamical properties of the DMD is the maximum switching rate of the device. For our Vialux DLP9500 DMD the nominal switching rate is 17.857 kHz, corresponding to a minimum picture time of 56 μs. To test the dynamical properties of the DMD we switch the displayed image between a completely black (all mirrors in the ON state) and a completely white (all mirrors in the OFF state) image. We shine laser light on the DMD displaying the white image and we set the DMD to work in SLAVE mode, so that the sequence timing is controlled by external triggers. We align a photodiode along the main order of diffraction for the ON direction, using an iris to block all the other orders, and we switch between black (ON) and white (OFF) images. By monitoring the rise time of the photodiode signal and changing the switching rate between the images we are able to characterize the dynamical properties of our DMD. We find that the minimum picture time is indeed 56 μs, corresponding to the nominal switching rate of $\sim$18 kHz. Despite being a few GHz out of resonance, our spin-dependent perturbations are not detuned enough to completely neglect photon absorption. For this reason, if we want to introduce non-dissipative effects on our sample, we cannot shine our light on the atomic cloud for long times, unless drastically reducing the light intensity. It is therefore necessary to produce short light pulses in order to minimize the exposure time of the atoms to our laser. The tools that allow

us to generate light pulses from a continuous source are the -640 MHz AOM in the main optical path and the DMD itself. In Fig. 3.10 we report a comparison between 100 μs pulses produced with the DMD (a), the AOM (c) and a combination of the two (b). To characterize our pulses

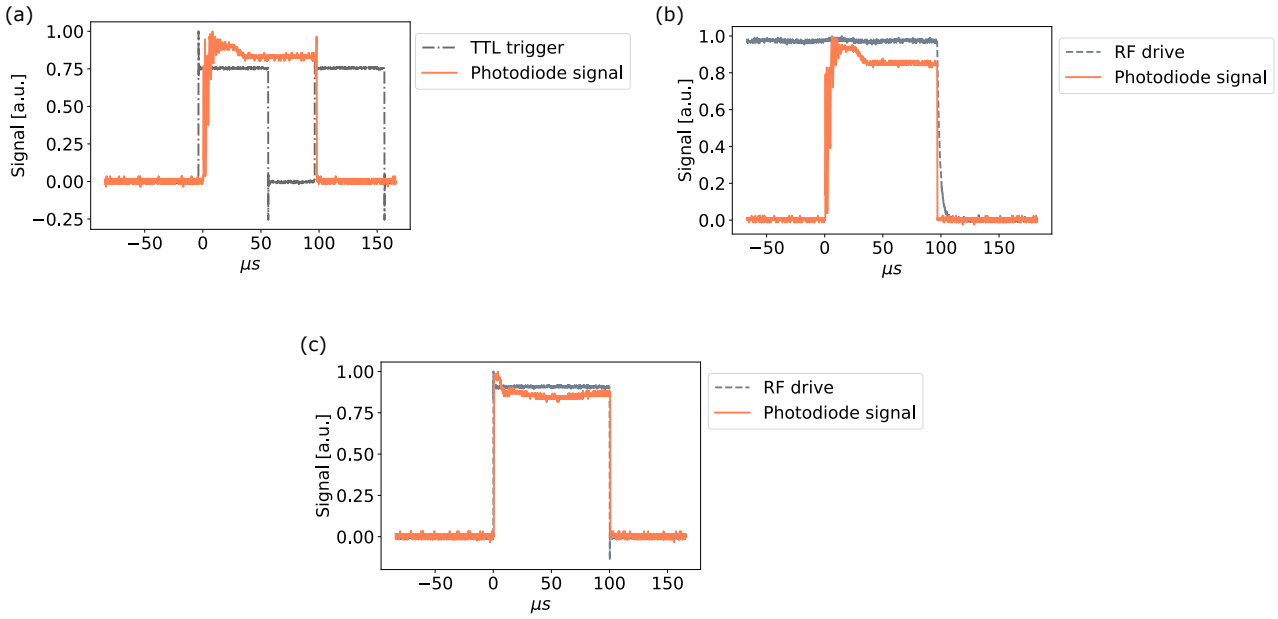

Figure 3.10: Comparison between 100 μs pulses produced using the DMD and the AOM. We report the light detected by the photodiode aligned on the ON direction of the DMD for pulses produced in different ways. (a) DMD pulse: light is always impinging on the DMD and the pulse is produced by switching between a white (OFF direction) and a black (ON direction) image. We also report the TTL trigger signal that controls the DMD switching in SLAVE mode. (b) DMD and AOM pulse: the pulse is started by switching from a white to a black image as before but it is ended by turning off the radiofrequency injection of the AOM. Since the beam passes through the AOM before impinging on the DMD, turning off the AOM results in the light not impinging on the DMD, thus ending the light pulse. (c) AOM pulse: we keep the DMD stationary on the ON image and we produce the pulse turning on and off the radiofrequency injection of the AOM.

we again use the photodiode aligned on the ON direction of the DMD-reflected light. One way of shining our tailored potentials for only a short time is to use the DMD as a switch, alternating between white and black images. In this case, light is always impinging on the DMD which starts from a white (OFF) image. The pulse is then obtained by switching to a black (ON) image and then back to a white one. Since light arrives to the photodiode only when the DMD displays a black image, it is possible to use the DMD to produce short light pulses (Fig. 3.10 (a)). However, producing light pulses in this way presents some limitations as it is impossible to produce pulses shorter than the minimum DMD picture time (56 μs). To overcome this limitation it is possible to produce pulses using a combination of both the AOM and the DMD (Fig. 3.10 (b)). Since the laser beam passes through the AOM before impinging on the DMD, by turning off the radiofrequency injection of the AOM the laser beam is blocked before reaching the DMD, thus providing a way of ending the light pulse without switching the DMD

back to a white image. In this way we can obtain light pulses that are shorter than the minimum picture time of the DMD, since during the pulse sequence the DMD switches image only once. However, such pulses are again not satisfactory because when the DMD switches between a white and a black image it needs to tilt all its micromirrors, which results in a transient of ~ 20 μs. During this transient time the light intensity on the photodiode changes non-monotonically until it reaches a stable value. Since 20 μs may be a time comparable, or even longer, than the target pulse duration, this transient time makes the DMD unsuitable for producing short light pulses. Therefore, for stabilizing the pulses we let the DMD display a stationary black (ON) image and we make the pulses using the AOM only. By turning on and off the radiofrequency injection of our double-pass AOM it is possible to either let our beam pass through or to block it. In particular, we can keep the radiofrequency injection off, therefore blocking the beam, and then turn it on and off again for producing a short light pulse (Fig. 3.10 (c)). The AOM has a much faster response and a much shorter transient time compared to the DMD, which makes it an optimal tool for the generation of short light pulses. For this reason, in all our experiments we keep the DMD stationary and we produce light pulses using only the AOM, even when we do not need to use very short pulses.

3.3.3 Optical layout

We design and build an optical setup for shining our DMD-tailored spin-dependent optical potentials on the atomic cloud. Since we already have two beams propagating along the vertical direction (the green beam for the repulsive potentials and the vertical imaging beam) we choose to shine our spin-dependent potentials along the horizontal direction, exploiting one of the side windows of the vacuum cell. As for the green DMD setup we take advantage of the vertical imaging path for focusing and demagnifying the tailored potentials, we make use of the horizontal imaging setup for doing the same with the new DMD. We show a scheme of the vacuum cell indicating the direction of the vertical imaging light as well as that of both the green (repulsive) and red (spin-dependent) DMD-shaped lights in Fig. 3.11 (a).
We report in Fig. 3.12 an optical scheme of the whole experimental setup for DMD-tailoring and shining the spin-dependent potentials on the atomic cloud from the horizontal direction. As previously mentioned, we carry the main beam of our laser source from the dedicated offset-lock optical table to the main experimental apparatus using a polarization maintaining optical fiber. We use a $\lambda/2$ waveplate and a PBS to split the laser beam into two beams, of which one carries most of the power ($\sim$ 10 mW) and is shone on the atomic cloud after passing through other optical elements and the other ($\sim$ 1 mW) is detected by a photodiode for stabilizing the light intensity. To keep the ratio between these two beams constant over time we have to stabilize the polarization of our laser light before it enters the optical fiber. For this reason, we insert the set of $\lambda/2 - \lambda/4$ waveplates before the optical fiber on the offset-lock table (see Fig. 3.7) and we tune them to stabilize the polarization of the beam emerging from the fiber, using a Schäfter-Kirchoff polarimeter for monitoring such polarization.
The beam reflected by the PBS is detected by a photodiode whose output signal is monitored with an oscilloscope and sent as input to a proportional–integral–derivative controller (PID). Feeding the output signal of the PID to the radiofrequency driver of the AOM in the path of our beam allows to tune the radiofrequency power and thus control the intensity of our light. Further, it is possible to use the PID as a feedback loop for stabilizing the light intensity in

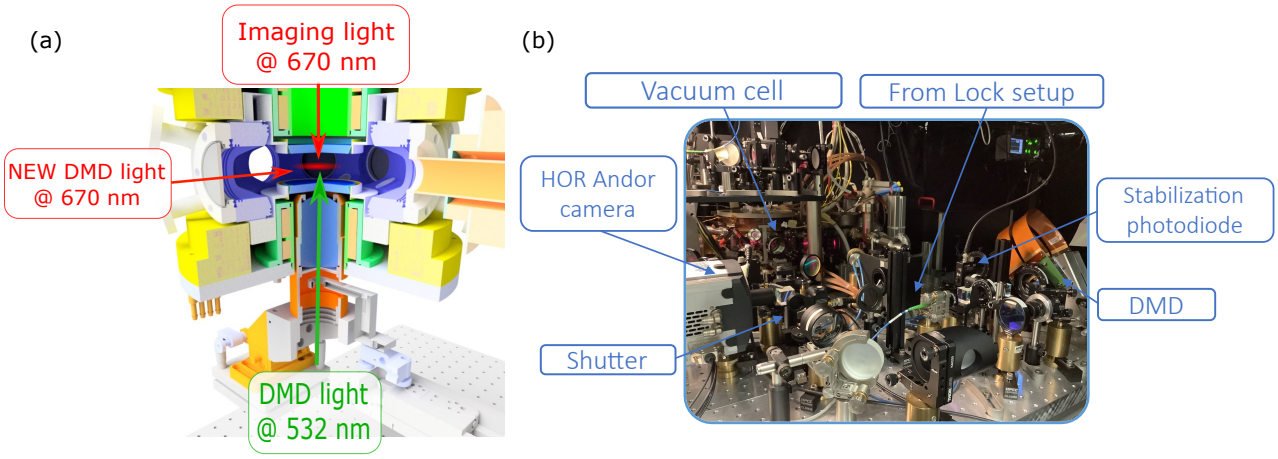

Figure 3.11: Horizontal setup for shining DMD-shaped laser light on the atomic cloud. (a) Scheme of the vacuum chamber with the vertical imaging light and the two DMD-shaped beams shone on the atomic sample from the bottom (green DMD) and the side (spin DMD). (b) Picture of our experimental setup for shaping the spin-dependent optical potentials and shining them on the atomic cloud.

order to compensate possible fluctuations of polarization and AOM efficiency. Wse can input the target intensity into the PID from the control program, measure the light intensity detected by the stabilization photodiode and, after an appropriate calibration, use the PID to tune the AOM power in order to set and stabilize the light intensity to a target value.
The transmitted beam, instead, impinges on the DMD and it is reflected back with the desired intensity profile. By optimizing the angle between the DMD and the impinging beam we are able to superimpose the incoming and the DMD-reflected beam so that the latter is again impinging on the PBS. Inserting a $\lambda/4$ waveplate between the PBS and the DMD allows to rotate the polarization of the incoming beam by 90° since the light passes through the waveplate twice. Thus, while the beam impinging on the DMD is transmitted through the PBS, the DMD-reflected beam is reflected by the PBS in the direction opposite to that of the stabilization photodiode. Since the DMD acts as a diffraction grating, the reflected light consists of many diffraction orders that we block by inserting an iris right after the PBS. In this way we are able to keep only the main diffraction order, whose power is maximized by fulfilling the blazing condition. This beam has an arbitrarily-shaped intensity profile and it is the beam that we use for realizing our tailored, spin-dependent optical potentials.

3.3.4 Focusing and demagnifying the laser beam

Manipulating an atomic sample with arbitrary optical potentials requires to demagnify the laser beam used for their realization and to focus it on the atomic cloud. In fact, what it is actually needed is an imaging setup that projects the image produced by the DMD on the atomic sample. For this reason we take advantage of the pre-existent horizontal imaging path that allows us to focus our spin-dependent potentials on the atomic cloud an to demagnify our beam by a factor 6.8. However, this demagnification is not sufficient for manipulating our sample with high spatial resolution and for producing smooth potentials. In fact, each DMD micromirror has a 10.8 μm

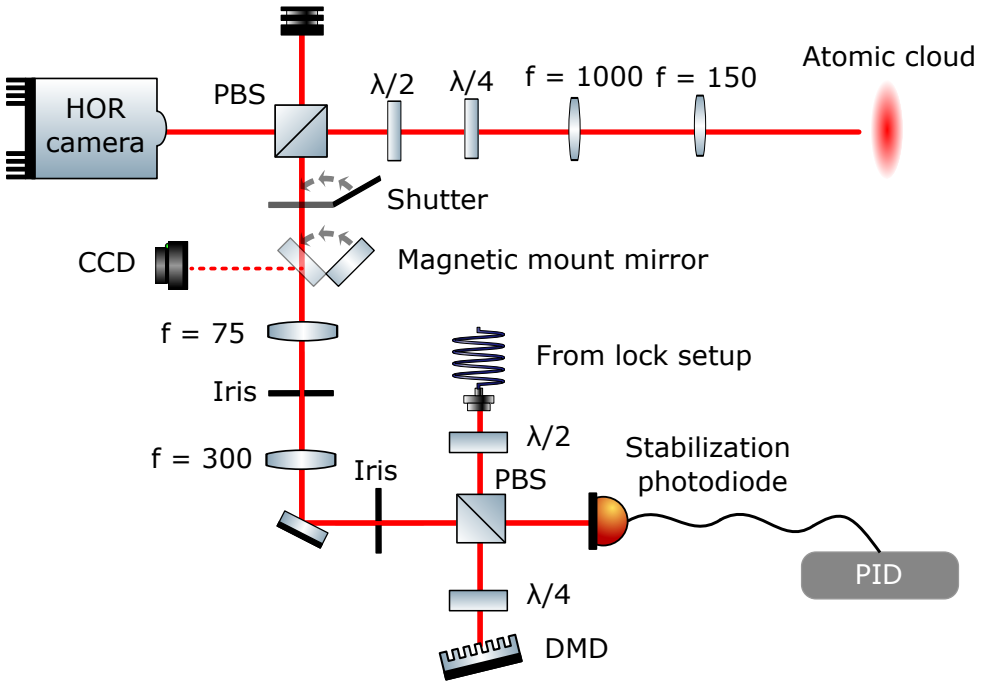

Figure 3.12: Optical scheme of the horizontal setup. We use the DMD to tailor the beam coming from the dedicated offset-lock table and realize arbitrarily-shaped spin-dependent optical potentials. We take advantage of the horizontal imaging optical path for demagnifying, focusing and shining our laser light on the atomic cloud.

side which, considering a demagnification factor of 6.8, results in a $\sim$ 2.5 μm^2 square on the atomic cloud. Since the typical size of the sample in the optical dipole trap is $\sim$300 μm, but it can be much smaller when trapped in different geometries, we cannot consider a potential that is discretized in pixels of a few micrometers to have a smooth spatial profile. Further, having such a low demagnification prevents us from manipulating our sample with local perturbations below a few micrometers size. For these reasons, we add to the optical path another telescope composed by a couple of lenses with focal length $f_1 = 300$ mm and $f_2 = 75$ mm respectively. The two lenses are positioned at a relative distance equal to $f_1 + f_2 = 375$ mm, so that the expected telescope demagnification is $300/75 = 4$. This telescope is coupled with an iris placed between the two lenses, in correspondence of the focal point of the first one. This iris acts as a spatial filter cutting the high frequency components of the DMD image. This effectively smooths the image intensity profile thus helping to realize smooth potentials on the atomic cloud, starting from a black and white image on the DMD.
To measure the actual magnification of our telescope we add a mirror after the second lens, mounting it on a magnetic base so that it can be inserted or removed at will without losing track of its previous position in the optical path and alignment. We focus the reflected light on a Thorlabs CCD camera, we display on the DMD an image of 3 dots of well known distance and we acquire a picture of the resulting image on the camera. Fitting each dot with a two-dimensional Gaussian we can find their relative distance on the camera and comparing such value to their distance on the DMD screen we can find the demagnification of our telescope. We

report an example of one of the images used for measuring the demagnification in Fig. 3.13. The measured demagnification factor for our telescope is 4.05(3), which is consistent with our expected value of 4.

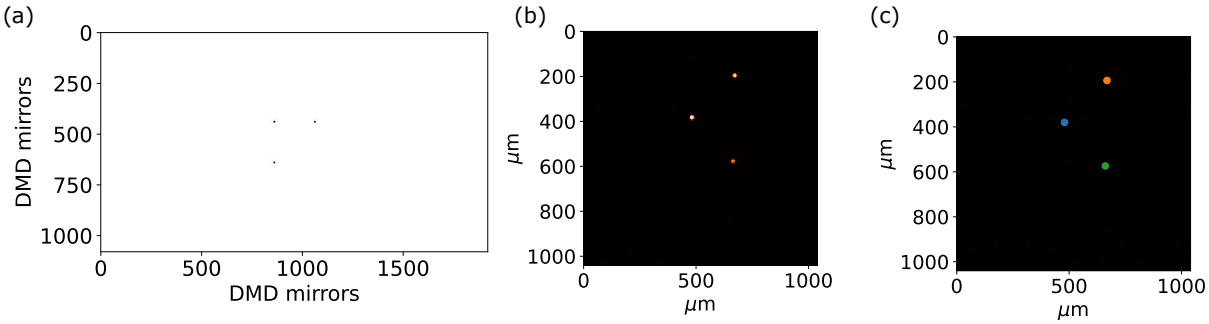

Figure 3.13: Telescope demagnification measurement. (a) Calibration image displayed on the DMD screen. (b) CCD camera picture of the three dots displayed on the DMD screen. (c) Coordinates of the three dots in the CCD screen found by fitting each of them with a two-dimensional Gaussian function.

To properly focus the image of the DMD-shaped light on the atomic cloud, the distance between the first lens and the DMD must be equal to the lens' focal length (300 mm), so that the DMD, which generates the image, is in the lens' focal point. Analogously, the distance between the second lens of our telescope and the first lens of the horizontal imaging telescope must be equal to the sum of their focal distances ($75 + 1000$ mm). This double telescope allows us to achieve a total demagnification factor of 27.2, resulting in each DMD micromirror being focused on the atomic cloud as a $\sim 0.16\,\mu\text{m}^2$ square. In this way we are able to manipulate our sample with good spatial resolution ($\sim 5\,\mu$m) and to efficiently tailor our intensity profile to produce spatially smooth potentials.
We use the CCD camera and the magnetic mount mirror also for monitoring and feedbacking the intensity profile of our DMD-tailored beams. In fact, since the beam impinging on the DMD has a Gaussian profile, the reflected light will retain its Gaussian shape on top of the profile determined by the image displayed on the DMD. To remove this undesired Gaussian shape from our potentials we use a feedback program that compares the target intensity profile to an image of the beam taken with the CCD camera. We will describe the feedback program in more detail in Chapt. 4.

3.3.5 Realizing spin-dependent light pulses

Right after the removable mirror we insert a shutter for blocking our laser beam during most of the experimental cycle. As mentioned before, our spin-dependent perturbations are always accompanied by a non-negligible photon absorption probability. Therefore, we have to shine our light on the atoms only for short time intervals. We do this by using the radiofrequency control of the AOM for producing light pulses in the μs - ms range. However, keeping the AOM off for the whole experimental cycle (~ 10 s) and turning it on only for a short pulse hinders the PID stabilization, since the PID does not have sufficient time to efficiently stabilize the light intensity. Moreover, once the AOM itself is turned on it needs some time to thermalize before

reaching its stationary working condition. This makes the pulses obtained by keeping the AOM off for most of the experimental cycle quite unreliable and shot-to-shot dependent. To overcome this problem we keep our AOM working at a stabilized power for most of the experimental cycle and we block the laser beam using the shutter inserted in the optical path. The transient time for the shutter to switch between its closed and open states is of the order of 500 ms. Therefore, we open the shutter ~ 500 ms before producing the light pulse and at the same time we turn off the AOM radiofrequency injection so that no light is shone on the atoms as long as the shutter is still opening. After the shutter is completely open we make a short pulse with the AOM, thus applying the spin-dependent perturbation for a short time, and we close the shutter, turning the AOM on again only when the shutter is completely closed. An overview of the experimental sequence for shining short light pulses on the atomic cloud is reported in Fig. 3.14.

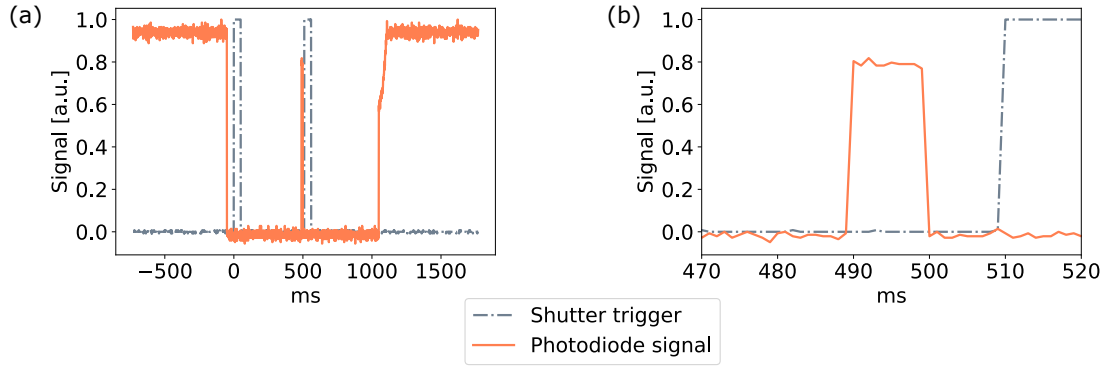

Figure 3.14: Pulse generation sequence. We report the light detected by the stabilization photodiode (orange line) and the trigger signals (dotted gray lines) for changing the shutter state. Since the stabilization photodiode is positioned before the shutter it detects a signal even when the shutter is closed, while the light is shone on the atoms only as long as the shutter is open. (a) The AOM is working and it is stabilized for the whole experimental cycle until the realization of the light pulse. 500 ms before the pulse (0 ms in the plot) the AOM power is turned off and the laser beam is blocked before arriving to both the photodiode and the shutter. At the same time the shutter is opened by the first trigger. After the shutter's transient time (500 ms) we quickly turn on and off again the AOM power to make a short light pulse and we close the shutter again with the second trigger. After the shutter is completely closed we turn the AOM on again for the next experimental cycle (1000 ms on the plot). (b) Zoom in the pulse region.

Thanks to this protocol, we are able to produce pulses that are stable and reproducible over all experimental cycles. However, we cannot produce arbitrarily short pulses as both the PID control and the AOM itself have typical transient times that need to be taken into account. In particular, we find that even optimizing the PID parameters for having the fastest response possible it is difficult to stabilize pulses below a few tens of microseconds. In Fig. 3.15 we report the profile of pulses of 50, 20 and 10 μs. While the 50 μs pulse is stabilized quite efficiently, the shortest pulses are more difficult to stabilize as the rise time of the pulse becomes comparable with the pulse duration itself. Despite being not ideal, it is still possible to work using such short pulses since, even though they may not be fully stabilized, they appear to have low shot-to-shot fluctuations. Of course an alternative approach is to reduce the light intensity and work with

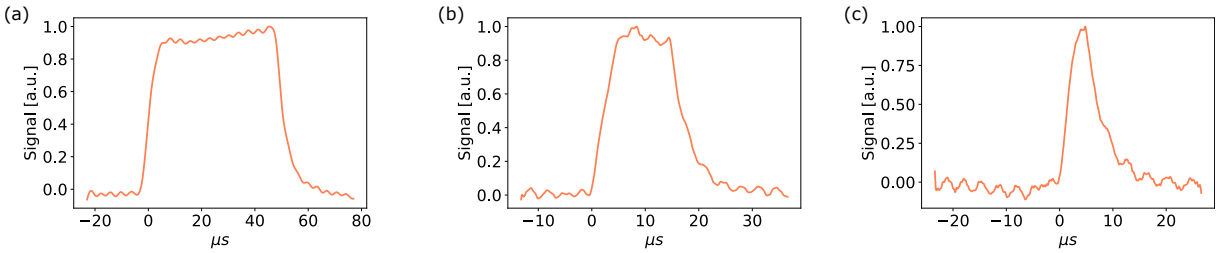

Figure 3.15: Short AOM pulses stabilization. It is difficult to stabilize the shortest light pulses since both the AOM and the PID have typical response times that need to be taken into account. While we can successfully stabilize a 50 μs pulse (a) we are not able to completely stabilize a 20 (b) or 10 μs pulse (c), since the rise time of the AOM is of the order of 5 μs, which is comparable with the pulse duration. Signals are detected using the stabilization photodiode which has an estimated rise time of 0.12 μs, much smaller than the other elements' typical timescales.

slightly longer pulses.
As we have seen in section 3.1, the light polarization plays a central role in the realization of the spin-dependent optical potentials. For controlling the light polarization we insert a set of $\lambda/2 - \lambda/4$ waveplates that allow us to tune the light polarization at will. However, when tuning the polarization we have to consider the geometry of our experimental setup. Since our laser beam is propagating along the horizontal direction and the Feshbach magnetic field, which defines the quantization axis of our system, is aligned vertically, the propagation direction of the light and the quantization axis are orthogonal. This prevents us from using σ-polarized light for the generation of our spin-dependent optical potentials. In fact, for having a pure σ^+ or σ^- polarization it is necessary to have a circular polarization and the electric field must rotate around the quantization axis, which is impossible in our geometry since the light propagates orthogonally to the magnetic field direction. Therefore, in our setup any non-linear polarization results in a non-trivial polarization on the atomic cloud. On the other hand, we can set the polarization to be linear and align it to the vertically magnetic field, thus obtaining π-polarized light. As we have seen in section 3.1, this light polarization is optimal for the realization of spin-dependent and spin-selective optical potentials. Therefore, we tune the $\lambda/2 - \lambda/4$ waveplates in order to obtain a light polarization that is maximally linear and we align it parallel to the vertical direction. For monitoring the polarization while we tune the waveplates we use the Schäfter-Kirchoff polarimeter that we insert in front of the vacuum cell window. We are able to obtain a $\sim 98\%$ linear polarization tilted by less than 1° from the vertical axis. Moreover, in these polarization measurements the vertical axis is the internal axis of the polarimeter which may be slightly different from the magnetic field direction. As we will see in the next chapter, this non perfect linear polarization and the misalignment between the polarimeter and magnetization axis may result in a non perfect π polarization on the atoms. In conclusion, exploiting all the elements of our experimental setup we are able to produce short light pulses of tailored spin-dependent or spin-selective optical potentials and to use them for manipulating our atomic sample.

Chapter 4

Testing the spin-dependent optical potentials

In this chapter we demonstrate that our experimental setup allows us to realize both spin-dependent and spin-selective optical potentials. First we show that our offset-lock is capable of reliably locking our laser source to the atomic resonances of the two spin states by resonantly and selectively addressing each spin state in a non-interacting Fermi gas. In this way we demonstrate the efficiency of our lock and we open up the possibility of introducing local spin-selective dissipative perturbations. In the second part of this chapter we show how we can use the DMD for arbitrarily shaping the intensity profile of a laser beam and tailoring the spin-dependent potentials. In particular, we focus on using a feedback program for giving a linear shape to the intensity profile. In the third part of this chapter we demonstrate that we can realize both spin-dependent and spin-selective optical potentials by performing an optical Stern-Gerlach experiment. Finally, we give a brief outlook on the possibility of exploiting the spin-selective optical potentials for the generation of spin currents in our sample.

4.1 Producing a spin-selective dissipative perturbation

Computing the the photon scattering rates of the ^{6}Li Zeeman states we can quantify the dissipative effects introduced by our close-detuned laser light. Considering the case of a light resonant to the D_2 transition, the lifetime of the excited state is 27 ns [19] which is a time shorter than our experimental resolution. Therefore, each time a lithium atom absorbs a photon we can consider its momentum to instantly change by the sum of the momenta of the incoming photon and of the randomly emitted one. Each momentum transfer results in a recoil energy $\frac{(\hbar k)^2}{2m}$ corresponding to a recoil velocity $\frac{\hbar k}{m}$ where k is the momentum of the absorbed or emitted photon and m is the mass of a lithium atom. This recoil energy results in the atoms acquiring a kinetic and increasing their temperature accordingly. For for the D_2 line of ^{6}Li this recoil temperature is of the order of $3\,\mu$K. Thus, when photons are absorbed by an atomic ensemble which is colder than a few μK the temperature of the system inevitably increases. This will happen even if photons are absorbed by only a few atoms, since the hotter atoms will collide with their neighbors, leading to thermalization and heating of the whole sample. Therefore the main effect of shining near-resonant light on an interacting ultracold atomic gas is to increase its temperature.

When considering the effects of photon absorption in an ultracold sample we also have to take into account that the system is confined by an external trapping potential of fixed depth. If such depth was infinite, then atoms could not escape the trap and the only effect of photon absorption would be an increase in the temperature of the atomic sample. However, in real life experiments atoms are usually confined by optical potentials of finite depth. For this reason it is possible that the recoil energy acquired by an atom after absorbing a photon is sufficiently high that the atom escapes from the optical confinement and is lost from the experimental cycle.
Computing the scattering rates of the Zeeman states composing our sample allows to describe the photon absorption probability of atoms in different spin states. Since such spin states are separated by $80-160$ MHz, depending on the considered states, their resonances will be splitted by a comparable gap. This splitting allows us to lock a laser to frequencies where one spin state has a much higher photon absorption probability than the other. In this way we can address the resonances of the two spin states composing our sample independently, as we do with our state-selective imaging. Besides imaging the two states independently we can exploit this splitting of the atomic resonances to selectively address the two spin states with resonant or near-resonant light for introducing spin-selective dissipative perturbations in our system. This can be easily achieved by our experimental setup for the realization of spin-dependent optical potentials since we just need to lock our laser source in the vicinity of the atomic resonances. Further, we can exploit the DMD for shaping the intensity profile of our laser beam for engineering dissipative local spin-selective perturbations, such as a spin filter [73, 76].
In the following we show how we can exploit our experimental setup for obtaining local spin-selective photon absorption in our system.

4.1.1 Absorption spectra of non-interacting Zeeman states

To perform a first test of our experimental setup we lock our laser source to the atomic resonances of the $|1\rangle$ and $|3\rangle$ spin states and we find that we are able to selectively address each state with resonant light. This allows us to test the reliability of our offset-lock and paves the way for the realization of spin-selective dissipative perturbations.
While the most interesting physical phenomena that we can investigate are related to the presence of interactions between atoms in different spin states, we perform our experiments on a $|1\rangle - |3\rangle$ non-interacting Fermi gas. This allows us to exclude any mutual interaction between the two spin states so that the only effects we have to take into account are those introduced by our spin-selective perturbations. We prepare the non interacting Fermi gas through the experimental protocol described in section 1.5, obtaining a sample composed by $\sim 10^5$ atom per spin state at $T/T_F \simeq 0.1$.
By looking at the trend of the scattering rates of our system for different light polarization (see Fig. 3.3) we find that the most well-suited choice for selectively addressing the resonances of the spin states in our setup is to use σ^--polarized light. This is because the offset-lock setup is designed and optimized to control the frequency of our laser source in the range between the D_1 and D_2 lines, while addressing the spin states' resonances using π or σ^+ polarized light requires to work with light that is blue-detuned with respect to the D_2 transition. However, we have seen that in our setup we cannot shine a fully σ^--polarized beam on the atomic cloud because of geometric reasons. Since our laser light propagates perpendicularly to the quantization axis it is impossible to have a pure σ^- circular polarization, nonetheless we can work with light that has

a non-zero σ^- component. In fact, we can decompose the polarization state of electromagnetic radiation in the basis of $\{\pi, \sigma^+, \sigma^-\}$ polarization states and we can write:

$$\hat{\epsilon} = a\,\hat{\epsilon}_\pi + b\,\hat{\epsilon}_{\sigma^+} + c\,\hat{\epsilon}_{\sigma^-} \tag{4.1}$$

where $\hat{\epsilon}$ is the light polarization and a, b, c are the coefficients for the state decomposition. In our experimental setup the quantization axis is given by the Feshbach magnetic field direction which is vertical. Therefore a linear vertical polarization corresponds to pure π-polarized light ($a = 1$, $b = c = 0$). On the other hand, a linear horizontal polarization is orthogonal to such state, thus corresponding to an equal mixture of σ^+ and σ^--polarized light ($a = 0$, $b = c = 1/2$). While this horizontal polarization state is not completely σ^-, it is the state with the highest σ^- component achievable in our setup. Further, it is the polarization state that we use for imaging our atomic cloud from the horizontal direction, so we already have a setup that is capable of shining horizontally polarized light on the atomic cloud from the horizontal direction. For these reasons, we test our spin-selective dissipative perturbations using light with linear, horizontal polarization.

To know the target frequency at which to lock our laser, we have to compute the scattering rate of our spin states for light with horizontal polarization. This can be done using expression 3.11 for the multi-level scattering rate. We take into account the horizontal polarization by equally dividing the light intensity into σ^+ and σ^- components and summing the computed scattering rates for the two components. We report the scattering rates of states $|1\rangle$ and $|3\rangle$ at 572 G for horizontal polarization in Fig. 4.1, computed for an arbitrary intensity of 0.1 mW/cm^2. The peaks that are present in the scattering rate of state $|1\rangle$ and not in that of state $|3\rangle$ are related to transitions allowed by the $|m_J = 1/2\rangle$ component of state $|1\rangle$, which is absent in $|3\rangle$. As mentioned before, these peaks would be ideal for the implementation of spin-selective dissipative perturbations. However, to access the corresponding frequencies, which are either blue-detuned with respect to the D_2 line or red-detuned with respect to the D_1, we need to slightly adapt our experimental setup. While this can be done quite easily we restrain from doing so since the scope of this work is to realize spin-dependent potentials using frequencies that are between the two atomic resonances. Moreover, we can realize equally selective dissipative effects also using the ~ -1 GHz detuned resonances of the two spin states. Therefore we resolve to produce our spin-selective perturbations by tuning our laser frequency around such resonances.

At first we avoid using the DMD horizontal setup described in section 3.3.3 and we instead plug the optical fiber coming from the offset-lock table in the fiber mount of the horizontal imaging light. In this way we take advantage of the imaging setup and our beam is already aligned to the atomic cloud as well as already having the desired horizontal polarization.

We shine our spin-selective laser beam on the whole non-interacting cloud trapped in the harmonic confinement provided by the optical dipole trap. Since we want to selectively address the spin states using resonant and near-resonant light we need to work with light pulses that are long enough to produce a detectable effect while being short enough to observe a difference between the addressed and unaddressed states. In fact, shining near-resonant light for a long time would eventually result in all the atoms in both spin states escaping the optical confinement due to photon absorption. For this reason we tune our experimental parameters finding the optimal conditions to be 15 μs long light pulses with 5.5 mW power. For our Gaussian beam this corresponds to an intensity of 5 mW/cm^2, resulting in a saturation parameter $I/I_s \simeq 2$ [19]. To monitor our sample we employ a double imaging technique that allows us to independently

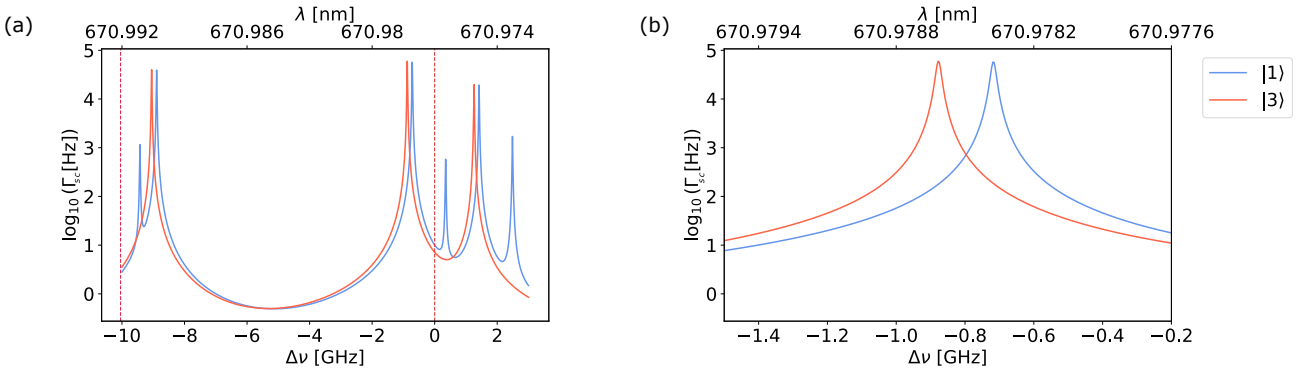

Figure 4.1: Scattering rates of spin states for horizontally-polarized light. (a) Full profile of the scattering rate for frequencies between the D-lines of ^{6}Li. (b) Zoom in the relevant region for the generation of spin-selective perturbations. Data are plotted as a function of the detuning $\Delta\nu$ from the zero field D_2 transition (lower x-axis) and of the light wavelength (upper x-axis). We report the D_1 and D_2 transitions as dashed red lines. The light intensity is arbitrarily set to $I = 0.1$ mW/cm^2, corresponding to a saturation parameter $I/I_s = 0.04$.

but almost simultaneously image both the spin states of our Fermi gas. By shining a light pulse and looking at the number of atoms remaining in each spin state we can estimate the dissipative effect of the spin-selective perturbations. Since all atoms that escape the trap are lost due to the light pulse, by comparing the relative losses of the two spin states we can demonstrate the spin-selectivity of our perturbation.

We tune and stabilize the frequency of our laser source in the vicinity of the atomic resonances using the offset-lock setup. By changing the target offset we are able to scan the frequency region around the resonances and effectively measure the absorption spectrum of the two spin states. We report such spectra in Fig. 4.2 (a), where the peaks corresponding to the resonances of the two spin states are clearly visible. When we lock our laser to the resonant frequency of one spin state the atoms in such state get blasted by the light due to photon absorption and escape the harmonic confinement, thus resulting in a decrease of the state's population. We observe that resonantly blasting atoms in one spin state does not significantly affect the population of the other state. While this happens mainly because we are working in a non interacting system, it demonstrates that it is possible to use our experimental setup for introducing spin-selective losses in our system.

Measuring the temperature of one of the two spin states, namely of state $|1\rangle$, we see that it does not change unless we address such state with resonant light (Fig. 4.2 (b)). While this may be a hint that our spin-selective perturbation do not introduce heating in our sample, drawing conclusions from a temperature measurement in a non-interacting system is not trivial. Due to the absence of interactions, atoms cannot, in principle, thermalize after being perturbed by our laser pulse, which opens the question concerning the meaning of the temperature we measure. A possible answer to such question could be that we measure the temperature of the atoms that do not absorb any photon and remain trapped in our confining potential. If every atom that absorbs a photon escapes the trap without interacting with any other atom it seems reasonable that the temperature of the atoms remaining in the trap is not affected by our external perturbation. If this is the case, the only conclusion we can draw from this temperature measurement

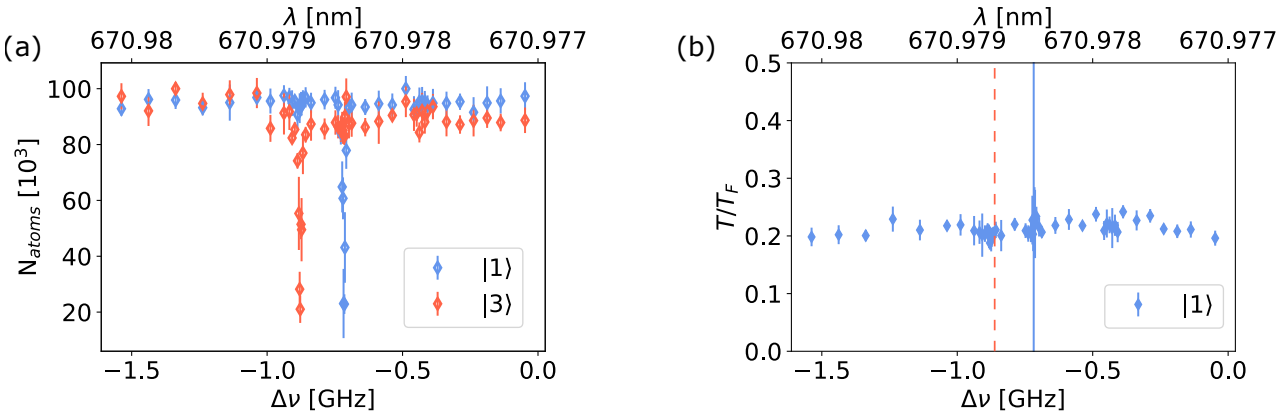

Figure 4.2: Spin-selective atomic losses. (a) Absorption spectra of the $|1\rangle - |3\rangle$ spin states. Scanning the frequency of our laser source we can selectively remove atoms in one spin state from our system. (b) Temperature of atoms in state $|1\rangle$. Here $T_F \simeq 450$ nK. The dashed red indicates the state $|3\rangle$ resonant frequency. Data are plotted as a function of the detuning from the zero field D_2 line and of the laser wavelength. Each point corresponds to the mean of at least 5 experimental data and error bars are computed as the standard deviation of such data.

is that it demonstrates that we are working with a truly non-interacting system. For investigating the heating effects caused by our spin-selective perturbations we should instead perform measurements on interacting systems. Moreover, we could compare out T/T_F measurements with measurements of the cloud's size, that should increase with increasing temperature. As of now we describe our spin-selective dissipative perturbations focusing only on the induced losses. By comparing the measured resonances with the computed scattering rates we find that they are indeed found at the expected frequencies. Further, we can obtain the resonances' width by fitting them with a Lorentzian function. In particular, we find the Full Width at Half Maximum (FWHM) to be 8.4(5) MHz and 10(1) MHz for state $|1\rangle$ and $|3\rangle$ respectively. These values are compatible with the 6 MHz natural linewidth of the D_2 transition [19] and the observation of such relatively narrow resonances demonstrates the reliability of our offset-lock setup.
To completely describe the width of our resonances we also consider the power broadening caused by working with non-negligible saturation parameter. In fact, the width of an absorption line is not simply the natural linewidth of the transition Γ but it is broadened by an amount related to the ratio between the light's and the saturation intensity (2.54 mW/cm^2 for the D_2 transition). Therefore, we can write the power broadened linewidth as $\Gamma_{PB} = \Gamma\sqrt{1 + I/I_s}$. By measuring the experimental width of our resonances and inverting this relation we obtain the saturation parameter I/I_s associated to our intensity, finding $I/I_s = 1.1(1)$ and $I/I_s = 2.1(3)$ for $|1\rangle$ and $|3\rangle$ respectively. The expected saturation parameter for our experimental condition is 2, therefore the value found for state $|3\rangle$ is in excellent agreement with our expectations while we can ascribe the discrepancy for state $|1\rangle$ to acceptable experimental errors. We report the Lorentzian fit of our experimental data and we compare them to the expected scattering rate in Fig. 4.3 (a).
We further investigate the role of power broadening by exploring the behavior of only one resonance as we change the light intensity and the pulse duration. We find that the resonance

gets both deeper and wider as we increase the power and the duration of the pulse, resulting in higher atom losses. Fitting the resonances for different experimental conditions we find that doubling the light power does indeed result in a resonance that is a factor $\sqrt{2}$ wider, while the depth of the peak is not affected by a change in power as long as light is shone on the cloud for a sufficiently long time. On the other hand, reducing the pulse time while keeping the intensity fixed results in reducing both the width and the depth of the resonances due to inferior losses in the atomic sample. We report the behavior of the resonance of state $|1\rangle$ to the change of experimental parameters in Fig. 4.3 (b).
Looking at the expected number of photons absorbed by a single atom for one of our light pulses (Fig. 4.3 (b), bottom) we see that this number is surprisingly high. We therefore suspect that we either overestimate the magnitude of the photon absorption probability or that an atom needs to absorb many photons before it has sufficient energy to escape the trapping potential. Due to this uncertainty, we prefer to evaluate the losses introduced by our laser light by directly looking at experimental values instead of trying to estimate them from our scattering rate calculations.

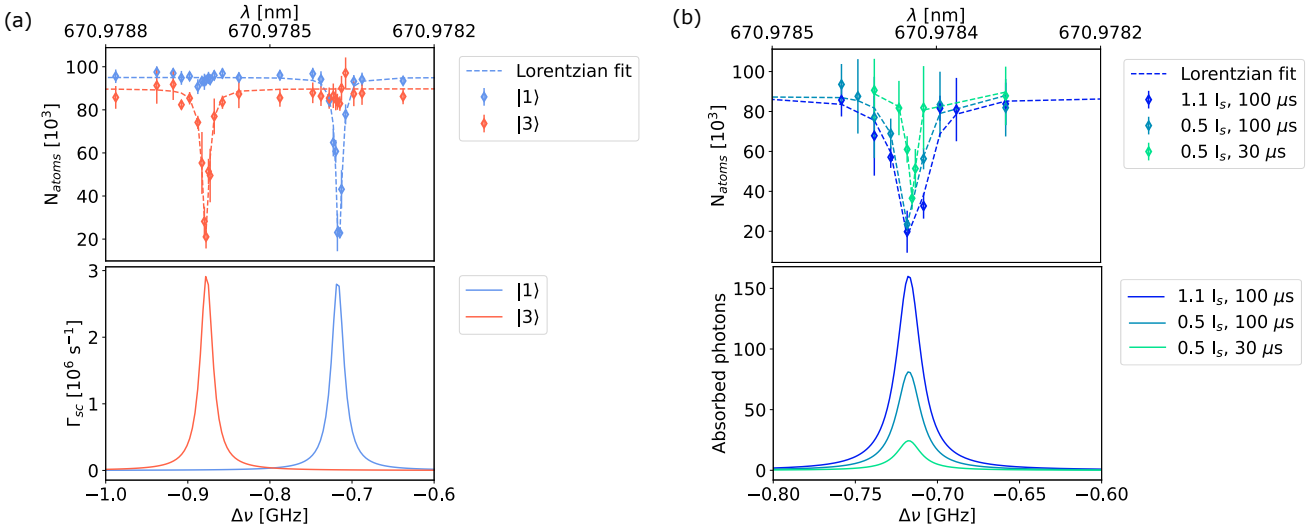

Figure 4.3: Resonances fitting and scattering probability. (a) Atomic resonances of the $|1\rangle$ and $|3\rangle$ spin states. Top: experimental data (diamonds) and Lorentzian fit (dashed line). Bottom: scattering rate computations for our experimental parameters. (b) Resonance of state $|1\rangle$ for different experimental conditions. Top: experimental data and Lorentzian fit. Bottom: Plot of the expected number of photons absorbed by each atom during the light pulse. Each experimental point is obtained by the mean of at least 5 data. Error bars are standard deviation of such values.

4.1.2 Local dissipative perturbations

The spin-selective losses induced by our perturbations can be exploited for imbalancing the spin population of the sample by shining resonant laser light on the whole atomic cloud as we have shown in the previous section. Such imbalanced system provides a very good platform for investigating the physics of impurities and quasiparticles in a Fermi system. In particular, it has

been shown that impurities formed by particles of the minority component can be dressed by particles in the other state, which act as a bath, and form a so-called *polaron* quasiparticle [70, 71]. A globally imbalanced system for the investigation of such fermionic quasiparticles can be obtained by driving radiofrequency transitions between internal states which does not require all the tools we developed for selectively addressing spin states with laser light. However, our experimental setup allows us to shape the intensity profile of the laser light and it opens up the possibility to produce locally imbalanced fermionic systems. To produce such local imbalance we need to induce local spin-selective losses in our sample. This can be achieved by locking our laser source to the resonance of one spin state and exploiting the DMD optical setup for shaping the profile of our laser beam. We can use the DMD as a light mask to simply reduce the waist of the Gaussian beam that we shine on the atoms, so that it covers only a defined region of the sample, or we can use it to produce more complicated shapes or patterns including barriers and arrays of focused beams.

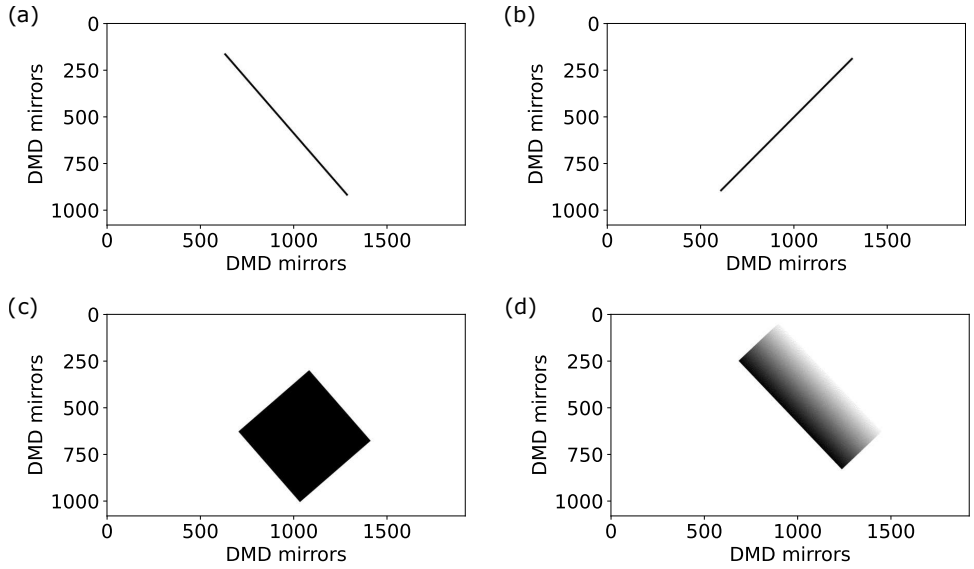

Figure 4.4: Examples of images displayed on the DMD screen. (a)-(b) Narrow barriers aligned parallel or perpendicularly to the main axis of the atomic cloud. (c) Homogeneous square: the reflected beam retains its Gaussian profile with a smaller waist. (d) Gradient-like pattern: the grayscale profile is obtained with a dithering procedure of the black and white image. All displayed images are tilted and centered in order to be aligned to the atomic sample.

Before shining our tailored laser beam on the atomic cloud we need to make sure that it is actually well aligned with the cloud itself. To do end we use a couple of irises to align the beam reflected by the DMD to the horizontal imaging beam, that we know is impinging on the atomic cloud. After doing this, we center the beam on the atomic sample by shining short resonant light pulses and looking at the density profile of the atomic cloud. When the DMD displays a completely black image the mirrors are all in the ON direction and the reflected beam has a Gaussian shape with the largest possible waist, so that it covers the whole atomic cloud. Therefore, we roughly center our beam using its maximum waist to verify that all the cloud is covered by the beam. Then we reduce the beam waist by displaying progressively smaller black

squares on the DMD screen, so that we can center our beam more precisely by looking at the density depleted region in the atomic cloud. We find the tilting angle between the atomic cloud and the DMD screen by shaping the beam profile as a thin rectangle around 10 DMD mirrors wide. Shining this light barrier on the atoms results in depleting the atomic density in a narrow region. By looking at the tilting angle between such region and the axes of our cloud we find the tilting angle of the DMD. Knowing such angle we can easily compensate for it by displaying opportunely tilted images on the DMD screen, so that the image projected on the atomic cloud has the desired orientation.
Once the laser beam is correctly centered on the atomic cloud, we proceed to a finer focusing of our imaging system. To do so, we again shine short pulses of resonant light shaped as a narrow barrier and we look at the atom losses in the region of the cloud that is covered by such barrier, expecting them to be the highest when the beam is focused on the atomic cloud. By using a T-stage mount for moving the $f = 75$ mm lens in our setup we can maximize such losses and focus our DMD-tailored beam on the atomic cloud. We report in Fig.4.4 (a-c) a few examples of the images displayed on the DMD screen during this alignment and focusing procedure. In Fig.4.4 (d) we instead report a gradient-like image that we use for giving a linear profile to our laser beam (see next section).
Once the optical setup is focuse,d we can use the DMD for arbitrarily shaping the intensity profile of our laser beam to realize local spin-dependent perturbations. In order to produce a locally spin-imbalanced system we display a small black square on the DMD screen so that the reflected beam covers only a defined region of the atomic cloud. By locking our laser source close to the resonance of one state and shining a short light pulse we are able to remove the atoms in that state from the region of interest without having a strong effect on the other component. In Fig. 4.5 we show the differential and local effect on the two states of a light pulse locked to the resonance of state $|1\rangle$. While we test our setup using intensity profiles such as simple squares

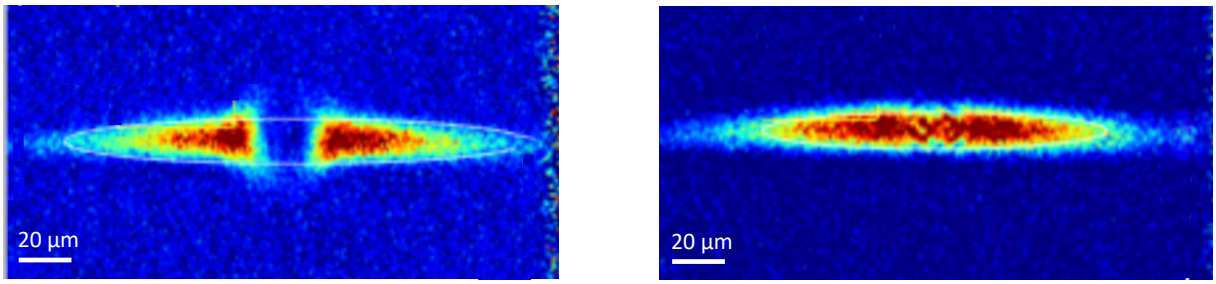

Figure 4.5: Local spin-selective blast. By shining a tailored laser beam that is resonant for state $|1\rangle$ we are able to locally remove atoms in $|1\rangle$ from our sample without having a strong effect on atoms in $|3\rangle$. We report experimental images of the density profile of atoms in $|1\rangle$ (left) and $|3\rangle$ (right) after shining our spin-selective beam.

or rectangles, we are in principle able to arbitrarily shape such intensity profile introducing features as small as a few micrometers. This may allow to realize spin filtering barriers or channels similarly to what was done in Refs. [73, 76].
Further, by appropriately tuning the experimental parameters at our disposal we can introduce local dissipative perturbations which may be tuned to selectively heat one spin component without removing it from the trapping potential. This will probably require to employ either

non-resonant or lower intensity light in order to reduce the absorption probability. Further, we may need to increase the depth of our optical dipole trap in order to keep the atoms trapped after they absorb a photon. Introducing a local spin-selective heating in an interacting spin-mixture may allow us to investigate heat transport in a quantum environment. Moreover this could allow us to address the many open questions regarding the coupled transport of heat and spin, paving the way for the quantum simulation of spin caloritronics [39, 48, 50].

4.2 Arbitrarily tailored optical potentials

In the previous discussion about the realization of local dissipative perturbations we focused on how we can use the DMD for shaping the intensity profile of a laser beam for shining it over finite regions of the atomic sample. To do this we just need to display simple patterns on the DMD screen, such as squares or rectangles with the desired size and orientation. However the realization of arbitrarily DMD-tailored optical potentials requires a more complicated shaping of the intensity profile. In fact, the spatial shape of an optical potential is directly proportional to the light's intensity profile: $V_{dip}(\mathbf{r}) \propto I(\mathbf{r})$. Therefore to arbitrarily tailor an optical potential it is necessary to have a high degree of control on the profile of the laser light.
As each DMD micromirror can be in either the ON or OFF state, the DMD is able to display arbitrary black and white patterns but it cannot display any grayscale image. Conversely, the potentials we want to realize will often have a continuous and smooth profile. Further, as we have already mentioned, since the laser beam impinging on the DMD has a Gaussian profile, this profile is retained after the beam is reflect by the DMD. The resulting profile of the optical potential is then given by the convolution between a Gaussian and the light mask provided by the DMD pattern. This particular effect prevents the straightforward realization of uniform potentials with the DMD. In fact, displaying a uniform black image on the DMD screen results in the DMD acting as a simple mirror so that the tailored optical potential will not be spatially homogeneous but Gaussian.
These two limitations seem to severely hinder the realization of arbitrarily tailored optical potentials using a DMD. However, it is possible to obtain a grayscale image by displaying a dithered pattern on the DMD screen where the density of ON mirrors reproduces the smooth profile of the target image as in Fig. 4.4 (d). Combining such dithering with an iris positioned at the focal point of one of the lenses of the imaging setup allows to effectively smooth the profile of the optical potentials, thus allowing to realize a continuous potential with a black and white pattern. To solve the issue related to the Gaussian profile of the laser light we use a particular feedback program that is capable of compensate for it and that we will describe in the following.

4.2.1 Intensity profile feedback program

In order to realize arbitrarily shaped optical potentials and to remove the Gaussian component from the profile of the DMD-reflected beam we exploit a feedback program that has been developed in Refs. [27, 33]. We briefly describe such program, referring to [27, 33] for a more detailed treatment.
The idea behind the feedback program is that, since the light profile on the atomic plane is not the same as in the image displayed on the DMD screen, it is possible to change such image in order to have the desired profile on the atoms. The two main reasons for differences between

the target and the actual image are the Gaussian profile of the laser beam and the presence of defects in the imaging setup such as dark regions in the light pattern created by flecks of dust on the optical elements. The feedback program corrects these two issues, realizing on the atomic plane a light pattern that is closer to the desired one.
The program operates as follows: the DMD mirrors are arranged in order to reproduce the target image and a picture of the resulting image is taken by the CCD camera in our experimental setup. This picture is then compared to the target image and the DMD mirrors are rearranged in order to compensate for discrepancies. To compare the target image to the actual one we compute the pixel-by-pixel error matrix, i.e. the difference between the two images for each pixel. This error matrix is then summed to the previous DMD image, weighted by a proportional and an integral coefficient, to obtain a new image. The new image is sent to the DMD and the process is iterated as long as the difference between the acquired and the target images is not sufficiently low.
Before being able to feedback our images we have to calibrate the DMD screen into the CCD, since the two have a different pixel number and orientation. This is achieved by a calibration routine where we find the affine transform that maps the DMD screen into the CCD by taking a CCD picture of the DMD screen displaying three dots at known relative positions.
Using our feedback program we can realize arbitrarily shaped potentials, including spatially homogeneous optical potentials. In this case, the rearrangement fo the DMD mirrors is such that the intensity is lowered near the peak of the Gaussian while it is maximized close to its tails, thus realizing a uniform intensity profile. Since with the DMD we cannot increase the light intensity on the edges of the beam, the reflected profile, while being spatially uniform has a lower intensity because it is bounded by the intensity in the tails of the Gaussian beam.
We focus on giving a linear shape to the intensity profile of our laser beam since this allows us to imprint either a uniform force or a uniform velocity to the atomic sample. We report the results of the feedback program of such an intensity profile in Fig. 4.6.

4.2.2 Linear optical gradients

The optical dipole force acting on a particle subjected to an optical potential is proportional to the gradient of the light intensity. In fact, being $V_{dip}(\mathbf{r}) \propto I(\mathbf{r})$, the dipole force is given by:

$$\mathbf{F}_{dip}(\mathbf{r}) = -\nabla V_{dip}(\mathbf{r}) \propto -\nabla I(\mathbf{r}). \tag{4.2}$$

Considering a one-dimensional situation for simplicity, a linear potential does indeed result in a spatially constant force: $V(x) \propto x \rightarrow F(x) = const.$ Therefore, a linearly-shaped optical potential allows to manipulate an atomic sample with a force that is homogeneous over the whole beam area.
To realize such potential we use the DMD to give a profile to the light intensity that is linear along one direction, so that $I(x) = I_0\, x$, while it is constant along the other one. To reproduce this continuous profile on the DMD screen we again use a dithered image in which the density of ON pixels is linear along the desired direction. Using our feedback program we are able to correct for the Gaussian profile of the beam and we can successfully give a gradient-like shape to our laser beam. We report an example of such linear profile before and after applying our feedback procedure in Fig. 4.6.
Since such linearly-shaped beam results in a constant force over the whole beam area, we can

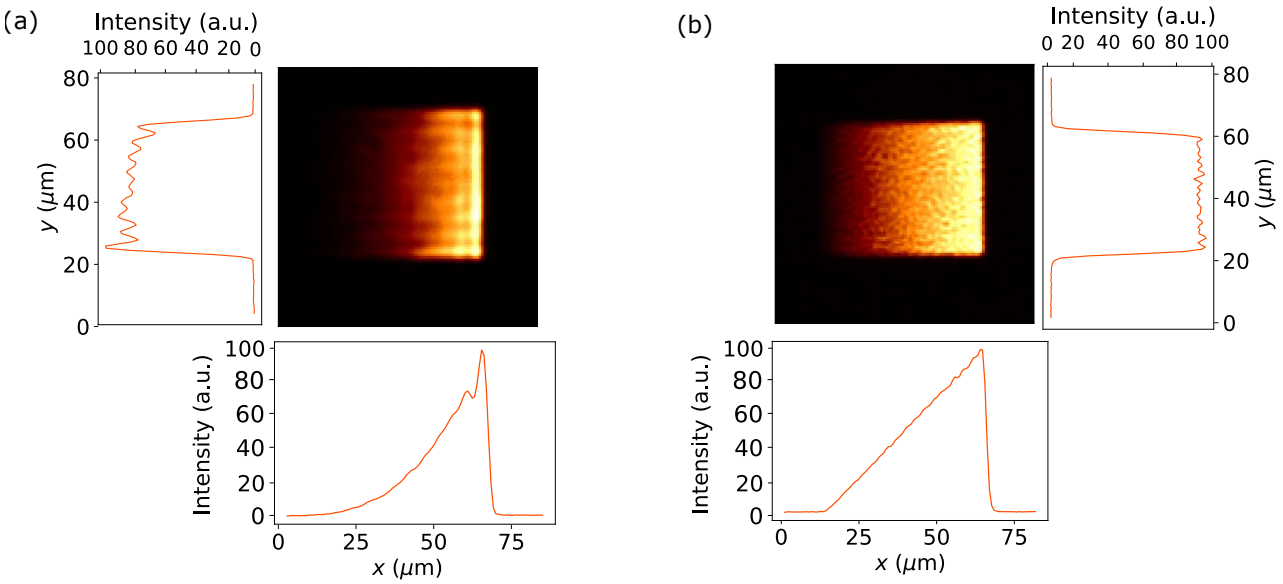

Figure 4.6: Linearly-shaped light intensity profile and feedback program. We show a CCD picture of a DMD-shaped laser beam and its intensity profile integrated along the vertical and horizontal directions. Without the feedback program (a) the DMD-shaped beam retains part of its Gaussian profile which can removed by our feedback procedure (b).

use it give a uniform acceleration to our atomic sample, thus generating an atomic current which is the fundamental building block of the whole field of atomtronics [7]. Further, the degree of control offered by tailored optical potentials allows to produce atomic currents along different directions and in different geometries, including the realization of circulating currents in not-simply-connected geometries [77–80]. We report the light intensity profile necessary for generating a linear current or a circulating current in an ultracold atomic gas in Fig. 4.7.
Following a classical description, a liner potential result in a constant force F over the whole beam area. This force imprints a momentum change to each atom, which can be quantified by simply using Newton's second law:

$$\Delta p = \int_{t_0}^{t_1} F_{dip}(t)dt = F_{dip}\,\Delta t \tag{4.3}$$

where p is the atomic momentum and $\Delta t = t_0 - t_1$ is the time interval for which we shine the laser beam on the sample. This very simple picture shows that we can generate an atomic current by shining a linearly-shaped optical potential on the atomic cloud for short time intervals. However, as we will see in the following, this classical treatment is not suited to describe the generation of an atomic current using a linear optical potential, as an appropriate description should take into account the profile of the quantum mechanical phase of the atomic wavefunction. Nonetheless, the experimental procedure required to generate controlled currents in ultracold atomic gases is the same. If the optical potential used for imprinting the current is spin-dependent or spin-selective then different currents will be generated for atoms in different spin states. Considering two states only, the resulting effect will thus be a spin current:

$$J_s = J_\uparrow - J_\downarrow \tag{4.4}$$

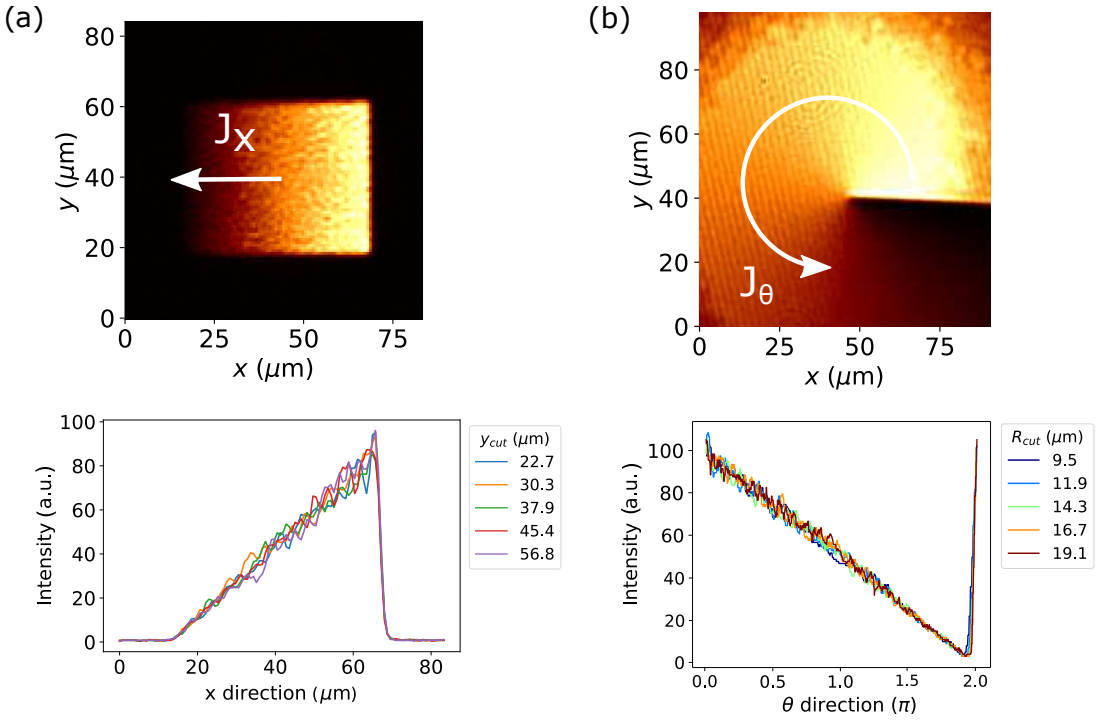

Figure 4.7: CCD pictures of the light intensity profiles for generating a linear (a) or circulating (b) current in an atomic sample. When light is blue-detuned atoms are repelled by the peak of the intensity and the induced current flows "down" the intensity slope. On the bottom we report different cuts of the feedbacked intensity profile.

where $J_\uparrow$ and $J_\downarrow$ are the atomic currents of the $|\uparrow\rangle$ and $|\downarrow\rangle$ spin states respectively.

4.3 Optical Stern-Gerlach experiment

One of the most direct way of introducing and observing a spin-dependent effect in an ultracold atoms experiment is to perform a so-called optical Stern-Gerlach (OSG) experiment [81]. The name originates from the analogy between this kind of experiments and the 1929 Stern-Gerlach experiment which demonstrated the quantization of angular momentum [82]. That particular experiment involved sending a beam of silver atoms through an inhomogeneous magnetic field and observing their deflection by letting them struck a detector. Due to the interaction between the atomic angular momentum and the inhomogeneous magnetic field, each atom composing the beam is affected by a force that deflects its trajectory. The breakthrough observation of the Stern-Gerlach experiment was that the atomic beam was split in two smaller beams, thus demonstrating the quantization of angular momentum. Considering an inhomogeneous magnetic field $B(z)$ directed along the vertical direction z and an atomic beam propagating perpendicularly to it, we have that the vertical component of the force acting on each atom is:

$$F_z = g_J \, \mu_B \, m_J \, \frac{dB}{dz} \tag{4.5}$$

where g_J is the Landè g-factor, μ_B is Bohr's magneton and m_J is the atomic angular momentum projection along the quantization axis, here defined by the magnetic field direction z. If we consider atoms with $l = 0$ and $J = s = 1/2$, as was the case of Stern and Gerlach's silver atoms, we have that only two values of m_J are possible, namely $m_J = m_s = \pm 1/2$. In this case the atomic beam is split into two beams, each composed by atoms in only one spin state.
From the discussion above we can see that in a Stern-Gerlach experiment it is possible to use an magnetic field gradient for introducing a spin-dependent force on an atomic beam so that atoms are deflected in different directions depending on their spin. Analogously, we can use a spin-dependent optical potential for applying a spin-dependent force on an atomic cloud and separate atoms in different spin states. In this case the z-component of the force acting on each atom will be given by:

$$F_z = -\frac{\alpha_i}{2\epsilon_0 c}\frac{dI}{dz} \tag{4.6}$$

where α_i is the real part of the polarizability for atoms in spin state $|i\rangle$ and I is the light's intensity. While this spin-dependent can be applied when the atomic gas is confined by an optical dipole trap, doing so results in introducing center of mass oscillations inside the trapping potential which add to the experimental shot-to-shot fluctuations of the trap position, needlessly increasing the complexity of the experiment. Therefore, in an optical Stern-Gerlach experiment the spin-dependent beam is shone on the atoms after they are released from the trapping potential. When atoms are released in the absence of any external perturbation they fall under the action of gravity and expand in the so-called *time of flight expansion*. By shining a spin-dependent optical potential on the falling atoms it is possible to give a differential acceleration to the different spin states which deflects their trajectory. In strong analogy to the traditional, magnetic Stern-Gerlach an optical Stern-Gerlach experiment allows to split the trajectories of moving atoms depending on their spin quantum number, exploiting a spin-dependent optical potential instead of the angular momentum-magnetic field interaction to do so.
Usually the OSG technique is used for measuring the population of different spin states in ultracold atoms experiments working with atomic species such as ytterbium where it is rather complicated to image different spin states independently due to a very small Zeeman splitting [52, 83, 84]. Since in such experiments the different spin states cannot be resolved energetically, the OSG is used to resolve them through a spatial separation. Conversely, the larger energy splittings of the Zeeman states of ^{6}Li atoms allow us to image the two spin states independently so that we don't need an OSG to resolve them. In this work, we perform the optical Stern-Gerlach experiment to demonstrate that we can realize both spin-dependent and spin-selective optical potentials, since the OSG is a powerful tool for revealing differential effects of forces acting on atomic spin states.
For reproducing the magnetic field gradient of the classic Stern-Gerlach, we shape the intensity profile of the optical potentials as a vertical gradient. This results in a spin-dependent force that is also aligned to the vertical direction, thus being parallel to gravity. Therefore, as atoms fall through the laser beam, they feel a vertical force that is added to the gravitational force. Appropriately tuning the frequency of our laser source we can produce opposite forces for the two spin states or a selective force that affects only one of them. By imaging our cloud from the horizontal direction we can detect the center of mass position of the two spin states at different times to follow their trajectory. Comparing the trajectories of the two states in presence or in absence of the OSG beam we are able to demonstrate that we can successfully realize both

spin-dependent and spin-selective optical potentials. We report sketches of both the magnetic and optical Stern-Gerlach experiments in Fig. 4.8.

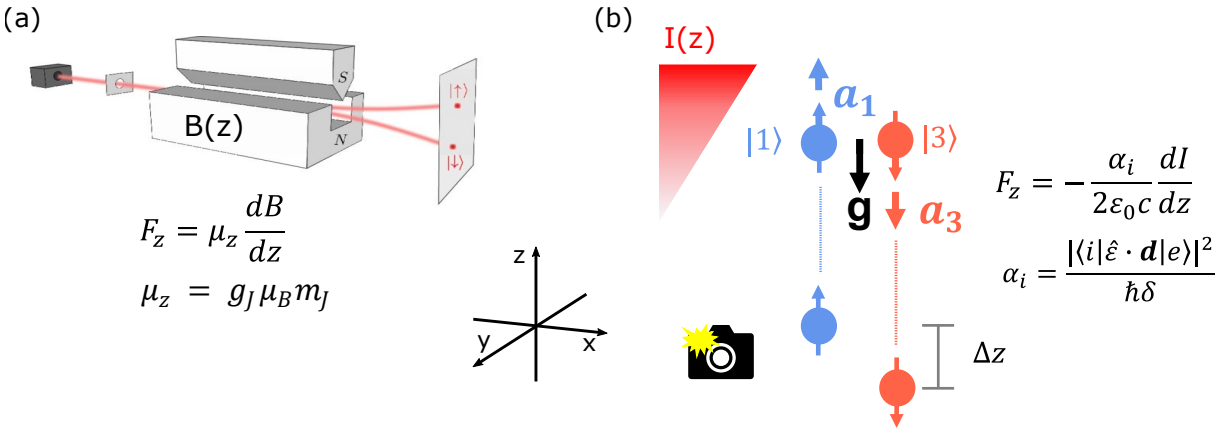

Figure 4.8: Magnetic and optical Stern-Gerlach experiments. (a) Magnetic Stern-Gerlach: a magnetic field gradient produces a spin-dependent force that deflects the trajectory of atoms traveling as a collimated beam depending on their spin. (b) Optical Stern-Gerlach: a linear spin-dependent optical potential obtained by a gradient-shaped laser beam gives a differential acceleration to the two spin states composing our system. Observing the trajectory of the two components as they fall in time of flight allows to reveal the spin-dependent effect of the optical potential.

4.3.1 Optical Stern-Gerlach setup

We perform all the optical Stern-Gerlach experiments on a $|1\rangle - |3\rangle$ non-interacting Fermi gas exploiting the 572 G zero crossing of the scattering length between such states. As in the case of the spin-selective blast, we work in a non-interacting system in order to prevent any physical phenomena related to the presence of interactions from affecting our observations.
In order to characterize the spin-dependent optical potentials we observe their effect on the center of mass trajectories of the two spin states. To do this, we compare their trajectory to what it would be in absence of any external perturbation. To find the unperturbed trajectory we simply prepare our system confined in the optical dipole trap, we release the trapping potential and we measure the center of mass position of the two states as they fall. Since we do not introduce any spin-dependent effect, the trajectories of the two states are exactly the same. We image the falling cloud from the horizontal direction and we fit the atomic density profile with a Gaussian distribution so that we can find the z coordinate of the center of mass of the system. We can follow this trajectory up to around 10 ms of time of flight, after which the atoms' motion and expansion brings them out of the objective of our horizontal camera.
Measuring the unperturbed free fall of the two states also allows us to calibrate the magnification of the horizontal imaging setup. In fact, the center of mass position measured with the camera is obtained in units of 16 μm wide camera pixels. However, one micrometer in the camera picture does not correspond to one micrometer in real space since the system is magnified by the telescope described in section 3.3.3. This telescope is composed by two lenses in the $f + f$ configuration, resulting in an expected magnification factor of 6.67. To measure the actual

magnification we can fit the free fall trajectory of our sample with the simple quadratic function $z_{px} = \frac{1}{2} a_{px}\, t^2$, where z_{px} is the center of mass position measured in camera pixels, t is the time at which the image is taken and a_{px} is the acceleration in pixels/s^2. Since we know that the atoms are falling under the action of gravity alone, we can assume this acceleration to be proportional to the gravitational acceleration $g = -9.81$ m/s^2, with a coefficient that is the calibration parameter for converting camera pixels into micrometers. By writing $a_{px}\, L = g$ we can find the coefficient L, which rescales pixels into μm. Knowing the size of each camera pixel (16 μm) we can then divide $L/(16\,\mu\text{m})$ to find the actual magnification of our telescope. We find a magnification of 6.87, so that each camera pixel corresponds to 2.33 μm on the atomic cloud. In this way we both calibrate the imaging setup magnification and find the factor for converting our data from camera pixels to micrometers.

After calibrating the imaging magnification and observing the unperturbed motion of the two spin states we can apply the spin-dependent optical potentials on them and investigate how such potentials affect their trajectories. To apply a vertical and spatially uniform force we shape our laser beam as a vertical gradient with a size sufficiently large to cover nearly all of the atomic cloud. We use our feedback protocol to produce such linearly-shaped laser beam and we find that we can obtain a $\simeq 200\,\mu$m wide gradient that is capable of covering most of the atomic sample. As we report in Fig. 4.9 (a), we efficiently shape our beam along the vertical direction, corresponding to the linear profile of the gradient, while we have issues in obtaining a homogeneous profile along the horizontal direction due to the size of our target image. In fact, the width of the target gradient is comparable to the diameter of our laser beam, so that the feedback program does not have to remove only a portion of the Gaussian profile but it really needs to reshape the whole Gaussian beam. The combined requirements of having a linear profile along the z direction and an homogeneous one along x are rather difficult to satisfy and our program is able to only partially remove the Gaussian profile along the x direction. Since for the OSG experiment we are mainly concerned about the vertical direction, we are satisfied with this result and we employ the intensity profile reported in Fig. 4.9 (a). We align the DMD so that the gradient covers most of the atomic cloud, taking care that the step of the gradient, corresponding to the maximum of the intensity, is positioned above the cloud. In this way we avoid that the atoms get strongly repelled or attracted by the steep increase of light intensity in correspondence of the maximum of the gradient profile. We report a sketch of the relative position between the light gradient and the atomic cloud in figure 4.9 (b).

When we shine the OSG beam on the trapped atoms, the two spin states feel a spin-dependent force that can be directed either downwards or upwards. Being affected by such force, the atoms will start moving inside the optical trap along the vertical direction, giving rise to in-trap oscillations. Releasing the atoms from the trap as they oscillate inside it results in them starting their motion with non-trivial initial velocities and positions which greatly complicates the experiment. For this reason, we first release the optical trap and only then we shine the OSG beam. By shining the beam less than 1 ms after releasing the trap we are able to apply the spin-dependent force to our atoms as they fall through the OSG beam and avoid issues related to in-trap oscillations. Since the atoms fall under the action of gravity, and we are not able to imprint accelerations greater than g, we do not need to pulse our laser light as atoms naturally pass through the beam as they fall.

We lock the frequency of our laser source to a value where we expect a spin-dependent effect and we see that the center of mass position of the two spin states after a fixed time of flight

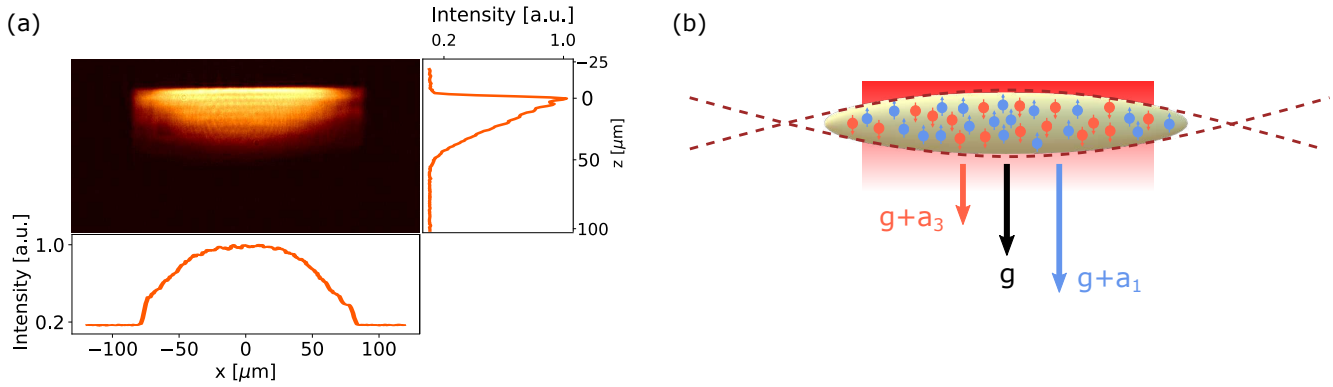

Figure 4.9: Experimental realization of the optical Stern-Gerlach. (a) CCD picture of the intensity profile of the linearly-shaped laser beam. (b) Sketch of the relative position between the OSG beam and the trapped gas. The atomic cloud is trapped in a cigar-shaped optical dipole trap (dark red dashed lines) and the OSG beam is aligned in order to cover most of the cloud. When the spin-dependent beam is applied on the atoms and the trap is turned off the two spin states fall with a differential acceleration.

is indeed different. Moreover, we see that by increasing the light intensity we can enhance this difference. However, doing this results also in an increase of the width of the atomic density distribution. This is due to the atoms absorbing photons from the laser beam and acquiring a higher kinetic energy. Since we want to investigate the conservative effects of the spin-dependent optical potentials we optimize the intensity of our laser beam by finding a compromise between evident differential effects on the two states and low photon absorption. We find that this is achieved for 350 μW power of the laser beam.

4.3.2 Differential trajectories of spin states

We scan the frequency of our laser source and we look at the trajectories of our spin states as a function of the detuning from the D_2 line. Comparing the trajectories to the unperturbed one we can reveal the effect of our spin-dependent forces. To quantitatively analyze our data we proceed along two parallel directions: we fit the experimental trajectory of the spin states using a simple equation of motion and we compare them to the expected trajectories obtained with a simulation.
The equation of motion of a uniformly accelerating object is given by:

$$z(t) = \frac{1}{2} a\, t^2 + v_0\, t + z_0 \tag{4.7}$$

where t is time, a is the uniform acceleration while v_0 and z_0 are the initial velocity and position respectively. Considering our falling sample, its center of mass acceleration is given by the contribution of both gravity and the optical potentials. However, our system is not uniformly accelerating since the optical force is acting on the atoms only as long as they are passing through the laser beam, while as soon as they exit the beam area they are only affected by gravitational acceleration. The simplest analysis we can make is to neglect this situation and fit the whole trajectory of the spin states with Eq. 4.7 imposing $v_0 = z_0 = 0$. In this way we can

find the mean acceleration of the spin states across the whole trajectory. By subtracting g from this value we can have a rough estimate of the differential acceleration given to the spin states by the spin-dependent potential. We find that we can obtain a differential acceleration between the spin state of the order of 10% g, i.e. $|a_{|1\rangle} - a_{|3\rangle}| \simeq 1$ m/s^2. Scanning the frequency of our laser source we can realize both spin-dependent and and spin-selective forces: $a_{|3\rangle/|1\rangle} = g \pm 0.5$ m/s^2 (spin-dependent) or $a_{|1\rangle/|3\rangle} \simeq g$ and $a_{|3\rangle/|1\rangle} \simeq g \pm 1$ m/s^2 (spin-selective).

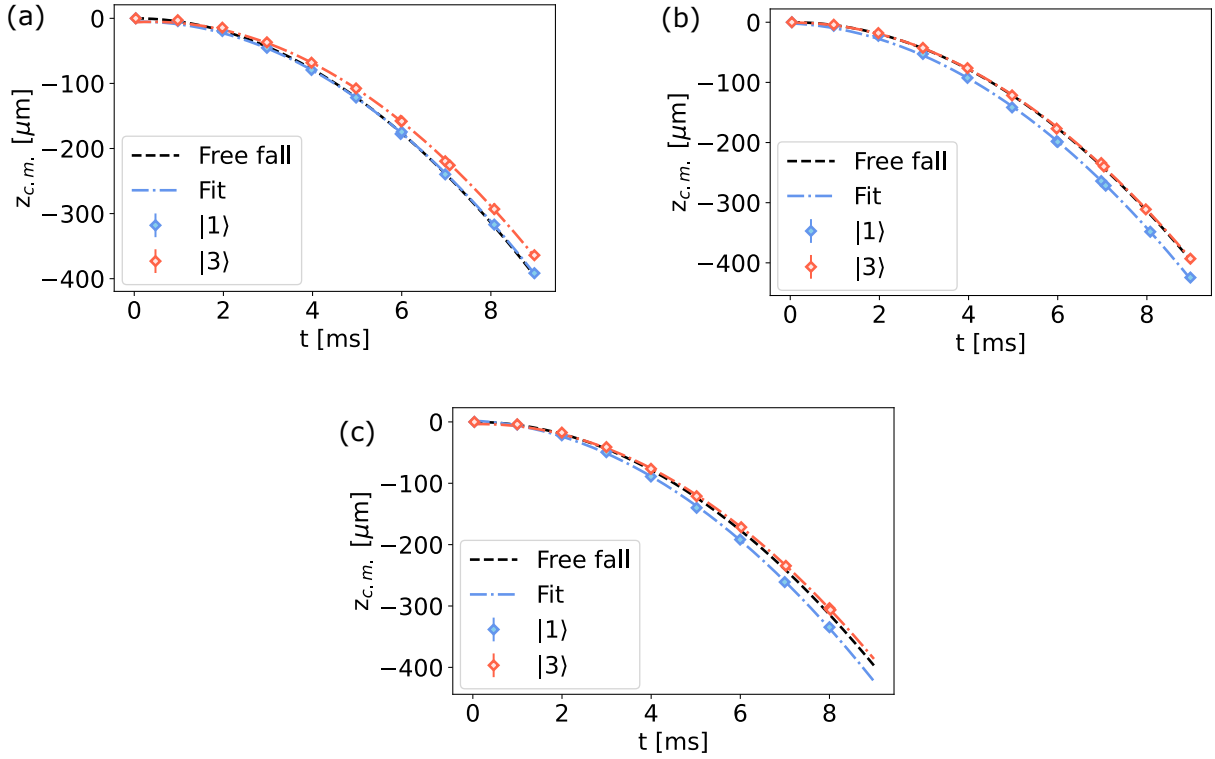

Figure 4.10: Spin state trajectories and fit. (a) $|3\rangle$-selective force: atoms in $|3\rangle$ are affected by an optical force pointing upwards, while atoms in $|1\rangle$ do not feel any force other than gravity. (b) $|1\rangle$-selective force: atoms in $|1\rangle$ are affected by an optical force pointing downwards, while atoms in $|3\rangle$ do not feel any force other than gravity. (c) Opposite force: atoms in $|3\rangle$ are affected by a force pointing upwards, while atoms in $|1\rangle$ are affected by a force pointing downwards. We report experimental points as diamonds and fitting curves as dot-dashed lines. Each point corresponds to the mean value of at least five experimental shots. Errorbars are the standard deviation of such values.

To have a more reliable estimate of the atoms' acceleration we can consider separately the region covered by the beam and the region where atoms fall under the action of gravity alone. Comparing the measured trajectories and the size of the light gradient we estimate that atoms exit the beam area after a $\simeq$3 ms fall. After such time, the equation of motion describing their fall is 4.7 with fixed $a = g$ and with x_0 and v_0 depending on the motion of the atoms during the 3 ms in which they fall inside the OSG beam. Therefore, we neglect the data corresponding to $t < 3$ ms and we fit the trajectories with $z(t) = \frac{1}{2} g\, t^2 + v_0\, t + z_0$, finding both v_0 and z_0. We can then obtain the acceleration due to the optical potential as: $a = v_0/(3\, ms) - g$. We again

find that the differential acceleration of the two states is of the order of 10% g, in agreement with our first estimations. We report the experimental trajectories of the spin states and their fit obtained with the above procedure in Fig 4.10.
Through the optical Stern-Gerlach experiment we demonstrate that our setup is capable of realizing both spin-dependent and spin-selective optical potentials. However, we find that the laser frequencies that allow us to realize such potentials are not consistent with the ones predicted by the polarizability computations presented in section 3.1. In particular, we find that the experimental frequencies corresponding to the polarizabilities' zero crossings are shifted by $\simeq 700$ MHz with respect to our expectations. The expected detuning from the D_2 line for having a zero crossing in the state $|3\rangle$ polarizability is $\simeq -6.3$ GHz. However, our experimental findings indicate that a spin-selective potential for state $|1\rangle$, i.e. $V_{|3\rangle} = 0$, is obtained for a $\simeq -5.6$ GHz detuning. We find that the spacing between the zero crossings of the two states is $\simeq 160$ MHz, which is consistent with our expectations. We suspect this $\simeq 700$ MHz shift to be due to the light polarization being not completely π. In fact, while our theoretical computations assume perfectly π-polarized light, this may not be true in the real experiment. As we have seen in section 3.3, we can tune the light polarization with a couple of $\lambda/2 - \lambda/4$ waveplates and, monitoring it with a polarimeter, we can set the waveplates' angle in order to have a linear vertical polarization. However, it is difficult to achieve 100% linear polarization and this polarization is measured with respect to the polarimeter's internal vertical axis which may be slightly different from the quantization axis defined by the Feshbach magnetic field. We therefore conclude that our assumption of perfect π polarization may not describe the experimental configuration accurately. To account for this, we tune the polarization state in our theoretical computations until they match the experimental data and we find that the observed light shifts are consistent with a light polarization that has a 85% π component and a 15% σ^+ component. We ascribe this experimental deviation from a perfect π polarization to both the tilting between the polarimeter's and the quantization axis and to the effect of optical elements which may slightly affect the beam polarization. We report a comparison between the theoretical and experimental detunings for realizing spin-selective and spin-dependent potentials in Table 4.1.

	$a_{\|1\rangle}$ [m/s^2]	$a_{\|3\rangle}$ [m/s^2]	$\Delta\nu_{exp}$ [GHz]	$\Delta\nu_{\pi}$ [GHz]	$\Delta\nu_{mix}$ [GHz]
Selective $\|1\rangle$:	-1.1(1)	0.1(1)	-5.618(2)	-6.326	- 5.614
Opposite:	-1.0(2)	0.5(1)	-5.573(2)	-6.240	- 5.549
Selective $\|3\rangle$:	0.3(1)	1.3(1)	-5.478(2)	-6.146	- 5.468

Table 4.1: Detunings comparison. We report the experimental detunings ($\Delta\nu_{exp}$) and the theoretical detunings computed for both π ($\Delta\nu_{\pi}$) and mixed ($\Delta\nu_{mix}$) light polarization necessary for realizing spin-selective and opposite optical potentials. Accelerations are measured with the fitting procedure described above.

To confirm this hypothesis and validate our polarizability calculations we simulate the trajectories of the spin states in the optical Stern-Gerlach experiment and we compare them to our experimental observations. We consider the one-dimensional motion of a single point, corresponding to the center of mass of our sample, falling along the z axis with non-uniform acceleration. We divide its trajectory into steps separated by time intervals $\Delta t = 2\,\mu$s. Given the

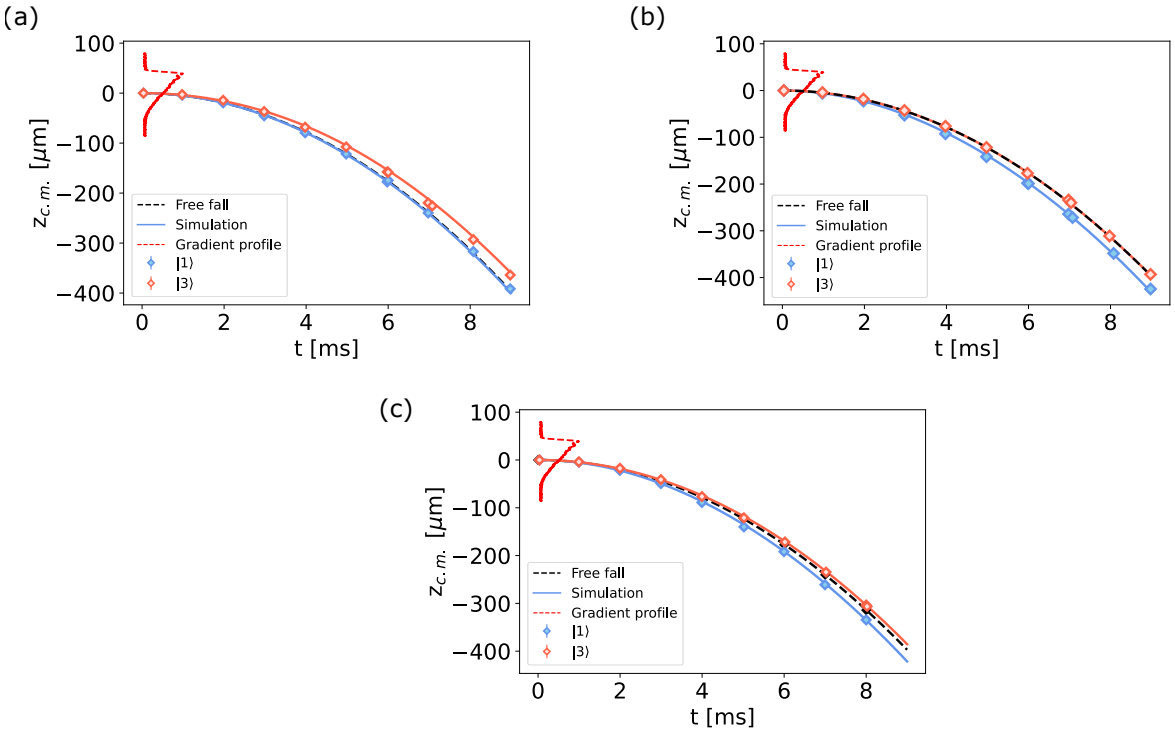

Figure 4.11: Optical Stern-Gerlach simulations. We report a comparison between the OSG experimental data (diamonds) and simulations (continuous lines) for the cases of: (a) selective potential for state $|3\rangle$, (b) selective potential for state $|1\rangle$, (c) opposite potentials. We report the shape of the gradient-shaped laser beam as a dashed red line. Experimental data are reported as diamonds and correspond to the mean value of seven experimental shots. Errorbars are standard deviation of such values.

center of mass position and velocity at step i, we compute them at the following step as:

$$\begin{aligned} z_{i+1} &= z_i + v_i \Delta t + \frac{1}{2} a_i \Delta t^2 \\ v_{i+1} &= v_i + a_i \Delta t \end{aligned} \tag{4.8}$$

where a_i is the acceleration at step i. Diving the trajectory into steps allows us to account for the spatially varying acceleration. For all the steps corresponding to a position where atoms are outside the region covered by the beam, we set $a_i = g$ as atoms feel only the gravitational acceleration. Conversely, when they travel inside the OSG beam we have to consider the acceleration caused by the optical force. To account for this acceleration we compute the optical force considering the intensity profile of our laser beam. We obtain such profile integrating the CCD picture of the OSG beam along the horizontal direction as in Fig. 4.9 (a) and we use it for computing the spatially varying optical potential acting on our sample. A pixel-by-pixel numerical derivative of the optical potential profile allows us to find the spatial dependence of the resulting force, which is mostly constant over the beam area but presents some inevitable fluctuations. From this spatially varying force we obtain a position-dependent acceleration that we insert in our simulation as $a_i = g + a_{opt}(z_i)$, where $a_{opt}(z_i)$ is the acceleration induced by

the optical force when the atoms' center of mass is in z_i. We find very good agreement between our simulations and the experimental data and we report a comparison between them Fig. 4.11. We observe a little discrepancy between experiment and simulations for the case of a potential selective only for state $|3\rangle$. In this case the optical force is directed opposite to gravity as expected, while the measured acceleration is smaller than the one predicted by the simulations.

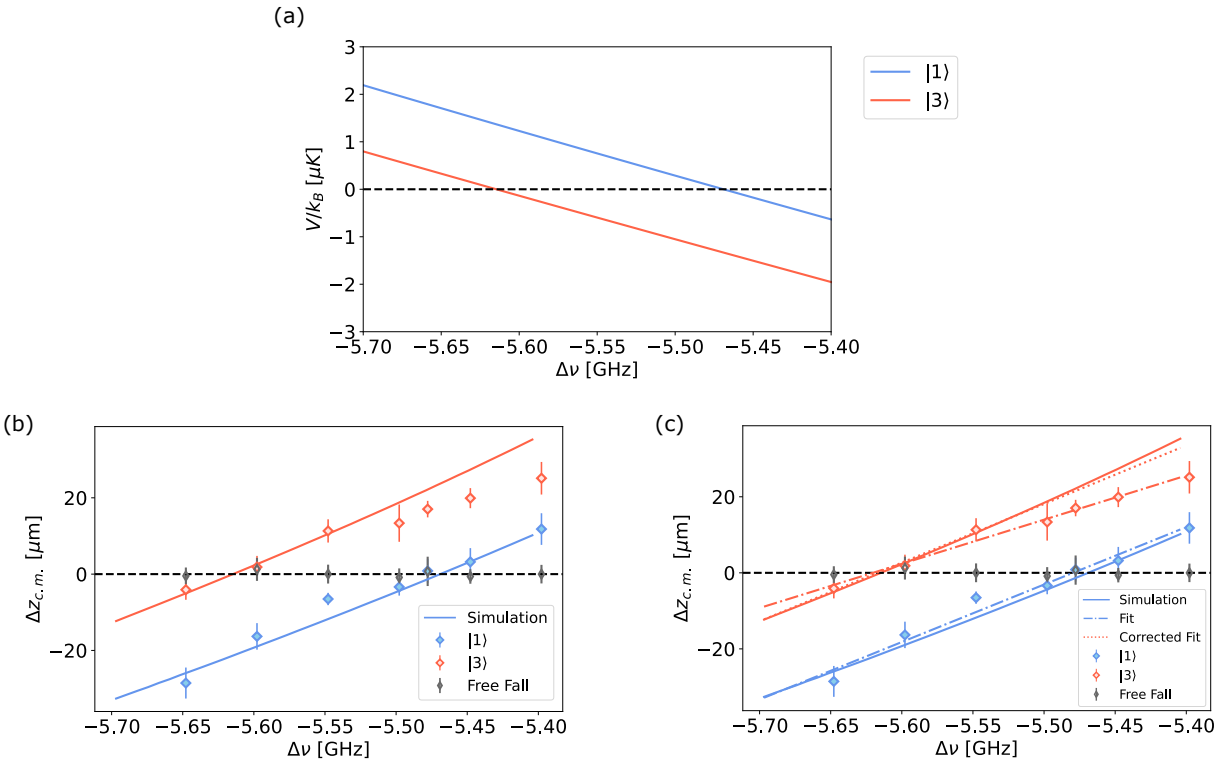

Figure 4.12: Frequency dependence of the optical potentials. (a) Theoretical light shifts of $|1\rangle$ and $|3\rangle$ spin states in the experimentally explored frequency range. Light shifts are reported in units of the Boltzmann constant k_B and as a function of the detuning from the D_2 line. (b) Center of mass position after 6 ms time of flight as a function of the light detuning. y-axis is the deviation from the unperturbed value, corresponding to the free fall in absence of the OSG beam. Experimental points (diamonds) are the mean value of al least five experimental shots, while errorbars are standard deviation. Simulation data (continuous line) are obtained with the above procedure. (c) Linear fit (dashed-dotted line) of the experimental data. We report a corrected fit taking into account only the first three points of state $|3\rangle$ as a dotted red line.

As a final measurement we investigate the relative position of the two states' center of mass at fixed time (6 ms) as a function of the laser source frequency. We report our findings in Fig. 4.12. Comparing the experimental results with the simulations we find good agreement between them, however we again observe a discrepancy for the data of state $|3\rangle$. We see that such deviation is enhanced when atoms in $|3\rangle$ feel a larger force, resulting in a larger displacement from the unperturbed trajectory. Conversely, for the frequency range we explore, we do not see any discrepancy for atoms in $|1\rangle$. This allows us to ascribe such deviation to the fact that, for the frequencies where we observe a discrepancy, atoms in $|3\rangle$ are attracted by the laser beam and

thus spend more time inside it. This results in higher photon absorption, which is not considered in our simulations and which may affect the center of mass position after the atoms exit the beam area. Further a more attractive potential results in a longer time passed by the atoms in the beam area and in a higher scattering probability, which may explain why discrepancies seem to become more relevant as the attractive force increases. On the other hand, atoms in $|1\rangle$ are mostly repelled by the laser light and they pass through the beam rather quickly, thus being less affected by scattering phenomena. This reasoning may explain the simulation-experiment discrepancy we see for state $|3\rangle$ data in correspondence of the most attractive optical forces.
To qualitatively investigate the agreement between the experimental data and the simulations we fit their slope across the zero crossings approximating their profile to a line. We find good agreement for state $|1\rangle$ as we find the slope of the simulation data to be 0.1459(6) μm/MHz compared to 0.15(1) μm/MHz for the experimental data. On the other hand, we find a coefficient of 0.162(8) μm/MHz and 0.116(7) μm/MHz for the state $|3\rangle$ simulation and data. Since we suspect that our simulations cannot properly describe the points corresponding to the largest negative potentials we fit again the slope of $|3\rangle$, considering only the three points closest to the zero crossing, corresponding to the lowest forces. This fit (Fig. 4.12 (c), red dotted line) results in a slope of 0.15(2) μm/MHz which is compatible with our experimental observations.
In conclusion through the optical Stern-Gerlach experiment we demonstrate that our experimental setup is capable of realizing both spin-selective and spin-dependent optical potentials. Further, by comparing the simulated trajectories to the experimental data we validate our multilevel polarizabilities computation.

4.4 Outlook: spin currents

While the optical Stern-Gerlach is a powerful tool for revealing the spin-dependent nature of our optical potentials, their implementation opens up much more interesting possibilities. In particular, we can exploit spin-dependent optical potentials for generating spin currents in an atomic sample.
As we have seen in Chapter 2, a spin current can be generated by spatially separating spin states with a magnetic field gradient and then letting atoms with different spin move towards one another [56, 57]. However, generating spin currents through spin-dependent optical potentials allows to achieve a much greater control over time and length scales and to decouple the current generation from the external magnetic field. In particular, optical potentials allow to control the magnitude of the spin currents by changing their shape or the time for which they are applied to the atomic cloud.
To detect a spin current in our sample we take advantage of our state-selective imaging. Since we can selectively image atoms in different spin states, we can describe a spin current by simply monitoring their relative motion. If we apply a spin-selective potential we will detect a motion of the center of mass of atoms in the addressed state while the atoms in the other state remain stationary. Such selective potentials result then in a coupled spin and mass current as the center of mass of the whole cloud is displaced by the motion of atoms in only one spin state. On the other hand, an opposite motion of the two states results in a spin current with negligible mass transport. In the atomtronics picture [7], a mass current of neutral atoms is analogous to the charge current in solid-state electronic circuits. In such systems it is usually impossible to separate the spin and charge degrees of freedom, a notable exception being the spin-charge

separation in the one-dimensional Tomonaga-Luttinger liquid [54], so that electric and spin current are always coupled. In this context optical potentials are a versatile tool that allow to induce either coupled or decoupled spin and mass currents.

4.4.1 Phase imprinting method

From a classical perspective, the simplest way of generating a current through an optical potential is to give it a linear shape, so that the atoms are affected by a uniform force. As we have previously mentioned, shining this linear potential on the atomic sample for a short time results in an effective "kick" to the atoms, which acquire a momentum and thus a velocity due to the externally applied force. This velocity results in an atomic current which can survive for longer or shorter times depending on the nature of the system. While this classical treatment can indeed offer a simple picture of the origin of optically-induced atomic currents, it is not sufficient to accurately describe the generation of currents through optical potentials in ultracold atomic gases.
To properly describe how we can excited a current in an atomic sample with a linear optical potential we need to consider the quantum nature of the system. An ultracold atomic gas can be described by a many-body wavefunction $\psi(t)$ whose time evolution is given by:

$$\psi(\mathbf{x}, t) = e^{-\frac{i}{\hbar}(H_0+V(\mathbf{x}))t}\psi(\mathbf{x}, 0) \tag{4.9}$$

where H_0 is the Hamiltonian describing the unperturbed system and $V(x)$ is the applied optical potential. If at $t = 0$ the potential is pulsed on the atomic cloud for a time τ that is much shorter than the typical timescales of the system, given by the frequencies of the trapping potential and by the chemical potential, we can neglect H_0. Therefore, the wavefunction at time τ will be

$$\psi(\mathbf{x}, \tau) = e^{-\frac{i}{\hbar}V(\mathbf{x})\,\tau}\psi(\mathbf{x}, 0). \tag{4.10}$$

Hence in the limit of small τ, the external potential will simply add a phase $\varphi(\mathbf{x}) = -V(\mathbf{x})\,\tau/\hbar$ to the system's wave function.
Considering a one dimensional system, the probability current operator for the i-th particle composing our sample is:

$$J_i(x, t) = -\frac{i\hbar}{2m}\left(\psi_i^*(x, t)\frac{\partial\psi_i(x, t)}{\partial x} - \psi_i(x, t)\frac{\partial\psi_i^*(x, t)}{\partial x}\right). \tag{4.11}$$

Inserting the time-evolved wavefunction 4.10 and summing over all the N particles composing the system we have that the total probability current is:

$$J(x, t) = \frac{1}{m}\rho(x, 0)\frac{\partial V(x)}{\partial x}\tau \tag{4.12}$$

where $\rho(x, t) = \sum_{i=1}^{N}|\psi_i(x, t)|^2$ is the numerical particle density. If the external potential is a linearly shaped optical potential then $\frac{\partial V(x)}{\partial x} = \beta = const.$ and the resulting current will just be:

$$J(x, t) = \frac{1}{m}\rho(x, 0)\beta\tau. \tag{4.13}$$

Such current is imprinted by manipulating the phase profile of our sample using an external potential. This method, appropriately named *phase imprinting method* [80, 85], is one of the

most promising techniques for inducing controlled currents in ultracold atomic gases. In fact by controlling both the imprinting time τ and the slope β, which can be tuned by changing the intensity of the laser beam, it is possible to control the magnitude of the induced currents. In the case of spin-dependent or spin-selective optical potentials each spin state will develop a current:

$$J_{\uparrow\downarrow} = \frac{1}{m}\rho_{\uparrow\downarrow}(x,0)\beta_{\uparrow\downarrow}\tau. \tag{4.14}$$

The resulting spin current will just be given by $J_s = J_\uparrow - J_\downarrow$. In the case of spin-selective potentials one of the two states will not develop any current so that the total spin current will coincide with the mass current of the addressed state. Further, expression 4.14 allows to highlight how the density of atoms in each spin state $\rho_{\uparrow\downarrow}(x,0)$ is a parameter that affects the magnitude of the spin current and that we can tune by locally imbalancing the spin population with resonant light.

With our experimental setup we can obtain imprinting times τ arbitrarily long and as short as a few microseconds. Since typical timescales of our system range from hundreds of microseconds to tens of milliseconds we can easily access the phase imprinting regime. Therefore, to imprint a spin-current in our sample we just need to give a gradient shape to the intensity profile of our laser beam as in the optical Stern-Gerlach experiment and pulse it on the atomic cloud finding the optimal configuration for generating a measurable spin current while keeping the scattering rate contained. Oppositely to the OSG case, for the generation of spin currents we want to align the gradient horizontally so that the current develops on the long axis of our cigar shaped trap. Once the current is generated we can detect it by measuring the relative motion of the two spin states' centers of mass inside the trapping potential. From very preliminary observations we find that it may be good to eliminate experimental shot-to-shot fluctuations of the trap center in order to increase the signal-to-noise ratio. This can be achieved by using the green DMD that we have in our experimental setup to add a stable confining potential to the crossed dipole trap. This can be for example done by adding solid walls near the edges of the dipole trap as in [22, 23], where this allowed to increase the signal to noise ratio by suppressing the shot-to-shot fluctuations in the center of mass position. The combined used of both our DMDs and of the $\mathrm{TEM}_{(0,1)}$ beam (see Chapter 1) may open exciting possibilities for investigating spin transport in different geometries or in presence of repulsive obstacle inside the sample.

Conclusions and perspectives

In this work we designed and implemented an experimental setup for the realization of tailored spin-dependent optical potentials which are a promising tool for the investigation of spin transport and spin excitations in ultracold Fermi gases.
We showed that the Zeeman levels of ^{6}Li atoms in magnetic fields display strongly state-dependent polarizabilities for laser light with frequencies between the atomic D_1 and D_2 lines. We found that by finely tuning the frequency and the polarization of a laser source it is possible to realize both state-dependent and state-selective optical potentials with tolerable photon scattering rates. Since the considered Zeeman states differ by their nuclear spin, such potentials allow to manipulate atoms with different spin in a differential way.
We developed an experimental setup for realizing such spin-selective potentials. First we implemented an offset-lock setup capable of setting and stabilizing the frequency of a 671 nm laser source. In particular, the offset-lock scheme allows us to lock the laser source to a frequency offset from a reference laser locked to an atomic transition. We achieve frequency control and stabilization in a range from 0 to - 6.5 GHz detuning from the D_2 atomic line, which is sufficient for the realization of both spin-dependent and spin-selective potentials.
After developing the offset-lock setup necessary for controlling the frequency of the laser source, we focused on tailoring the spatial profile of the optical potentials. To this end, we designed and built an optical setup for shaping the intensity profile a laser beam using a Digital Micromirror Device. This setup also allows us to focus such tailored light on the atomic sample after a demagnification process, taking advantage of the pre-existent horizontal imaging setup. Thanks to appropriate tools we achieve control on the light polarization and intensity.
We performed a first test of our setup by selectively addressing atoms in different spin states with resonant light. To avoid coping with physical phenomena related to the presence of interactions, all our tests are performed over a non-interacting Fermi gas composed by ^{6}Li atoms in the lowest and third-lowest Zeeman states. We demonstrated that we can resonantly and selectively address atoms in one state by looking at the population of the two spin states after shining them with light resonant with only one state. Performing the same experiment with a DMD-shaped beam allowed us to show that our setup is capable of producing local spin-selective dissipative perturbations with a spatial resolution of the order of a few micrometers.
We then tested and characterized the spin-dependent potentials by performing an optical Stern-Gerlach experiment. By applying a spin-dependent force and observing the differential trajectories of the two spin states we demonstrated that the setup we developed is capable of realizing both spin-dependent and spin-selective optical potentials. Comparing the trajectories of the two spin states in the optical Stern-Gerlach experiment to the trajectories of unperturbed falling atoms we have been able to quantify the effects of the optical forces we can produce.

We found that we can give a differential acceleration to our falling spin states of the order of 1 m/s^2 with almost negligible photon scattering. Finally, we validated the multi-level polarizability computations by comparing the experimental trajectories to simulations based on such theoretical predictions.
In conclusion, in this work we implemented a new setup for the realization of spin-selective tailored optical potentials. This setup allows to differentially and selectively manipulate nuclear spin states of ^{6}Li atoms with a new level of control over time and length scales. Moreover, combining the spin-dependent potentials with the other optical potentials at our disposal we can control the shape of the atomic sample and investigate spin transport phenomena in different geometries.
The simplest geometry we can investigate is that of the atoms confined in the cigar-shaped optical dipole trap that we use for their evaporative cooling. As this trap has a harmonic profile, shining a linear spin-dependent optical potential directed along the main axis of the trap allows to induce relative oscillations between the two spin components. Such oscillatory spin current can be detected by looking at the relative position of the two spin states' centers of mass (Fig. C1 (a). Considering the case of a spin-selective potential, while in the non-interacting case the unaddressed state is expected to remain stationary, the presence of interactions between spin states leads to the unaddressed atoms being dragged by the moving component. As we have seen in Chapter 2, this spin drag can be both dissipative and non-dissipative [68] depending on the considered timescales. Thanks to our versatile spin-selective optical potentials we are in principle able to access both short and long timescale and investigate these spin drag regimes.
A possible limitation to our experiments is given by the limited imprinting time that we can employ for inducing a spin current with contained scattering rate ($\Gamma_{sc} \leq 10^3$ photons/s). With an imprinting time of the order of 80 μs and a saturation parameter $I/I_s \simeq 400$ we expect to observe the center of mass of the addressed state oscillate with an amplitude smaller than 10 μm. Thus, at least for weakly interacting non paired systems, the dragged component will oscillate with an even smaller amplitude, possibly below one micrometer. While we can in principle detect such small amplitude oscillations thanks to our high-resolution imaging setup, this three dimensional (3D) geometry may not be ideal for the investigation of spin drag in all interaction regimes
On the other hand, spin drag is expected to be a enhanced in two-dimensional (2D) geometries. Further, most of modern-day solid state quantum devices are based on low-dimensions nanostructures, motivating the great interest in the quantum simulation of one (1D) or 2D systems. We can achieve a 2D or quasi-2D geometry by squeezing the atomic gas along the vertical direction using a repulsive TEM$_{(0,1)}$ beam [27]. Exploiting both the TEM$_{(0,1)}$ and the DMD-tailored repulsive potentials we can also obtain oblate homogeneous degenerate gases, as in [24]. We can therefore combine both the spin-selective and the repulsive optical potentials to investigate spin transport in 2D or quasi-2D, homogeneous or non-homogeneous, systems. (Fig. C1 (b)).
Moreover, the tailored repulsive optical potentials allow us to trapping our atomic sample in even more exotic geometries. In Fig. C1 (c-d) we report sketches of two geometries that we can realize in our experimental setup. By realizing a squeezed toroidal system (Fig. C1 (c)) we could investigate circulating spin currents, in a geometry similar to that of superconducting squids. However, to introduce a spin current in such geometry it is necessary to adapt our optical setup for shining the spin-dependent potentials along the vertical direction. With our current setup we could instead investigate spin conductance through narrow channels, which we can realize

using again the tailored repulsive optical potentials provided by our green DMD setup (Fig. C1 (d)).

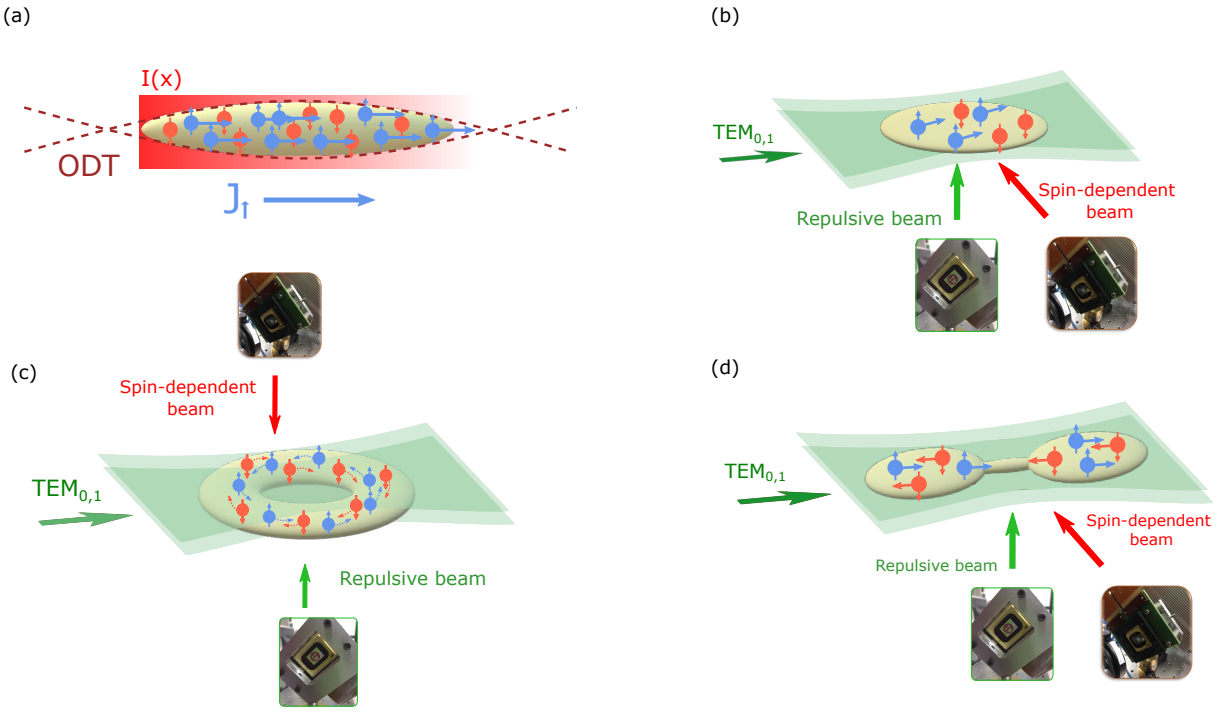

Figure C1: Spin transport experiments in different geometries. (a) Generation of spin currents in the optical dipole trap obtained by two crossed IR beams. (b) Spin transport in an oblate homogeneous system obtained by combining the vertical squeezing provided by the $TEM_{(0,1)}$ beam and DMD-tailored repulsive potentials. (c) Toroidal geometry for the investigation of circulating spin currents. (d) Spin transport between terminals. The confining potential and the narrow channel can be obtained with the tailored repulsive potentials.

Once the geometry of our system is set, we can further exploit different optical potentials to investigate spin transport in many experimental conditions. The easiest, but nonetheless interesting, situation would be to generate a spin current through either spin-selective or spin-dependent potentials and simply investigate the properties of such current, looking for hints of spin drag or other phenomena related to correlations between spin states in relative motion. However, we can also exploit the green DMD to introduce a set of repulsive obstacles in our system and investigate how they affect its spin transport properties. In Fig. C2 (a, c) we sketch two possible experiments for the investigation of spin currents in presence of a repulsive barrier (Fig. C2 (a)) or of a pattern of either ordered or disordered repulsive obstacles. In such cases, the spin manipulation is provided by the spin-dependent potentials and the DMD-shaped green light has a repulsive effect on both the spin states, which could be exploited for investigating the robustness of spin currents.
Conversely, we can use the green repulsive potential for imprinting an equal current to both spin states and use the spin-selective potentials for introducing spin-selective obstacles that may act as spin filters as in Fig. C2 (b). In this case we will need to take into account the dissipative effects introduced by the close-detuned light of the spin-selective potentials.

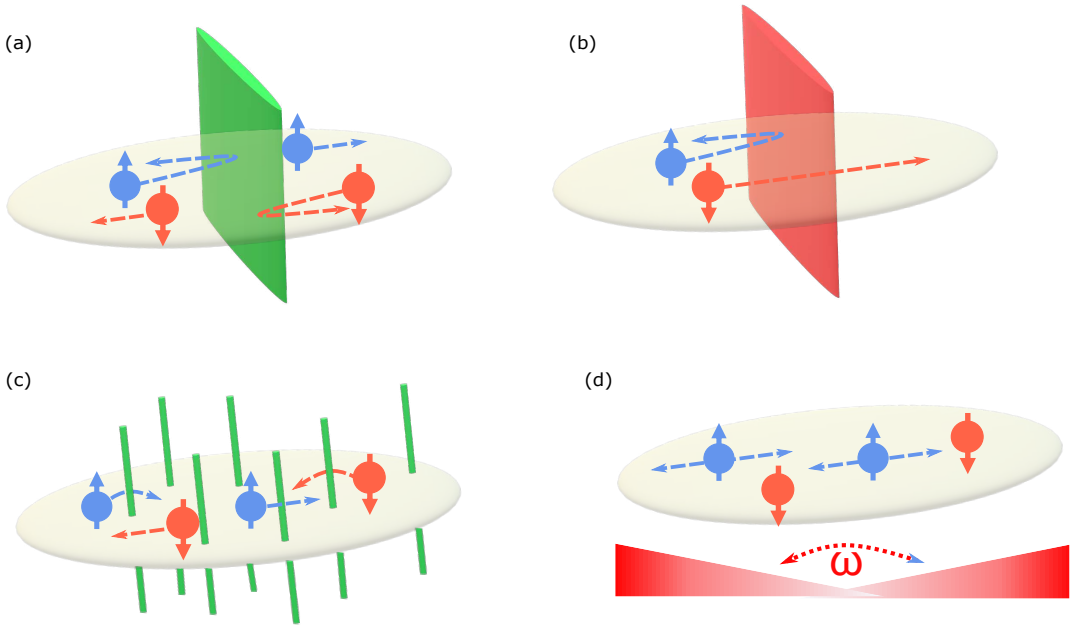

Figure C2: Spin transport experiments with DMD-tailored optical potentials. (a) Spin currents in presence of a repulsive barrier. (b) Mass currents in presence of a spin-selective barrier. This barrier could also be engineered to introduce losses to either one or both spin states. (c) Spin currents in presence of patterns of either ordered or disordered repulsive obstacles. (d) AC spin currents obtained by switching the image displayed on the DMD screen between gradients with opposite slopes.

Finally, we can use our experimental setup to investigate the AC optical spin conductivity of our sample by imprinting time-dependent spin currents. To imprint such currents we can exploit the dynamical properties of the DMD and switch between images of differently oriented gradients at a rate ω, which defines the frequency of the spin current (C2 (d)). As the maximum picture time of the DMD is 56 μs, corresponding to a maximum frequency of $\sim$ 10 kHz, we have an upper boundary to the range of frequencies we can experimentally investigate. Further, due to the non-negligible scattering rate, we cannot shine the DMD-tailored beam on the atomic cloud for the whole time interval between two different DMD images, as this can be of the order of hundreds of microseconds or even more in the case of low-frequency currents. To overcome this, we can combine the dynamic properties of the DMD with the AOM stabilization in order to reduce or modulate the light intensity parallel to the switching of the DMD images.
While the scattering rate associated with the spin-dependent potentials is generally an undesired effect, it can be exploited for introducing selective heating or losses on one spin state. In particular, we could investigate the effect of a spin-dependent barrier such as that of C2 (b) in experimental conditions where the barrier introduces strong spin-selective losses, acting as a dissipative spin-filter [73, 76]. Further, heating only one spin component may allow to investigate heat transport in spin mixtures across different geometries, interaction regimes and in both balanced and spin-imbalanced mixtures. As the scattering rate is proportional to the intensity of the laser beam, using a linearly-shaped beam results in a linear dependence of the photon

absorption probability. By opportunely tuning the experimental parameters we could find a configuration where we can achieve a linear heating of our sample and thus realize a gradient of temperature for either one or both the spin states. We stress that it may prove rather difficult to obtain such temperature gradient due to atoms thermalizing into a system with uniform temperature. However, the tunability of interatomic interactions allows us to produce weakly interacting systems in order to reduce such thermalization process, or to enhance it by increasing the interactions' strength. Having such control on thermalization effects may help us find the best experimental conditions for investigating spin and heat transport in ultracold Fermi gases [48–50].

The versatility of our experimental setup and of the spin-dependent optical potentials allows us to in principle investigate spin transport in ultracold Fermi gases combining features of all the described geometries and experiment. Further, all the aforementioned experiments can be performed in either balanced or spin imbalanced systems across all possible interaction regimes. In conclusion, spin-dependent optical potentials allow to investigate spin transport phenomena that have so far eluded experimental observation including fast spin drag and time-dependent spin currents. Moreover, our experimental setup can be also exploited for introducing local spin-selective perturbations which opens up interesting possibilities for probing the spin-conductivity of fermionic systems in presence of both dissipative and non-dissipative structures. This local and differential manipulation of spin states in degenerate Fermi gases will allow us to address spin transport in strongly correlated fermionic systems across different geometries and interaction regimes.

Bibliography

[1]R. P. Feynman, "Simulating physics with computers", International Journal of Theoretical Physics **21**, 467–488 (1982).

[2]I. Bloch, J. Dalibard, and W. Zwerger, "Many-body physics with ultracold gases", Rev. Mod. Phys. **80**, 885 (2008).

[3]C. Chin, R. Grimm, P. Julienne, and E. Tiesinga, "Feshbach resonances in ultracold gases", Reviews of Modern Physics **82**, 1225–1286 (2010).

[4]W. Ketterle and M. W. Zwierlein, "Making, probing and understanding ultracold Fermi gases", Rivista del Nuovo Cimento **31**, 247–422 (2008).

[5]M. Randeria, W Zwerger, and M Zwierlein, "The bcs–bec crossover and the unitary fermi gas", in *The bcs-bec crossover and the unitary fermi gas* (Springer, 2012), pp. 1–32.

[6]K.-H. Bennemann and J. B. Ketterson, *Novel superfluids: volume 1*, Vol. 156 (OUP Oxford, 2013).

[7]L. Amico et al., "Roadmap on Atomtronics: State of the art and perspective", (2020).

[8]J. Kondo, "Resistance Minimum in Dilute Magnetic Alloys", Progress of Theoretical Physics **32**, 37–49 (1964).

[9]J. Bardeen, L. N. Cooper, and J. R. Schrieffer, "Microscopic theory of superconductivity", Phys. Rev. **106**, 162–164 (1957).

[10]T. Timusk and B. Statt, "The pseudogap in high-temperature superconductors: an experimental survey", Reports on Progress in Physics **62**, 61 (1999).

[11]S. A. Wolf, D. D. Awschalom, R. A. Buhrman, J. M. Daughton, S. Von Molnár, M. L. Roukes, A. Y. Chtchelkanova, and D. M. Treger, "Spintronics: A spin-based electronics vision for the future", Science **294**, 1488–1495 (2001).

[12]I. Zutic, J. Fabian, and S. Das Sarma, "Spintronics: fundamentals and applications", Rev. Mod. Phys. **76**, 323–410 (2004).

[13]M. N. Baibich, J. M. Broto, A. Fert, F. N. Van Dau, F. Petroff, P Etienne, G Creuzet, A Friederich, and J Chazelas, "Giant magnetoresistance of (001) fe/(001) cr magnetic superlattices", Physical review letters **61**, 2472 (1988).

[14]A. Fert, "Nobel lecture: origin, development, and future of spintronics", Rev. Mod. Phys. **80**, 1517–1530 (2008).

[15]S. Datta and B. Das, "Electronic analog of the electro-optic modulator", Applied Physics Letters **56**, 665–667 (1990).

[16]D. A. Steck, *Quantum and Atom Optics* (2007).

[17]C. J. Foot, *Atomic physics*, Vol. 7 (Oxford University Press, 2005).

[18]H. J. Metcalf and P. van der Straten, *Laser cooling and trapping* (Springer, New York, 1999).

[19]M. E. Gehm, *Preparation of an optically-trapped degenerate fermi gas of 6li: finding the route to degeneracy* (2003).

[20]A. Burchianti, G. Valtolina, J. A. Seman, E. Pace, M. De Pas, M. Inguscio, M. Zaccanti, and G. Roati, "Efficient all-optical production of large Li 6 quantum gases using D1 gray-molasses cooling", Phys. Rev. A **90**, 1–5 (2014).

[21]R. Grimm, M. Weidemüller, and Y. B. Ovchinnikov, "Optical Dipole Traps for Neutral Atoms", Advances in Atomic, Molecular and Optical Pahysics **42**, 10.1016/S1049-250X(08)60186-X (2000).

[22]W. J. Kwon, G. D. Pace, R. Panza, M. Inguscio, W. Zwerger, M. Zaccanti, F. Scazza, and G. Roati, "Strongly correlated superfluid order parameters from dc Josephson supercurrents", Science **369**, 84–88 (2020).

[23]G. Del Pace, W. J. Kwon, M. Zaccanti, G. Roati, and F. Scazza, "Tunneling transport of unitary fermions across the superfluid transition", Phys. Rev. Lett. **126**, 055301 (2021).

[24]W. J. Kwon, G. Del Pace, K. Xhani, L. Galantucci, A. Muzi Falconi, M. Inguscio, F. Scazza, and G. Roati, "Sound emission and annihilations in a programmable quantum vortex collider", arXiv:2105.15180v2 (2021).

[25]J. J. Sakurai and J. Napolitano, *Modern quantum mechanics* (1994).

[26]J. Dalibard, "Collisional dynamics of ultra-cold atomic gases", Proceedings of the International School of Physics-Enrico Fermi **321**.

[27]G. Del Pace, "Tunneling transport in strongly-interacting atomic fermi gases", PhD thesis (Università degli Studi di Firenze, 2020).

[28]G. Zürn, T. Lompe, A. N. Wenz, S. Jochim, P. S. Julienne, and J. M. Hutson, "Precise characterization of ^{6}Li Feshbach resonances using trap-sideband-resolved RF spectroscopy of weakly bound molecules", Physical Review Letters **110**, 1–5 (2013).

[29]G. Valtolina, "Superfluid and spin dynamics of strongly interacting atomic fermi gases", PhD thesis (Scuola Normale Superiore di Pisa, 2016).

[30]R. Haussmann, W. Rantner, S. Cerrito, and W. Zwerger, "Thermodynamics of the bcs-bec crossover", Physical Review A **75**, 023610 (2007).

[31]J. Dalibard and C. Cohen-Tannoudji, "Laser cooling below the doppler limit by polarization gradients: simple theoretical models", J. Opt. Soc. Am. B **6**, 2023–2045 (1989).

[32]A. Amico, "Probing the many body dynamics of ultracold repulsive fermi gases of lithium atoms.", PhD thesis (Università degli Studi di Firenze, 2018).

[33]G. Del Pace, *Tailored optical potentials for experiments with atomic superfluid*, 2017.

[34]F. Scazza, G. D. Pace, L. Pieri, R. Concas, W. J. Kwon, and G. Roati, "An efficient high-current circuit for fast radio-frequency spectroscopy in cold atomic gases", arXiv:2104.12730 (2021).

[35]M. Inguscio and L. Fallani, *Atomic physics: precise measurements and ultracold matter* (Oxford University Press, 2013).

[36]M. J. H. Ku, A. T. Sommer, L. W. Cheuk, and M. W. Zwierlein, "Revealing the superfluid lambda transition in the universal thermodynamics of a unitary fermi gas", Science **335**, 563–567 (2012).

[37]M. Pustilnik and L. Glazman, "Kondo effect in quantum dots", Journal of Physics: Condensed Matter **16**, R513 (2004).

[38]A. Avsar, H. Ochoa, F. Guinea, B. Zyilmaz, B. J. Van Wees, and I. J. Vera-Marun, "Colloquium: Spintronics in graphene and other two-dimensional materials", Reviews of Modern Physics **92**, 21003 (2020).

[39]G. E. Bauer, E. Saitoh, and B. J. Van Wees, "Spin caloritronics", Nature Materials **11**, 391–399 (2012).

[40]N. F. Mott, "The electrical conductivity of transition metals", Proceedings of the Royal Society of London. Series A-Mathematical and Physical Sciences **153**, 699–717 (1936).

[41]D. K. Ferry, *Transport in semiconductor mesoscopic devices* (IOP Publishing Bristol, 2015).

[42]J. Sinova, D. Culcer, Q. Niu, N. Sinitsyn, T Jungwirth, and A. H. MacDonald, "Universal intrinsic spin hall effect", Physical review letters **92**, 126603 (2004).

[43]Y. K. Kato, R. C. Myers, A. C. Gossard, and D. D. Awschalom, "Observation of the spin hall effect in semiconductors", science **306**, 1910–1913 (2004).

[44]J. Wunderlich, B. Kaestner, J. Sinova, and T. Jungwirth, "Experimental observation of the spin-hall effect in a two-dimensional spin-orbit coupled semiconductor system", Physical review letters **94**, 047204 (2005).

[45]M. C. Beeler, R. A. Williams, K. Jimenez-Garcia, L. J. LeBlanc, A. R. Perry, and I. B. Spielman, "The spin hall effect in a quantum gas", Nature **498**, 201–204 (2013).

[46]K Ohnishi, S Komori, G Yang, K.-R. Jeon, L. Olde Olthof, X Montiel, M. Blamire, and J. Robinson, "Spin-transport in superconductors", Applied Physics Letters **116**, 130501 (2020).

[47]T Kato, Y Ohnuma, M Matsuo, J. Rech, T. Jonckheere, and T Martin, "Microscopic theory of spin transport at the interface between a superconductor and a ferromagnetic insulator", Physical Review B **99**, 144411 (2019).

[48]C. H. Wong, H. T. Stoof, and R. A. Duine, "Spin-seebeck effect in a strongly interacting Fermi gas", Physical Review A - Atomic, Molecular, and Optical Physics **85**, 1–4 (2012).

[49]C. Wong, H. van Driel, R. Kittinaradorn, H. Stoof, and R. Duine, "Spin caloritronics in noncondensed bose gases", Physical review letters **108**, 075301 (2012).

[50]C. H. Wong, H. T. Stoof, and R. A. Duine, "Spin-heat relaxation and thermospin diffusion in atomic Bose and Fermi gases", Physical Review A - Atomic, Molecular, and Optical Physics **91**, 1–14 (2015).

[51]S. T. Goennenwein and G. E. Bauer, "Electron spin blow hot and cold", Nature nanotechnology **7**, 145–147 (2012).

[52]S. Taie, Y. Takasu, S. Sugawa, R. Yamazaki, T. Tsujimoto, R. Murakami, and Y. Takahashi, "Realization of a SU(2)×SU(6) system of fermions in a cold atomic gas", Physical Review Letters **105**, 1–4 (2010).

[53]H. Heiselberg, "Fermi systems with long scattering lengths", Physical Review A **63**, 043606 (2001).

[54]J. M. Luttinger, "An Exactly Soluble Model of a Many-Fermion System", Journal of Mathematical Physics **4**, 1154–1162 (1963).

[55]P. Gegenwart, Q. Si, and F. Steglich, "Quantum criticality in heavy-fermion metals", nature physics **4**, 186–197 (2008).

[56]A. Sommer, M. Ku, G. Roati, and M. W. Zwierlein, "Universal spin transport in a strongly interacting Fermi gas", Nature **472**, 201–204 (2011).

[57]G. Valtolina, F. Scazza, A. Amico, A. Burchianti, A. Recati, T. Enss, M. Inguscio, M. Zaccanti, and G. Roati, "Exploring the ferromagnetic behaviour of a repulsive Fermi gas through spin dynamics", Nature Physics **13**, 704–709 (2017).

[58]T. Enss and J. H. Thywissen, "Universal spin transport and quantum bounds for unitary fermions", Annual Review of Condensed Matter Physics **10**, 85–106 (2019).

[59]S Trotzky, S Beattie, C Luciuk, S Smale, A. Bardon, T Enss, E Taylor, S Zhang, and J. Thywissen, "Observation of the leggett-rice effect in a unitary fermi gas", Physical review letters **114**, 015301 (2015).

[60]R. A. Duine and H. T. Stoof, "Spin Drag in Noncondensed Bose Gases", Physical Review Letters **103**, 1–4 (2009).

[61]S. Krinner, M. Lebrat, D. Husmann, C. Grenier, J.-P. Brantut, and T. Esslinger, "Mapping out spin and particle conductances in a quantum point contact", Proceedings of the National Academy of Sciences **113**, 8144–8149 (2016).

[62]M. Kanász-Nagy, L. Glazman, T. Esslinger, and E. A. Demler, "Anomalous conductances in an ultracold quantum wire", Physical review letters **117**, 255302 (2016).

[63]P. Magierski, B. b. u. Tüzemen, and G. Wlazłowski, "Spin-polarized droplets in the unitary fermi gas", Phys. Rev. A **100**, 033613 (2019).

[64]P. Magierski, B. Tüzemen, and G. Wlazłowski, "Dynamics of spin-polarized impurity in ultracold fermi gas", Physical Review A **104**, 033304 (2021).

[65]L. Herrmann, F. Portier, P. Roche, A. L. Yeyati, T. Kontos, and C. Strunk, "Carbon nanotubes as cooper-pair beam splitters", Physical review letters **104**, 026801 (2010).

[66]L. Hofstetter, S. Csonka, J. Nygård, and C Schönenberger, "Cooper pair splitter realized in a two-quantum-dot y-junction", Nature **461**, 960–963 (2009).

[67]G. Wlazłowski, P. Magierski, J. E. Drut, A. Bulgac, and K. J. Roche, "Cooper pairing above the critical temperature in a unitary fermi gas", Physical review letters **110**, 090401 (2013).

[68]F. Carlini and S. Stringari, "Spin drag and fast response in a quantum mixture of atomic gases", Phys. Rev. A **104**, 023301 (2021).

[69]Y. Sekino, H. Tajima, and S. Uchino, "Optical Spin Transport in Ultracold Quantum Gases", 1–14 (2021).

[70]F. Scazza, G. Valtolina, P. Massignan, A. Recati, A. Amico, A. Burchianti, C. Fort, M. Inguscio, M. Zaccanti, and G. Roati, "Repulsive Fermi Polarons in a Resonant Mixture of Ultracold Li 6 Atoms", Physical Review Letters **118**, 1–6 (2017).

[71]H. S. Adlong, W. E. Liu, F. Scazza, M. Zaccanti, N. D. Oppong, S. Fölling, M. M. Parish, and J. Levinsen, "Quasiparticle Lifetime of the Repulsive Fermi Polaron", Physical Review Letters **125**, 133401 (2020).

[72]M. Houbiers, H. T. Stoof, W. I. McAlexander, and R. G. Hulet, "Elastic and inelastic collisions of atoms in magnetic and optical traps", Physical Review A **57**, R1497–R1500 (1998).

[73]L. Corman, P. Fabritius, S. Haüsler, J. Mohan, L. H. Dogra, D. Husmann, M. Lebrat, and T. Esslinger, "Quantized conductance through a dissipative atomic point contact", Physical Review A **100**, 1–11 (2019).

[74]M. J. Martin, "Quantum Metrology and Many-Body Physics : Pushing the Frontier of the Optical Lattice Clock", PhD thesis (University of Colorado, 2013).

[75]K. Xhani, *Production and observation of degenerate quantum gases of ^{6}li fermionic atoms*, 2014.

[76]M. Lebrat, S. Häusler, P. Fabritius, D. Husmann, L. Corman, and T. Esslinger, "Quantized Conductance through a Spin-Selective Atomic Point Contact", Physical Review Letters **123**, 193605 (2019).

[77]L. Amico, A. Osterloh, and F. Cataliotti, "Quantum many particle systems in ring-shaped optical lattices", Phys. Rev. Lett. **95**, 063201 (2005).

[78]A. Ramanathan, K. C. Wright, S. R. Muniz, M. Zelan, W. T. Hill, C. J. Lobb, K. Helmerson, W. D. Phillips, and G. K. Campbell, "Superflow in a toroidal bose-einstein condensate: an atom circuit with a tunable weak link", Phys. Rev. Lett. **106**, 130401 (2011).

[79]Y. Cai, D. G. Allman, P. Sabharwal, and K. C. Wright, "Persistent currents in rings of ultracold fermionic atoms", **1**, 1–5 (2021).

[80]A. Kumar, R. Dubessy, T. Badr, C. De Rossi, M. De Goër De Herve, L. Longchambon, and H. Perrin, "Producing superfluid circulation states using phase imprinting", Physical Review A **97**, 1–10 (2018).

[81]T. Sleator, T. Pfau, V. Balykin, O. Carnal, and J. Mlynek, "Experimental demonstration of the optical Stern-Gerlach effect", Physical Review Letters **68**, 1996–1999 (1992).

[82]W. Gerlach and O. Stern, "Der experimentelle Nachweis des magnetischen Moments des Silberatoms", Zeitschrift fur Physik **8**, 110–111 (1922).

[83]F. Scazza, C. Hofrichter, M. Höfer, P. C. De Groot, I. Bloch, and S. Fölling, "Observation of two-orbital spin-exchange interactions with ultracold SU(N)-symmetric fermions", Nature Physics **10**, 779–784 (2014).

[84]G. Cappellini, M. Mancini, G. Pagano, P. Lombardi, L. Livi, M. Siciliani De Cumis, P. Cancio, M. Pizzocaro, D. Calonico, F. Levi, C. Sias, J. Catani, M. Inguscio, and L. Fallani, "Direct observation of coherent interorbital spin-exchange dynamics", Physical Review Letters **113**, 1–5 (2014).

[85]G. Andrelczyk, M. Brewczyk, L. Dobrek, M. Gajda, and M. Lewenstein, "Optical generation of vortices in trapped Bose-Einstein condensates", Physical Review A - Atomic, Molecular, and Optical Physics **64**, 10 (2001).

Ringraziamenti

Non ho in mente un momento preciso, ma so che poco dopo avere iniziato la tesi ho capito che avrei voluto ringraziare. Ringraziare chi mi ha accolto al LENS e chi mi ha dato la possibilità di andare, chi mi ha posto davanti a decisioni importanti e chi ha supportato le mie scelte, chi mi ha accompagnato in questo anno da vicino e chi da lontano. Tutte le soddisfazioni di oggi e le prospettive di domani sono grazie a voi.
Non posso non partire dalle persone che hanno reso straordinaria la mia esperienza fiorentina. Grazie Marco, per la tua continua gentilezza e disponibilità, per essere stato un compagno di viaggio nella seconda parte della tesi. Thank you Giulia and Woo Jin, for being a constant guide in the lab, for listening to me and advising me. Thank you for your patience and your counsel, for teaching me that a good physicist doesn't take her/himself too seriously. Thank you for showing me how hard work, passion and determination always pay off. Grazie Francesco e Giacomo, per essere una fonte costante di stimoli, per avermi trasmesso la vostra passione e il vostro entusiasmo. Grazie per tutte le cene, per tutti i consigli, per tutte le opportunità che mi avete dato. Grazie per essere stati degli amici quando era il momento di essere amici e dei maestri quando era il momento di essere dei maestri. Grazie per avermi spinto oltre quelli che pensavo fossero i miei limiti. Grazie per la fiducia che avete riposto in me.
Grazie a tutti voi per i vostri insegnamenti e per avermi accolto come se fossi sempre stato con voi. Sopattutto, grazie per avermi aiutato a capire quello che voglio essere nel futuro.
Grazie a tutti gli amici che ho incontrato in questo ultimo anno: grazie a Daniele, Nicoletta, Alessia, Michele e ai due Lorenzi. Grazie a Matteo per l'interesse che ha sempre dimostrato verso questo lavoro. Grazie a Roberto per avermi esposto i principi della nobile arte della saldatura e per avermi soccorso quando sistematicamente non li mettevo in pratica.
Tutti questi ringraziamenti non ci sarebbero stati senza un persona. Grazie Davide, perchè senza di te tutto questo non sarebbe successo. Grazie per essere stato un professore eccellente, è grazie al tuo corso che ho capito a quale parte della fisica volevo dedicarmi. Grazie per avermi fatto conoscere Giacomo e Francesco e per essere stato sempre disponibile per tutta la durata della tesi. A posteriori, grazie per la tesi triennale perchè, anche se non lo sai, mi hai indirettamente aiutato anche in quella. Visto che siamo in tema, grazie ai miei relatori triennali Tommaso e Giovanni, se amo la fisica sperimentale molto è merito vostro.
Grazie a tutte le amiche e gli amici fisici che mi hanno accompagnato in questi anni. Grazie agli amici di sempre Federico e Massimo, grazie a Carlo, per essere sempre presente e sempre pronto a condividere successi e fallimenti.
Grazie alla mia famiglia che mi ha sempre supportato, chi più vicino chi più lontano. Grazie a Pietro per il troppo poco tempo passato a Firenze, e, insieme a Giulia, grazie di essere dei fratelli straordinari. Un grazie particolare a Lisa e Aldo, mi avete sempre aiutato e supportato. I genitori

non si scelgono, non avrei potuto sceglierne quattro migliori. Ovviamente, un grandissimo grazie ai miei primi due genitori. Mi avete aperto mille strade senza mai impormi quale seguire. Senza il vostro aiuto e il vostro modello non sarei la persona che sono ora.
E, alla fine, non posso che ringraziare te, Micol. Per ogni giorno passato insieme, per ogni giorno passato lontani, per qualcosa che non si può scrivere su un foglio di carta, men che meno in una tesi di laurea.

Les Houches,
19/09/2021